Master of Science Thesis

Sky-dive Cavity Buffeting Noise Reduction

Werner Jousma

January 15, 2018

Aerodynamics

TU**Delft**

Sky-dive Cavity Buffeting Noise Reduction

Master of Science Thesis

For obtaining the degree of Master of Science in Aerospace Engineering at Delft University of Technology

Werner Jousma

January 15, 2018

Faculty of Aerospace Engineering   ·   Delft University of Technology

Delft University of Technology

DELFT UNIVERSITY OF TECHNOLOGY
DEPARTMENT OF AERODYNAMICS

The undersigned hereby certify that they have read and recommend to the Faculty of Aerospace Engineering for acceptance the thesis entitled **"Sky-dive Cavity Buffeting Noise Reduction"** by **Werner Jousma** in fulfillment of the requirements for the degree of **Master of Science**.

Dated: January 15, 2018

Supervisors:

_____

Dr.ir. A.H. van Zuijlen

_____

Dr.ir. B.W. van Oudheusden

_____

Dr. F. Avallone

_____

E Terry, MSc

Preface

This thesis is the final milestone in obtaining my Master degree in Aerodynamics, at Delft University of Technology. This report presents my work on the master thesis, performed at Actiflow BV under supervision of Dr.ir. A.H. van Zuijlen (Delft University of Technology) and E. Terry, MSc (Actiflow BV).

In the current state of prosperity of western countries like the Netherlands, our own comfort is becoming more important than ever. For sky-dive tunnels, a big comfort issue, which can be improved on, is found in cavity buffeting noise. Sky-dive tunnel cavity buffeting noise reductions are particularly interesting to research due to the complex flow mechanisms found for relative simple geometries and the instant improvements you can physically experience during on-site tests.

I wish to take this opportunity to thank my supervisors Dr.ir. A.H. van Zuijlen (Delft University of Technology) and E. Terry, MSc (Actiflow BV) for the critical, though righteous feedback on my work and writing, and for enabling me to pursue this topic. Furthermore I would like to thank my dear "Alleen gerookte avocado"/Forze friends, with whom I have experienced many bright moments during a Forze Hydrogen Racing board-year, which facilitated unbelievable professional and personal growth. To my girlfriend Doutsen, thank you for dragging me trough the last bits and pieces of this thesis and for the unconditional support, I would be lost without you. Special thanks to my parents, Henk and Gea Jousma, who have supported every decision I made the past six and a half years and enabled me to study and grow as a person.

"Life is about passions - Thank you for sharing mine" - der Schumi

Abstract

Cavity buffeting noise is the main contributor to discomfort in sky-dive tunnels. Low frequency noise, generated by self-sustained cavity shear-layer oscillations, similar to automotive sunroof-buffeting noise and side-window buffeting noise, is observed in sky-dive tunnels. Typical low frequencies are not conventionally audible to the human ear: registration of this phenomenon occurs due to the high strength of the oscillations felt on the inner-ear. Long-term exposure to high intensity low frequency noise can be experienced as fatiguing and annoying. A design Study of Streamlines Design BV has shown a fully effective design solution by simulation, which proved to be ineffective in real-life. The current study deals with validation of a different numerical set-up and the analysis of various retrofit designs for the reduction of sky-dive buffeting noise.

Existing literature has shown the promising results for the use of compressible computational fluid dynamics solvers, combined with detached eddy simulation for similar problems. The computational cost of detached eddy simulation has been found within the computational resources for this thesis, opposed to large eddy simulation or direct numerical simulation. For this thesis, the delayed detached eddy simulation model has been used. For the acquisition of validation data a Scanivalve DSA3217 pressure scanner has been used. For computational fluid dynamics and experiments, pressure has been probed at the same location in the cavity. Four retrofit designs have been proposed for analysis in this thesis: trailing edge extension, wall normal cylinder, span wise cylinder and a wing. Simulations have been conducted for one specific tunnel velocity and experiments for a full range of operating set-points.

Simulations have shown reductions of 6.0 dB and 2.6 dB for respectively the trailing edge extension and the wing in sound pressure levels of cavity buffeting noise. Furthermore an increase of 3.6 dB and 1.5 dB have been observed for respectively the span wise cylinder and wall normal cylinder. A reduction of the wake by 5.2% has been observed for the trailing edge extension, where the other designs increased the wake. For the clear reduction in sound pressure level, introduced by the trailing edge extension, the formation of a larger scale vortex has been delayed downstream compared to the current situation. Visualising the vortices in the case of the span wise cylinder, it has been found that the formation of the large scale vortex has been triggered further upstream compared to the current situation, possibly due to interaction with cylinder vortex shedding.

Comparison of simulation and experiment data has shown errors of 11.8% in sound pressure level for the current situation and 17.6% when the trailing edge extension is employed. The reduction in experiment has been observed to be stronger than in simulation.

An evaluation experiment has shown the effectiveness of the trailing edge extension for all tunnel

velocities at which high sound pressure levels have been observed. Reductions between 7.7 dB and 22.6 dB have been observed. Over the whole range of tunnel velocities, the sound pressure level has been reduced to 130.1 dB and below.

Concluding on the thesis work, the numerical model is able to predict a reduction. Following the simulation work the trailing edge extension is most effective in both reducing the noise and maintaining tunnel performance. Furthermore, the trailing edge extension has proved effectiveness for all critical tunnel velocities in experiment.

Table of Contents

List of Figures

List of Tables

Nomenclature

Abbreviations

Symbol	Description	Dimensions	Units
CFD	Computational Fluid Dynamics	-	-
CVT	Cylinder Vortex	-	-
DES	Detached Eddy Simulation	-	-
DNC	Direct Noise Computation	-	-
ILSVT	Impinged Large Scale Vortex	-	-
LE	Leading Edge	-	-
LES	Large Eddy Simulation	-	-
LSVT	Large Scale Vortex	-	-
OpenFOAM	Open source Field Operation And Manipulation	-	-
P1	Probe1	-	-
P2	Probe2	-	-
RANS	Reynolds Average Navier Stokes	-	-
SGS	Sub-grid Scale	-	-
SPL	Sound Pressure Level	-	dB
SUV	Sports Utility Vehicle	-	-
SWC	Span Wise Cylinder	-	-
TE	Trailing Edge	-	-
TEE	Trailing Edge Extension	-	-
VT	Vortex	-	-
WNC	Wall Normal Cylinder	-	-

Greek Symbols

Symbol	Description	Dimensions	Units
α	Thermal diffusivity	$WL^{-1} t^{-1}$	$kg\ m^{-1}\ s^{-1}$
α_{ROS}	Emperical constant for phase-lag compensation	-	-

Δ	Sub grid scale	L	m
δ	Boundary layer thickness	L	m
γ	Heat capacity ratio	-	-
κ	von Kármán constant	-	-
κ_{ROS}	Emperical constant	-	-
λ	Eigenvalues for λ_2 criterion	-	-
μ	Dynamic viscosity	W L^{-1} t^{-1}	kg m^{-1} s^{-1}
ν	Kinematic viscosity	L^2 t^{-1}	m^2 s^{-1}
Ω	Anti-symmetric part velocity gradient tensor	t^{-1}	s^{-1}
ϕ	Dummy variable for mathematics purposes	-	-
Ψ	Compressibility	-	-
ρ	Density	W L^{-3}	kg m^{-3}
σ	Relative system volume change	-	-
τ	Stress tensor	W L^{-1} t^{-2}	kg m^{-1} s^{-2}
θ	Boundary layer momentum thickness	L	m
$\tilde{\nu}$	Turbulent transport variable SA model	L^2 t^{-1}	m^2 s^{-1}

Roman Symbols

Symbol	Description	Dimensions	Units
$\tilde{d}$	DES wall distance	L	m
S	Cell face area (vector)	L^2	m^2
A	Cavity opening area	L^2	m^2
a$_0$	Speed of sound (freestream)	L t^{-1}	m s^{-1}
C$_{DES}$	DES model constant	-	-
D	Cavity depth	L	m
d	Wall distance	L	m
f	Frequency	t^{-1}	Hz
f$_d$	DDES blending function	-	-
G	Distortion compensation gain	-	dB
G(x)	Filter function	-	-
h	Specific enthalpy	L^2 t^2	m^2 s^2
h$_n$	Cavity neck length	L	m
h$_{conv}$	Average cell size estimate	-	-
K	Specific kinetic energy	L^2 t^2	m^2 s^2
k	Expansion coefficient	-	-

L	Cavity length (dimension in flow direction)	L	m
M	Mach number	-	-
n	Number of spanwise vortices in cavity opening	-	-
p	Pressure	W L^{-1} t^{-2}	Pa
p_{conv}	Rate of convergence	-	-
q	Heat-flux	L^3 t^{-3}	m^3 s^{-3}
R	Specific gas constant	L^2 t^{-2} T^{-1}	m^2 s^{-2} K^{-1}
r_d	SA model constant	-	-
Re	Reynolds number	-	-
S	Symmetric part velocity gradient tensor	t^{-1}	s^{-1}
S_f	Cell face area	L^2	m^2
St	Strouhal number	-	-
T	Temperature	T	K
U	Velocity magnitude	L t^{-1}	m s^{-1}
u	Velocity component	L t^{-1}	m s^{-1}
V_c	Cavity volume	L^3	m^3
V_t	Tube volume	L^3	m^3
V_v	Measurement system volume	L^3	m^3
W	Cavity width (span-wise direction)	L	m
x	Spatial vector direction	L	m

Subscripts

Symbol	Description	Dimensions	Units
∞	Indication of free stream condition	-	-
θ	Indication momentum thickness for length scale	L	m
0	Indication of upstream location	-	-
D	Indication cavity depth for length scale	L	m
eff	Indication summation of turbulent and laminar properties	-	-
f	Indication cell centre to face interpolation	-	-
i	Indication of a vector component	-	-
j	Summation vector index	-	-

L	Indication cavity length for length scale	L	m
ref	Indication of reference value	-	-
t	Indication of turbulent variant of property	-	-

Chapter 1

Introduction

1.1 Motivation

Like all wind-tunnels, sky-dive tunnels are known to generate noise. One of the biggest sources of aerodynamic noise in sky-dive tunnels originates from the entrance which forms a cavity in the tunnel wall. Sky-dive tunnels are mostly used for amusement purposes which makes consumer comfort an important aspect. Low frequency noise (infra-sound, typically below 20 Hz) is generated by this cavity, which is often categorised as "buffeting" noise, similar to automotive sunroof of side window buffeting noise. Frequencies below 20 Hz are typically not audible to the human ear. Nevertheless, buffeting noise has severe influence during long time exposure. Gong et al. (2016) describes the effects of buffeting noise as "fatiguing" and "annoying". Similar results have been found in a toxicological study (Haneke et al., 2001). Next to this, certain frequencies (around 18 Hz) can cause resonance in the human eyeball (Ohlbaum, 1976).

In order to not compromise on the performance of the tunnel, Actiflow BV recently conducted a design study towards the development of a trailing edge design for noise reduction. By initial simulations, the presumption has been developed that this solution is very effective in reducing buffeting noise. These initial simulations have been performed by the means available for the particular study and are therefore not validated with reality. A lack of confidence in the used simulation methods remains which is enforced by observations in the evaluation of the project: buffeting noise remains dominant with the current design solution.

Actiflow BV has commissioned a research project in order to asses the accuracy of numerical methods to asses different retrofit solutions for buffeting noise reduction, which could be applied to existing sky-dive tunnels including city sky-dive Utrecht. Actiflow BV believes that by adding retrofit design solutions to existing sky-dive tunnels, it is possible to reduce buffeting noise and with that improve consumer comfort.

1.2 Project Objective

The main (external) objective of the research has been established as follows:

"To provide Actiflow BV with recommendations on designs for Sky-dive tunnel cavity buffeting noise reduction by using experimental measurements and computational fluid dynamics."

In order to achieve the main external goal, three sub-goals are formulated and listed in the following.

1. Validation of a numerical set-up by comparison of time-varying pressure data from measurements and CFD.

2. Assessment of various retrofit cavity buffeting reducing designs by applying the CFD set-up.

3. Evaluation of the most effective retrofit design by experimental pressure measurements.

1.3 Research Questions

For these goals, questions and sub-questions have been formulated as listed in the following.

1. To which extend can the numerical set-up be validated for sky-dive cavity buffeting noise prediction?

   (a) Which flow mechanisms have to be anticipated according to existing literature?
   (b) Which numerical set-ups have been validated before for similar problems and are feasible to use within the scope of the thesis project, according to existing literature?
   (c) How do the numerical predictions correlate with experimental measurements?

2. Which retrofit design is most effective in suppressing cavity buffeting noise, according to the numerical set-up?

   (a) Which retrofit designs can be proposed based on existing literature?
   (b) How do the retrofit designs affect cavity buffeting noise and the associated flow mechanisms, according to the numerical set-up?
   (c) How do the retrofit designs affect tunnel performance (flow uniformity) in the sky-dive section, according to the numerical set-up?

3. To what extend is the cavity buffeting noise suppression effective, according the evaluation measurements?

   (a) Which oscillation strength reduction is found for the simulate tunnel velocity according to experimental measurements?

(b) How does the retrofit design influence oscillation strength for other tunnel velocities?

It is evident that the research questions combined will provide the information necessary to contribute to the external objective of this thesis.

1.4 Properties and Situation City-Skydive Utrecht

The current (cavity buffeting noise producing) tunnel-geometry has been presented in Figure 1.1. In Figure 1.1(b) it can be seen that the waiting room looks like a Helmholtz type cavity in the wall of the tunnel. The entrance opening has overhang on 3 out of 4 edges, which form a throat towards a bigger volume.

The operating conditions of the tunnel are defined to be ranging from 0 to 75 ms^{-1}, which results in Mach numbers (M) between 0 and 0.22 and cavity length based Reynolds number (Re) between 0 and 1.2×10^7.
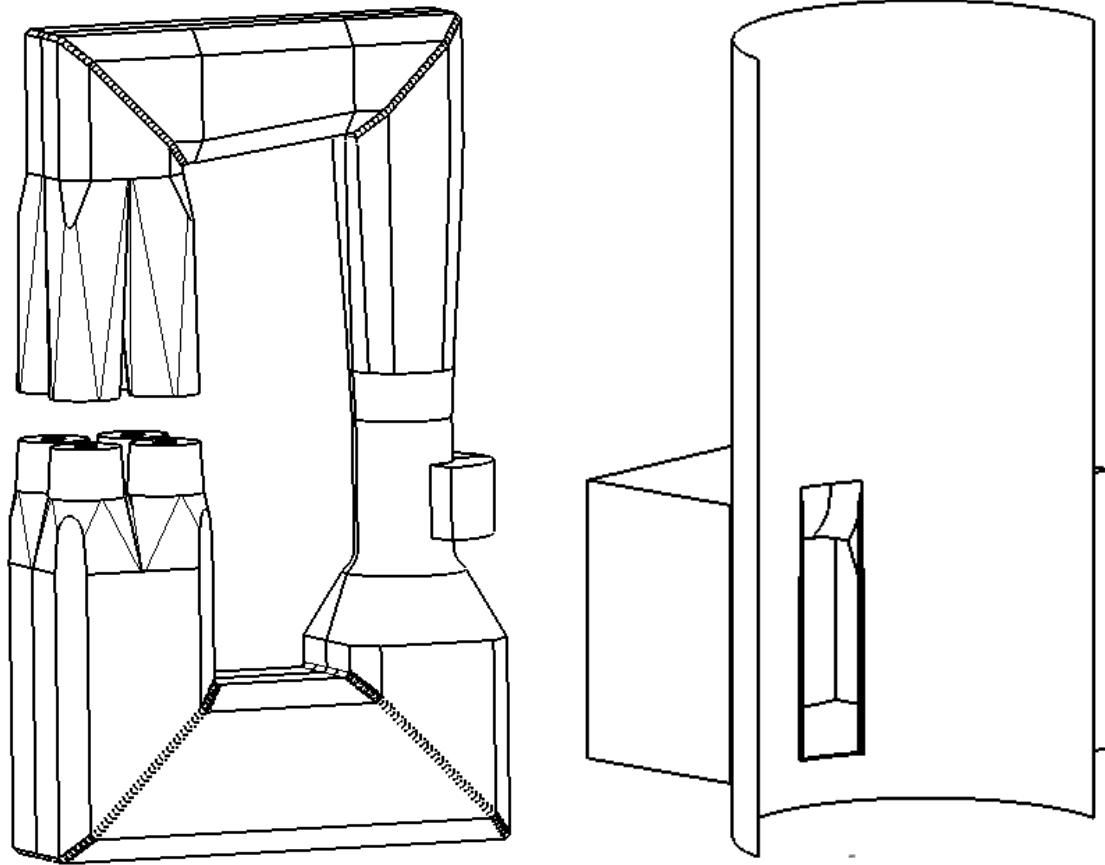
(a) Full tunnel schematic view

(b) Zoomed view inside tunnel at waiting room entrance

Figure 1.1: Existing geometry of tunnel at City-Skydive Utrecht

1.5   Document structure

This thesis contains three major parts in which chapters are categorised. After this introduction, the read first finds a part called Background Theory. In this part the author outlines existing literature and knowledge on the topic of flows over cavities and the accompanied flow mechanisms. Furthermore existing literature on the reduction of cavity induced noise (cavity buffeting noise) will be discussed.

Next the reader will find the Methodology part. In this part, the author will first discuss the numerical set-up, with which the current situation and retrofit designs will be analysed. Hereafter, the experiment set-up which will provide validation data and evaluation measurements will be outlined. The last chapter in this part will discuss additional data processing for both the numerical and experiment data.

The third part that the reader will encounter contains the results of this thesis. First the results found for the current situation of both simulation and experiment will be presented. After this, the results of simulation of the retrofit designs will discussed and the evaluation experiment of the best performing retrofit design will be presented.

The last part of this thesis is named Conclusions and Recommendations. In this part the reader will find a systematic answering of the research questions, after which recommendations for future work will be provided.

Part I

Background Theory

Chapter 2

Flow mechanisms of cavities

Flow and acoustic mechanisms of flows over an open cavities have been studied extensively over the years. Flow mechanisms, which potentially can be recognised in the flow over a cavity of a sky-dive tunnel are addressed in existing literature.

In this chapter, an overview of leading research in flow and acoustic mechanisms regarding flow over cavities will be presented.

2.1 Flow Mechanisms

Despite the relative simple geometry used in most experiments and simulations concerning a flow over cavity, the flow mechanisms observed in these experiments and simulations are complex.

The work of Rowley et al. (2002) describes two different flow mechanisms following from observations of two dimensional direct numerical simulation (DNS): the "shear-layer mode" and the "wake-mode". Both modes can occur for different situations and driving flow parameters, but also a combination of both can exists.

2.1.1 Shear-layer mode

The first mode described by Rowley et al. (2002) is the shear-layer mode. The boundary layer, existing upstream of the cavity, detaches when it reaches the leading wall of the cavity, forming a shear-layer. This shear-layer rolls up towards the trailing wall of the cavity, which results in vortex shedding. These vortices collide with the trailing wall of the cavity, creating pressure disturbances in the cavity, which propagates upstream as waves. The disturbances have an amplifying effect on the instabilities originating at he upstream wall of the cavity, closing a loop. This flow mechanism

is usually referred to as the acoustic feedback mechanism. A schematic representation of this feedback mechanism has been visualised in Figure 2.1.
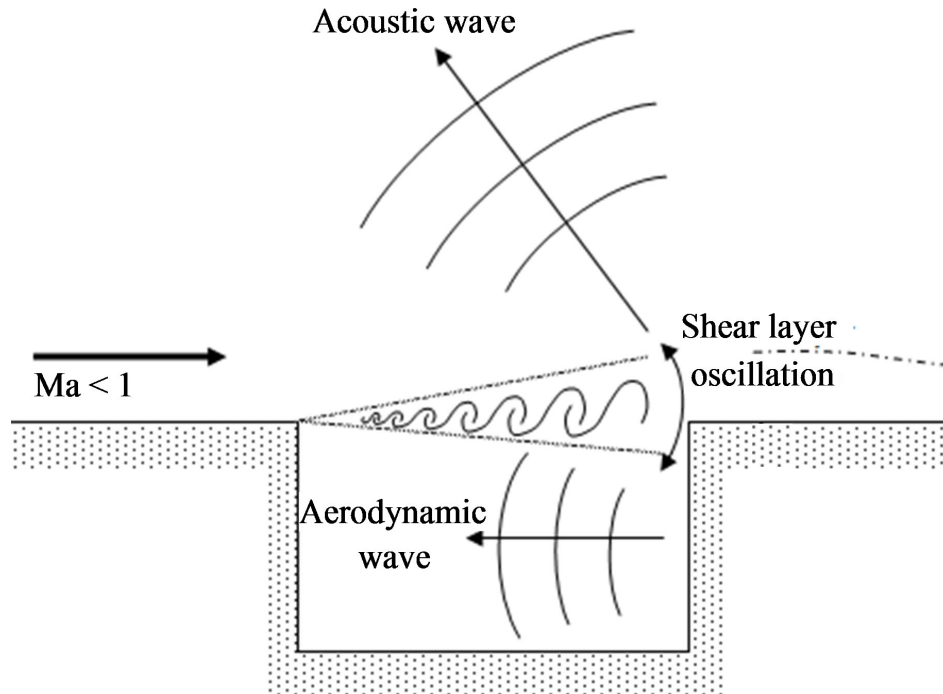
Figure 2.1: Schematic representation of feedback mechanism (Dykas et al., 2012)

The shear-layer mode has been classified further by Rockwell and Naudascher (1978), in their work, the mechanisms which can be observed in the case of a shear-layer mode have been sub-classified by three categories: fluid-dynamic oscillations, fluid-resonant oscillations and fluid-elastic oscillations. For the different categories, different feedback mechanisms can be observed.

Fluid-dynamic oscillations and fluid-resonant oscillations

Fluid-dynamic oscillations are driven by the two mechanisms which characterize the shear-layer mode described by Rowley et al. (2002), mentioned earlier in this section. This category of oscillations occur when the cavity length is much smaller than the acoustic-wavelength, corresponding to the frequency of the oscillations. The interaction of the vorticity with the trailing wall, strongly enhance the instability (Rockwell and Naudascher, 1978).

Fluid-resonant oscillations can occur when the feedback mechanism is driven by resonant acoustic waves, caused by acoustic cavity modes. Resonant oscillations appear when the acoustic wavelength accompanying the frequency of the oscillation is much smaller than the characteristic lengths of the cavity. This particular category of self-sustained oscillations are fed by longitudinal (leading to trailing edge) or transverse (bottom to top) standing waves. According to Rockwell and Naudascher (1978), fluid-resonant oscillations can be observed at specific wavelength to cavity

length ratios, which are not evident to predict. The fluid-resonant oscillation produces noise at the specific frequencies related to the resonant wave-lengths. The distinction with the fluid-dynamic oscillation is relative small. According to Rockwell and Naudascher (1978), for the same cavity geometry a combination of both can exist for different values of free stream velocities.

Many attempts have been made to develop analytic relations in order to capture the frequencies at which the fluid-resonant oscillations occur. One of the earlier attempts was performed by Rossiter (1967). His work is motivated by the sound generation of fighter aircraft bomb-bays, which are a different application of wall cavities. The work of Rossiter (1967) consists of various experiment at various flow and geometry variations.

Rossiter (1967) observed the periodic vortex shedding at the leading edge of the cavity and observed the existence of the acoustic feedback mechanism.

The most important, and most used result from his work is the semi-empirical relation he formulated as presented in Equation (2.1).

$$St_L = \frac{fL}{U_\infty} = \frac{n - \alpha_{ROS}}{M_\infty + \frac{1}{\kappa_{ROS}}} \tag{2.1}$$

From Equation (2.1) it becomes clear that the cavity length based Strouhal number (St_L) is dependent on the following listed parameters:

- n: the number of vortices observed over the cavity mouth. ($= 1, 2, 3....$)

- α_{ROS}: an empirical constant, contribution of phase lag (0.25).

- M_∞: Mach number of the free stream flow.

- κ: an empirical constant, calibrated for experiments of (Rossiter, 1967) (0.57).

For many cases of flows over a cavity (mainly the ones with a simple geometry), this basic equation can work resonably well. The formulation of Rossiter (1967) has been improved by Heller and Bliss (1975). This improved formulation has been adapted such that it can compensate for the change in Mach number inside of th cavity. The adapted equation has been presented in Equation (2.2), which extends the use of the semi-empirical relation towards higher Mach numbers.

$$St_L = \frac{fL}{U} = \frac{n - \alpha_{ROS}}{\frac{M_\infty}{\sqrt{1 + \frac{\gamma - 1}{2} M_\infty^2}} + \frac{1}{\kappa_{ROS}}} \tag{2.2}$$

An additional parameter can be found in this equation, which is γ and represents the heat capacity ratio of the fluid.

Although mentioned at the fluid-resonant oscillation category in Rockwell and Naudascher (1978), the observations made by Rossiter can also relate to the fluid-dynamic oscillation. The distinction

between the fluid-dynamic oscillation and the fluid-resonant oscillation remains vague, as both produce considerable high sound pressure levels driven by very similar mechanisms. Also the use of "much smaller" by Rockwell and Naudascher (1978) for the categorisation based on wavelength to cavity length ratio, can not be quantified easily which makes the distinction based on geometric and flow properties impossible prior to experiment or simulation. This does not necessarily impose an issue; both oscillation modes are known to produce a feedback mechanism which is driven by acoustic waves and therefore both would be able to be captured by similar numerical techniques. Both can occur for the same cavity geometry exposed to different flow velocities and when the Rossiter frequencies are close to a resonance mode of the cavity, a lock-on state can be observed (Rockwell and Naudascher, 1978).

For the current study, the fluid-resonant oscillation is likely to occur with a Helmholtz resonance mode, as the shape of the sky-dive tunnel cavity is very similar. Wang et al. (2013) presents an equation (presented in Equation (2.3)) which can be used for the estimation of the frequency at which Helmholtz resonance occurs for a cavity with a rectangular opening.

$$f = \frac{a_0}{2\pi} \sqrt{\frac{A}{(h_n + 0.82\sqrt{A})V_c}} \tag{2.3}$$

Where the following definitions apply.

- a_0: speed of sound $(\mathrm{ms^{-1}})$.
- A: area of cavity opening $(\mathrm{m^2})$.
- h_n: length of neck towards cavity (m).
- V_c: volume of the cavity $(\mathrm{m^3})$.

Fluid-elastic oscillations

Fluid-elastic oscillations have different driving mechanism: they are fed by the feedback of the elastic behaviour of solid boundaries. In this flow mechanism, moving walls, which vibrate due to periodic instabilities in the shear-layer, employ a similar feedback mechanism as in the other two categories.
If this feedback mechanism is present, the problem becomes one of the fluid-structure interaction type. Of the three cavity types, this one has been researched the least thorough.

Vortex-edge interaction

Another mechanism which can cause tonal noise at lower frequencies has been described by Rockwell and Knisely (1980). In water-tunnel experiments it has been found that different types of interaction between the vortex and the edge it impinges on exist: complete escape, partial
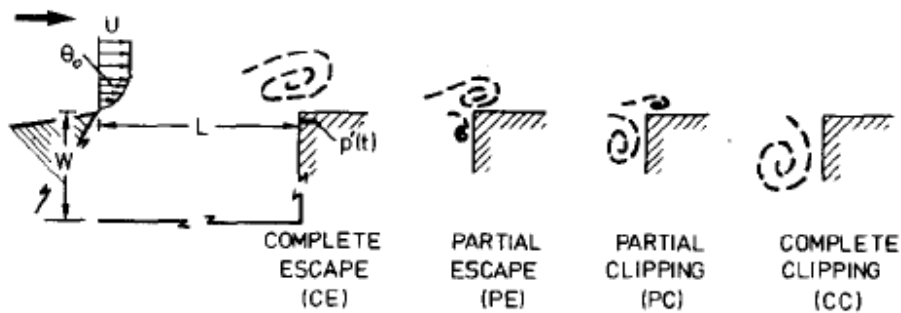
Figure 2.2: Different vortex-edge interaction modes (Rockwell and Knisely, 1980).

escape, partial clipping and complete clipping. An graphical representation has been presented in Figure 2.2.

The vortex-edge interaction modes do not stay constant over time. Rockwell and Knisely (1980) found a very periodic behaviour in the switching between modes. Although these experiments were conducted for water, this flow mechanism should be considered as a possible low frequency source.

2.1.2 Wake mode

The second mode that has been described by Rowley et al. (2002) is the wake mode. This mode is a more violent mode in which vortex shedding is not so obvious any-more. Rather than vortex shedding, a large vortex fills the complete cavity. This modes creates a flow field which is more similar to the wake behind a bluff body than to a shear-layer. Early research on the wake mode has been described by Gharib and Roshko (1987).
During th formation of the cavity-size vortex, a small part of the free-stream flow is bend into the cavity and breaks down on the cavity bottom.
From simulation runs described in Rowley et al. (2002), Rowley found that flow over a cavity in wake mode has more influence on the flow field above the cavity. A comparison of stream lines in the time averaged flow over cavities with shear-layer mode and wake-mode present have been presented in Figure 2.3. Both cavities are investigated at the same Mach number. Due to an increased length, the wake mode has been triggered.

The simulations described in Rowley et al. (2002), show a correlation between the increase in cavity length or depth, relative to the momentum thickness of th boundary layer upstream of the cavity and the occurrence of the wake mode.
Opposed to the Mach number dependence of the vortex shedding in shear-layer mode, the wake mode has found to be almost independent of Mach number (where the transition to wake mode is highly dependent on Mach number).
The wake mode is less likely to occur when the upstream boundary layer is turbulent, as the acoustic field radiated by the cavity becomes less intense when the boundary layer is turbulent. Next to this, wake mode is prevented by other three dimensional effects, such as the presence of

side walls in the cavity.
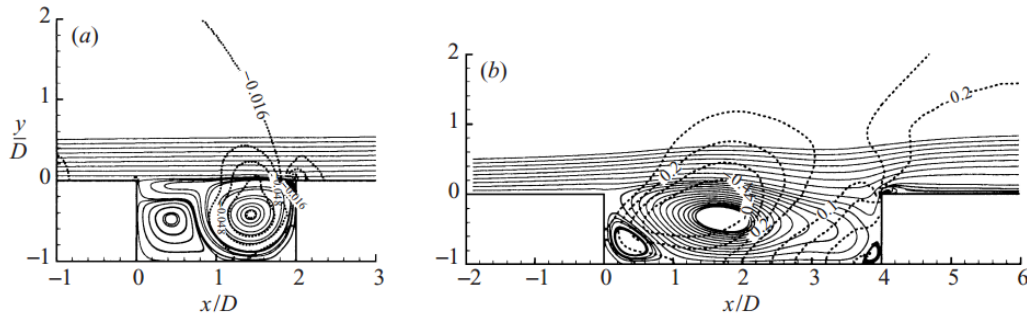
Figure 2.3: Comparison of time averaged flow stream lines of a cavity in shear-layer mode (left) and wake mode (right) (Rowley et al., 2002)

2.2   Aerodynamic Sound Sources of flows over cavities

In order to select a proper computational set-up for the prediction of buffeting noise of City-Skydive Utrecht, it is of high importance to determine which kind of sound sources are present in cavities with low Mach numbers.

Howe (2004) studied the sound mechanism in the flows over cavities. Howe concluded from the research that a dipole distribution, primarily on the leading and trailing edges of the cavity are dominant in very low Mach number flow (approximately M<0.01). When the Mach number approaches/exceeds a certain value (M>0.05) the monopole compressibility reaches similar magnitude as the dipole sources, specifically for resonant frequencies.

2.3   Driving flow and geometry parameters

The flow mechanism of the flow over an open cavity has been an interesting topic of study in the experimental field. In the many studies which have been conducted over the years, many different driving parameters have been identified by researchers in order to attempt to predict the behaviour based on geometry and dimensionless flow parameters.

2.3.1   Geometric parameters

Based on studies of cavities with simple geometries (Rossiter, 1967; Rockwell and Naudascher, 1978; Rowley et al., 2002; Ahuja and Mendoza, 1995), geometric dependencies have been found. The geometric parameters of interest have been listed in the following.

- **Shallow/deep classification ($\frac{L}{D}$):** the length to depth ratio of a cavity determines whether it is a deep or a shallow cavity. Shallow and deep cavities show different types of behaviour.

  Shallow/deep classification is most important when a fluid-resonant oscillation occurs; deep cavities will more likely encounter transverse waves (bottom to top) and shallow cavities are likely to produce longitudinal waves (leading to trailing wall).

  Ahuja and Mendoza (1995) classifies deep cavities by length over depth ratios lower than unity, and shallow bigger than unity. On the other hand for Rossiter (1967) this ratio limit is found at 4.

  A consequence of certain shallowness of cavities could be the open/closed nature of the cavity. As shown in the article of Gloerfelt (2009), the nature of a cavity can become closed when very shallow. In this kind of classification, three classes exist: closed, open and transitional.

- **Two dimensional/three dimensional behaviour ($\frac{L}{W}$):** the length to width determines whether the cavity instabilities behave two or three dimensional. Typically, cavities with length over width ratios than unity, are found to show two dimensional behaviour where length to width ratios higher than unity show three dimensional behaviour (Ahuja and Mendoza, 1995).

2.3.2 Flow parameters

Many relevant flow parameters have been identified. In the following list, the most influential parameters are listed and elaborated on.

- **Free stream Mach number (M_∞):** directly found from the relation presented in Equation (2.2) and Equation (2.1), the Mach number can be found as a driving parameter for the feedback mechanism, and influences the frequency of the oscillation.

- **(Momentum) thicknes of upstream boundary layer ($\frac{\theta_0}{L}$, $\frac{\theta_0}{D}$, $\frac{\delta_0}{L}$):** the (momentum thickness) of the upstream boundary layer contributes to the thickness of the shear-layer. The noise generated by the shear-layer is dependent on the thickness of the shear-layer (Rockwell and Naudascher, 1978; Rowley et al., 2002). In order to make the momentum thickness non-dimensional it is typically divided by the length or depth of the cavity. Comparison of a thick and thin boundary layer upstream of the cavity has been presented in Henderson (2000). The thickness of the upstream boundary layer is also a determining parameter in the distinction between wake mode and shear-layer mode.

  (Ahuja and Mendoza, 1995) also found lower noise levels for thicker upstream boundary layers. He observed that the self-excited oscillations vanish when $\frac{\delta_0}{L} = 0.07$ is reached for boundary-layer thickness.

- **Reynolds number (Re_L, Re_D, Re_θ):** The Reynolds number can be a driving parameter in the classification of flows over cavities. Not only the Reynolds number based on the cavity length or depth is important, also the Reynolds number based on the momentum thickness,

as it can be a determining factor in the nature of the cavity (Rowley et al., 2002; Rockwell and Naudascher, 1978).

- **Strouhal number (St_L):** found in Equation (2.1), the Strouhal number based on cavity length can provide important information about frequencies, but also in scalability to other problems (Rossiter, 1967).

2.4   Summary

In this chapter, the flow mechanisms concerning flows over cavities have been presented. The flow mechanisms provide very useful information, which can be used for selecting numerical methods for computational aeroacoustics. The following list draws intermediate conclusions of the information gathered so far.

- Flows over cavities are classified in wake mode and shear-layer mode flows. Based on the information provided by Rowley et al. (2002), it is expected that the flow of the sky-dive tunnel entrance cavity is a shear-layer mode due to the turbulent boundary layer and the three dimensional character of the cavity. It is impossible to predict whether the flow is of the fluid-dynamic type or the fluid-resonant oscillation type, which is also not necessary and relevant at this point in the current study.

- The flow over a cavity includes effects from both the incompressible as the compressible regime, even at low free stream Mach numbers. Vortex shedding form the leading wall of the cavity is considered an incompressible feature. However, the feedback mechanism feeds the vortex shedding and due to the acoustic wave behaviour on which it feeds, the feedback mechanism is a compressible feature of this flow.

- The important geometric parameters, according to existing literature, are found in the dimensions of the cavity (L, W and D). The ratios of this parameters classify the cavity to be deep ($\frac{L}{D} < 1$) or determine whether the cavity behaves two dimensional ($\frac{L}{W} < 1$).

- Important flow parameters have been identified as Strouhal number (St_L), Reynolds number (Re_L, Re_D, Re_θ), Momentum) thicknes of upstream boundary layer ($\frac{\theta_0}{L}$, $\frac{\theta_0}{D}$, $\frac{\delta_0}{L}$) and the Free stream Mach number (M_∞).

Chapter 3

Cavity buffeting noise reduction

The reduction of cavity buffeting noise has been investigated for many applications. The main industries in which solutions for the flow problem regarding cavity buffeting noise are employed are the automotive, aviation and HVAC industry. The cavity buffeting noise, generated by the entrance cavity of the sky-dive tunnel, is in many ways comparable to the cavity buffeting noise generated by an open sunroof of a car or the opening of a wheel/weapon bay of an aircraft.

In this chapter, an overview of viable design solutions for the reduction (an possibly elimination) of cavity buffeting noise will be presented. The chapter starts with a short discussion about hearing thresholds, acceptable noise levels and viable reductions. After this, different design solutions and their working principles will be discussed.

3.1   Hearing thresholds and acceptable noise levels

Although infra-sound is not observed in the conventional way of describing hearing, the presumption that low frequencies can not be observed by the ear is a misconception (Broner, 1978).
In (Broner, 1978) the hearing thresholds of low frequency noise have been presented as in Figure 3.1. It can be seen that the hearing threshold for low frequency noise decreases with increasing frequency, from 140 dB at 1.5 Hz to approximately 90 dB at 20 Hz.

In the study of Gong et al. (2016), (objective and subjective) observations in a road-test show that cavity buffeting has vanished for the sunroof of a SUV. The optimization study has been performed in CFD and a reduction of 10 dB was found in the CFD study (130 dB to 120 dB).
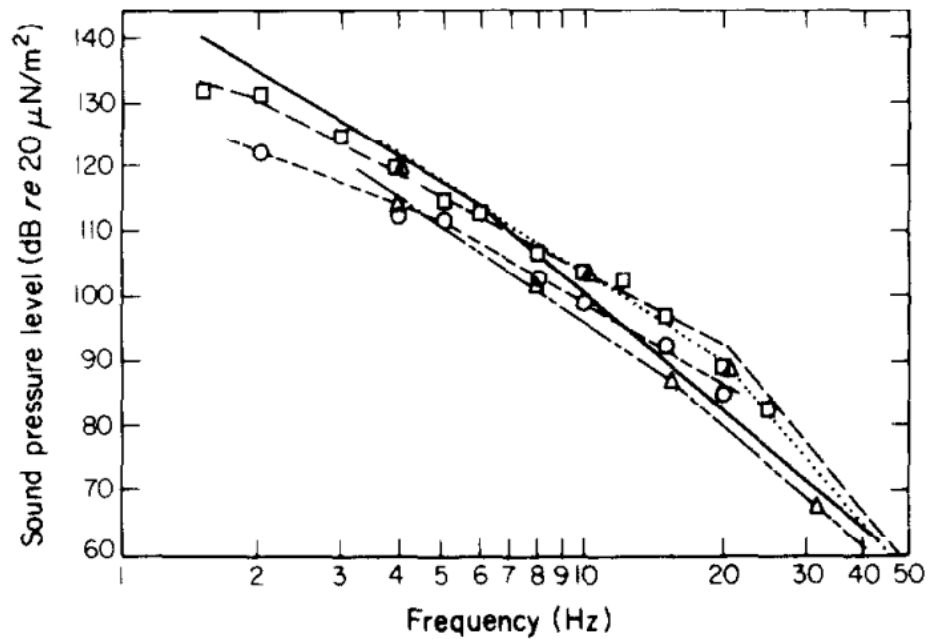
Figure 3.1: Low frequency hearing thresholds (Broner, 1978)

3.2   Shear Layer Alterations

A first category of noise reduction techniques is found in alterations to the shear-layer. In general, the thickening and lifting of the shear-layer affects the oscillation strength in the cavity. In this section, different methods to achieve shear-layer alterations which reduce cavity buffeting noise will be discussed.

3.2.1   Flow deflectors

As the comfort of passengers in the automotive industry is highly important and the complexity of automotive systems is rather kept low, different passive systems have been proposed and analysed in existing literature.

In the proceedings of Ribaldone et al. (2006), the performance of a flow deflector upstream of the cavity (sunroof opening) has been investigated by numerical simulation. The deflector is an add-on on the roof of the car. Both the clean geometry and geometry with deflector are shown in Figure 3.2. The same images show a slice of instantaneous velocity magnitude. It can be seen that the deflector leaves a bigger wake than the clean geometry, which protrudes further in the free stream flow field.

In Figure 3.3, the power spectrum of the pressure fluctuations has been shown. A serious suppression of the buffeting tone has been established with the flow deflector. Due to confidentiality reasons, the units of the y-axis have not been plot, which makes it difficult to quantify the per-

formance of this solution.
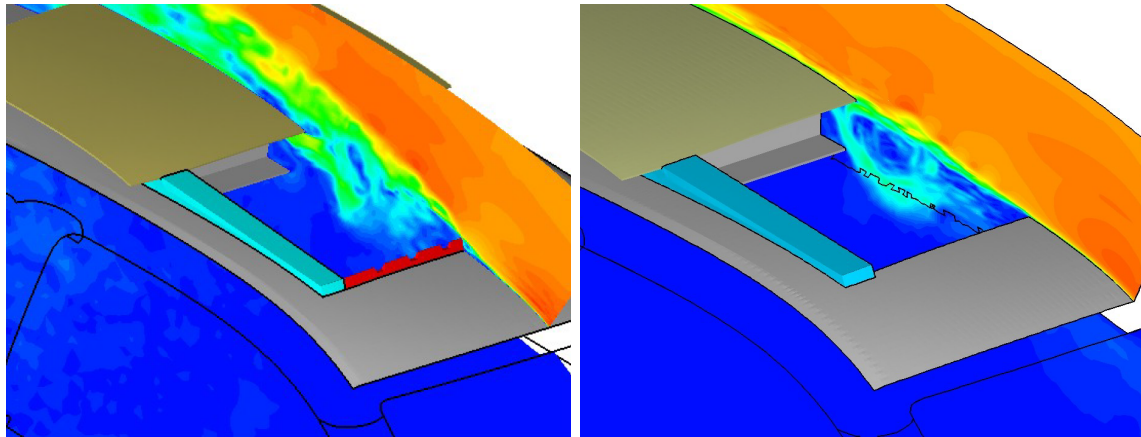
(a) Geometry with deflector.   (b) Clean geometry.

Figure 3.2: Comparison of influence of flow deflector on flow field (Ribaldone et al., 2006)(slice of instantaneous velocity).
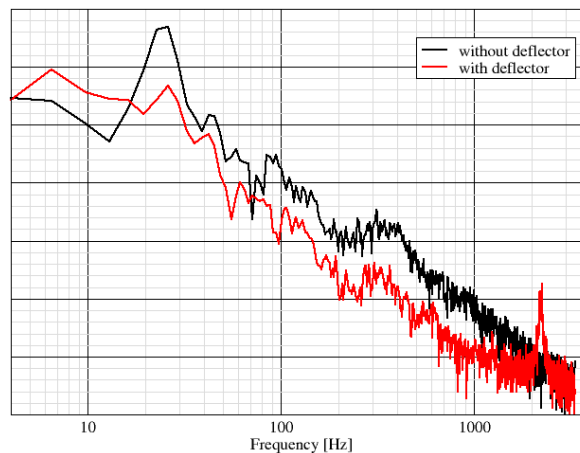
Figure 3.3: Power spectrum results, with and without deflector (Ribaldone et al., 2006)

Other research within this same topic has been performed by Kook (2008). In this study, Particle Image Velocimetry has been applied to the flow over an open sunroof. Rather than a flat cross-sectional shape as shown in Figure 3.2, the geometries discussed by Kook are defined by a tubular cross section as shown in Figure 3.4. The measurements by Kook are used in order to understand the noise suppression of the flow deflector. It was found that noise suppression becomes more effective with increasing protrusion of the free stream flow.

For the case where a deflector was employed (at most protrusion), the boundary layer detached tangential to the upper surface of the deflector, keeping it higher above the cavity than the case in which no deflector had been used.
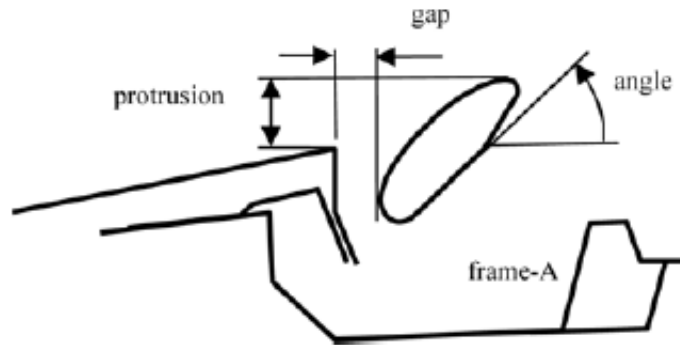
Figure 3.4: Flow deflector geometry (Kook, 2008)

Comparing the flows around two deflectors (lowest protrusion and highest protrusion), an increase in mass-flux trough the gap (see Figure 3.4) was found with increasing protrusion. Due to this increase mass flux trough the gap, the shear layer thickness was increased, which lowers the velocity gradient over the shear layers and consequently the strength of the vortex which introduced buffeting.

Despite the clear noise suppression by flow deflectors, the method is not favourable for a sky-dive tunnel. For many sky-dive tunnels it is known that flow deflectors affect the performance of the tunnel drastically. Flying above and around the door is hardly possible. This effect is also observed in Figure 3.2, in which a large wake is found behind the deflector. For a good performance above and a around the entrance, it is essential that the velocity field is only minor affected by the buffeting retrofit design.
On the other hand, the suppression mechanism is fairly simple to achieve: on simply increases the thickness of the shear-layer. When this could be achieved in a more controlled fashion it might be a suitable contribution to buffeting noise reduction.

3.2.2 Upstream dimples

Addressing similar issues which withholds the use of flow deflectors for the noise suppression in sky-dive tunnels (increased drag on cars due to the bigger wake), Wang et al. (2016) proposed to exploit a different technique: an array of dimples, upstream of the cavity, as presented in Figure 3.5.

Surprisingly the mechanism which suppresses the noise works similar to the mechanism which was found at the investigation of the flow deflector. The dimples in the surface thicken the boundary layer upstream, which results in a thicker shear layer over the cavity. A thicker shear layer results in a lower velocity gradient over the shear layer, which partially suppresses the rotating nature of the shear layer.

The upstream dimples reduced sound pressure levels by approximately 25 dB and a discrete peak was not found compared to a smooth upstream surface. The article shows that the oscillating
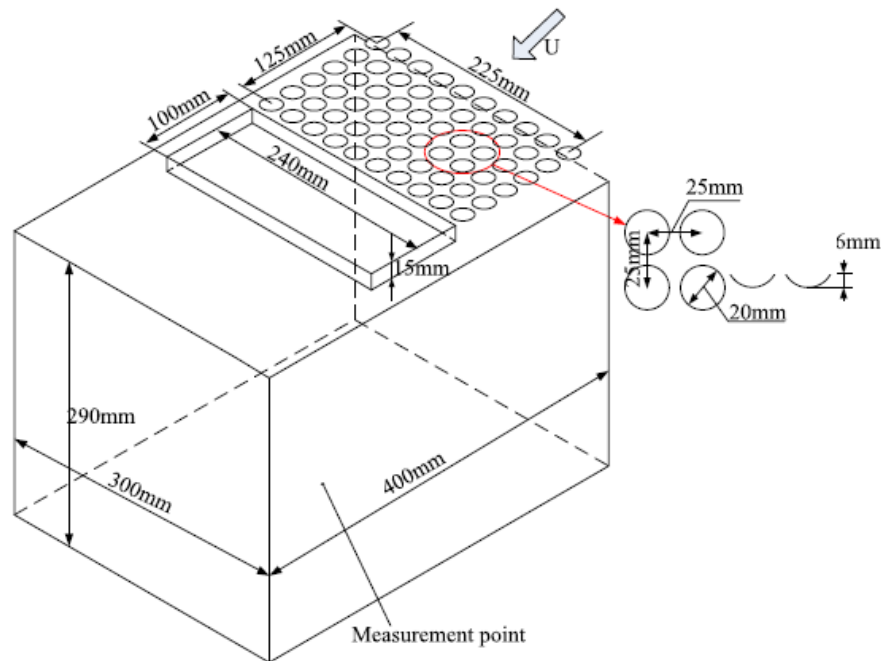
Figure 3.5: Dimpled geometry upstream of the cavity (Wang et al., 2016)

mechanisms were suppressed (almost) fully. These results are promising for the use in a newly built sky-dive tunnel, as a rather simple part can be added to the tunnel containing the dimples in an embedded geometry. However, as retrofit solution, this would be difficult to apply.

Missing information is the influence of the dimples on the downstream velocity field. This information is essential for the assessment of the applicability of the performance of this method to sky-dive tunnels.

3.2.3 Control cylinder

In Omer and Mohany (2015), a rather special form of a flow deflector is used, which in fact employs a slightly different mechanism in order to disturb the resonance/vortex shedding over the cavity opening. A cylinder is placed upstream of the cavity.

In an experiment, by Omer and Mohany (2015), it was found that the vortex shedding of the cylinder interacts with the vortex shedding over the cavity opening. It appears that the vortex shedding, induced by the cylinder, reduced the correlation coefficient of shear-perturbations in span-wise direction. Form these results it can be deduced that the shear-layer is disturbed at the leading edge of the cavity which subsequently reduced the tendency for acoustic excitation. This mechanism is visualised in Figure 3.6. Next to this it was found that the cylinder increased the momentum thickness of the shear-layer, which is a similar effect as the normal flow deflectors.

Various positions and diameters of the cylinder have been investigated. Most of the positions
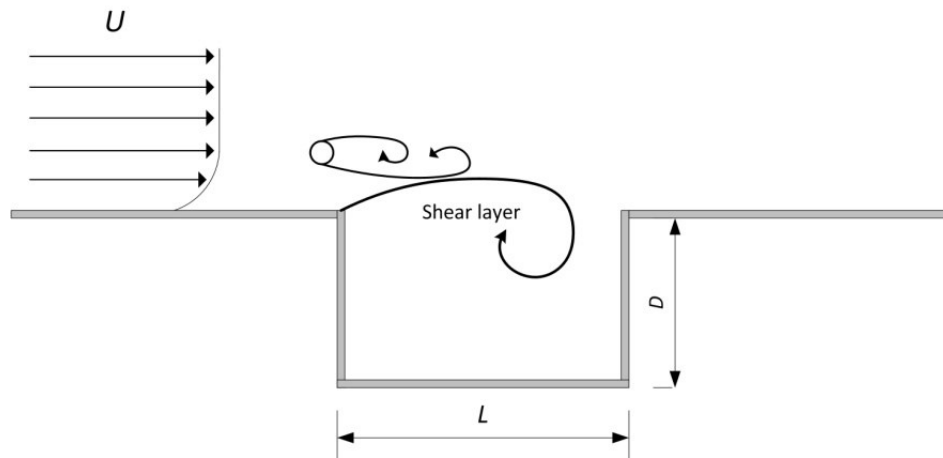
Figure 3.6: Schematic representation flow mechanism for noise suppression control cylinder (Omer and Mohany, 2015)

and diameters show a reduction in acoustic pressure. The magnitude of the reduction is highly dependent on the position and diameter of the cylinder.

3.2.4   Spoilers

Another possible solution, which potentially removes periodicity from the shear layer and thickens it are spoilers. Bolduc et al. (2013) presents the results of different spoiler configurations on the upstream edge of an axis symmetric ducted cavity.

Most promising results were found for the spoilers which were named delta spoilers. These spoilers were placed in converging pairs. The geometry, which has been presented Figure 3.7(a), suppresses the acoustic resonance of the cavity for a wide range of operating velocities, which can be seen in Figure 3.7(b).

As for many of the solutions found, the impact on the velocity field downstream of the cavity has not been investigated.

(a) Geometry for delta spoil-   (b) Acoustic pressure comparison.
ers.
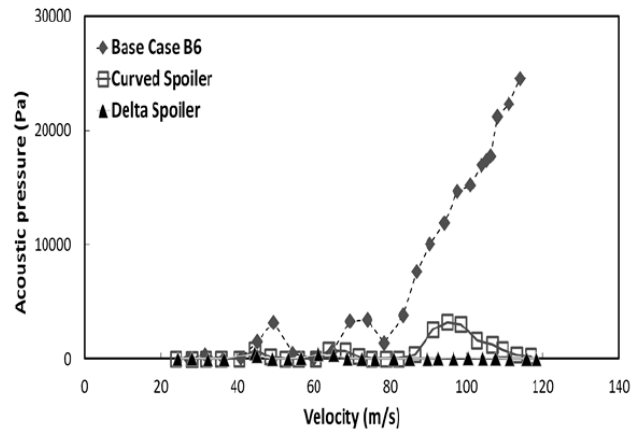
Figure 3.7: Leading edge delta spoilers, used by Bolduc et al. (2013) and accompanying acoustic
pressure results.

3.3 Impingement Alterations

A second method for cavity buffeting noise reductions is found in alterations of the impingement
mechanism. In this section, different methods to achieve reduction of cavity buffeting noise, by
alteration of vortex impingement on the trailing edge of the cavity, will be discussed.

3.3.1 Trailing edge shape change

A different method of suppressing the self-sustained oscillation has been found in adapting the
shape of the edge of the cavity geometry.
In the article of Omer et al. (2015), the effect of varying geometry parameters has been investigated
for different free stream velocities and therefore different Mach numbers and Reynolds numbers.
The different shapes are shown in Figure 3.8.

The results, in the format of acoustic pressure are presented in Table 3.1. It has been observed
that for this particular cavity, the acoustic pressure decreases by introducing a chamfer at the
trailing edge. The acoustic pressure keeps decreasing until an angle of 135 $[deg]$ has been reached
at which the acoustic pressure has been reduced approximately by a factor 4, which corresponds
to a reduction of 12 dB. Increasing the angle further increases the maximum acoustic pressure.
A similar investigation has been conducted for the leading edge and the combined leading and
trailing edge. It has been found that a leading edge chamfer drastically increases the maximum
acoustic pressure by 6.4-7.1 dB.
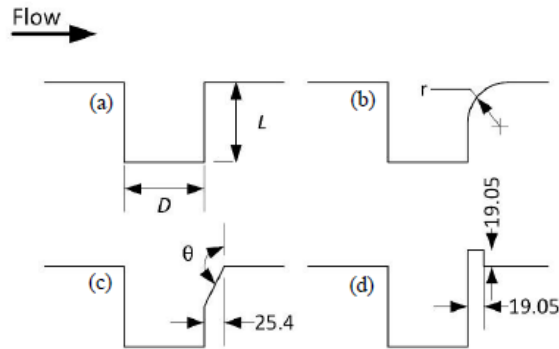
Figure 3.8: Tested edge alterations: a) Baseline cavity b) rounded trailing edge c) chamfered trailing edge d) Stepped trailing edge (results not presented) (Omer et al., 2015)

3.3.2 Flow deflector in cavity

Continuing on the study of computational fluid dynamics as a tool for the prediction of cavity buffeting noise, Langtry and Spalart (2008) proposed a cavity buffeting noise reducing solution as presented in Figure 3.9. A baffle device is used to deflect the shear-layer outwards, reducing the strength of the impingement on the trailing edge and preventing the shear-layer to deflect inwards. This design results in the suppression of feedback mechanism and the working principles a comparable to those of the chamfer in Omer et al. (2015).

The numerical and experimental results of this study are shown in Figure 3.10. Langtry and Spalart (2008) concluded that the (what appears to be the) buffeting peak in the default geometry (15 Hz) has been largely reduced in the case with the baffle device (20 dB in CFD, 33 dB in experiment).

A missing aspect in the conclusions is the effect on a shift of frequency. Installing this baffle devices obviously affects the length scale of the cavity. Keeping the Strouhal number the same (only affected by Mach number), the buffeting frequency has to rise compared to the default geometry. This would explain the higher frequency being the dominant peak in the new experimental spectrum. The small peak still being present at the location of the old buffeting peak (15 Hz) could be accounted for by considering that the baffle device does not cover the full span of the cavity, leaving a small part of unaltered cavity.

Table 3.1: Results summary adapted cavity shapes (Omer et al., 2015) (LE = Leading Edge, TE = Trailing Edge)

Geometry	Parameter	LE/TE	Maximum acoustic pressure [Pa]
Baseline	-	-	2200
Chamfer	107 deg	TE	1200
	120 deg	TE	700
	135 deg	TE	530
	150 deg	TE	1050
	120 deg	LE	4600
	135 deg	LE	3550
	150 deg	LE	5000
	120 deg	LE+TE	1900
	135 deg	LE+TE	1500
	150 deg	LE+TE	1150
Radius	12.7 mm	TE	1500
	12.7 mm	LE	4200
	12.7 mm	LE+TE	2500
	25.4 mm	TE	1000
	25.4 mm	LE	4200
	25.4 mm	LE+TE	4000
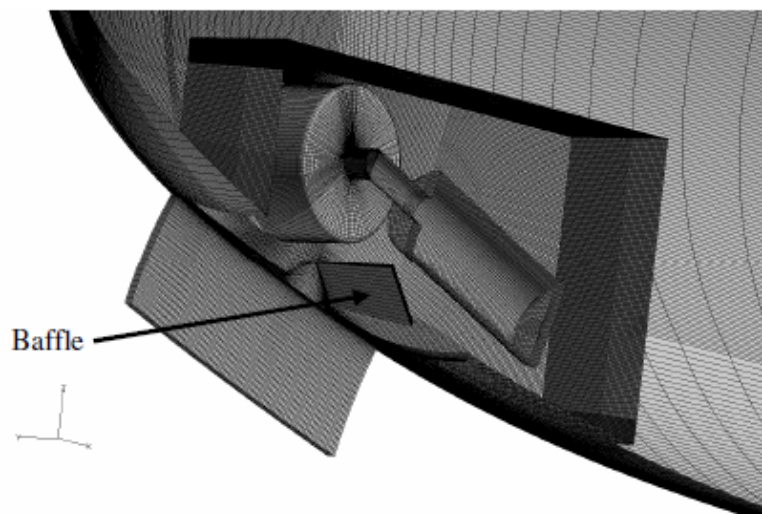
Figure 3.9: Internal flow deflector design (Langtry and Spalart, 2008)

(a) Default geometry.   (b) Geometry including baffle device
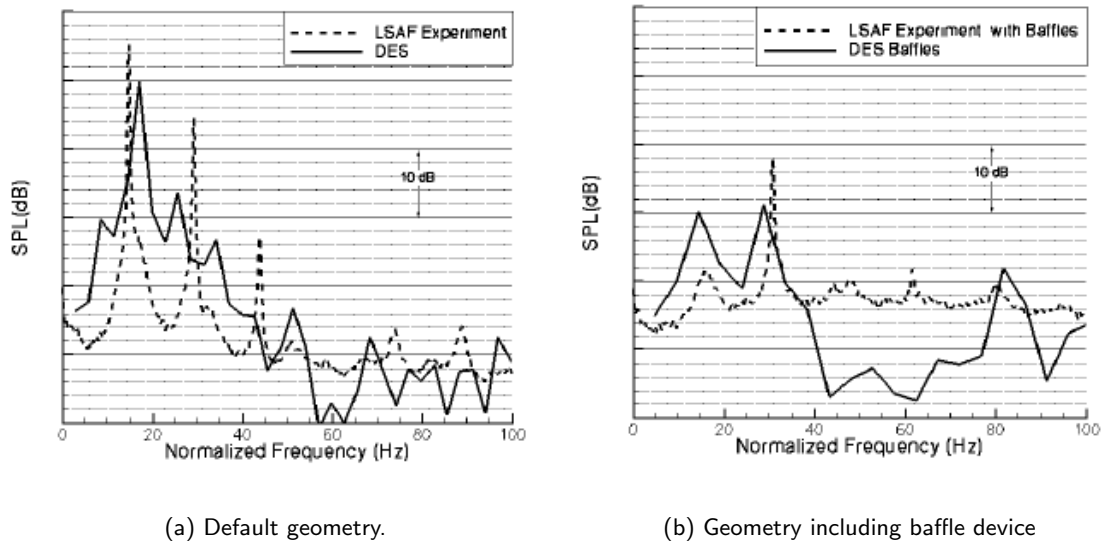
Figure 3.10: Numerical and experimental results of default geometry and internal flow deflector (Langtry and Spalart, 2008)

3.4 Summary

Various geometries with the purpose of noise suppression have been investigated in previous researches. In the following the conclusions for this part of the literature research have been listed.

- Mainly two mechanisms for the suppression of buffeting noise (and therefore cavity oscillations) have been found in existing literature.

  The first of which is altering the shear-layer over the cavity. Thickening this layer results in a smaller velocity gradient over the shear-layer. Subsequently, the rotating nature of the shear-layer is (partially) suppressed which results in a weaker vortex over the cavity. The pressure fluctuations, introduced by this weaker vortex are much smaller than

  The second mechanism is suppressing the feedback mechanism. By changing the shape/design of the edges of the cavity, the strength of the perturbations, introduced by vortex impingement can be altered. Subsequently the sound generation of the complete cavity is largely reduced.

- Both mechanisms show strong interaction. When thickening the shear layers, one also influences the impingement point on the down stream edge (more towards the free-stream flow). Which thereby also suppresses the feeback mechanism.

- For both mechanisms, existing literature shows different effectiveness for different solutions. For the suppression of the feedback mechanism, the rounded trailing edge seems to be most effective. On the other hand, for the thickening the shear-layer, whilst with minimal effect on the flow distribution of the sky-dive tunnel, the dimples (golf-ball pattern) seems to be most effective because of the relative low level of complexity and the .

- For each mechanism of noise suppression, several different solutions have been assessed in existing literature. Due to computational expensive simulations and the expenses of wind tunnel tests, no clear and complete sweep of parameters has been investigated. Next to this, the combined effect of a thickened shear-layer and the suppression of the feedback loop has not been investigate thoroughly.

Part II

Methodology

Chapter 4

Numerical set-up

In order to asses the performance of buffeting noise reducing solutions, a numerical set-up which is accurate in the prediction of buffeting noise reduction is required. In this chapter, the choices regarding the numerical set-up will be discussed.

4.1 Computational Fluid Dynamics

In Chapter 2 it has been indicated that part of the flow mechanisms (the feedback mechanism) is of compressible nature. Evidently, to capture this phenomenon, the compressible Navier-Stokes equations have to be used. This assumption is confirmed by studies of Inagaki et al. (2002) and Farkas and Paál (2015) which indicate the inaccurate prediction of cavity buffeting noise by incompressible solvers.

In this section the physics and modelling applied in computational fluid dynamics is explained.

4.1.1 Compressible Navier-Stokes

The physics of flow are described by the Navier-Stokes Equations (NS-Equations). These equations have been described in Equations (4.1) to (4.3) using Einstein notation (White and Corfield, 2006). (Note: the energy equation is the energy equation found in the source code of OpenFOAM, this is not necessarily the most physically complete version)

$$\frac{\partial \rho}{\partial t} + \frac{\partial \rho u_i}{\partial x_i} = 0 \tag{4.1}$$

$$\frac{\partial \rho u_i}{\partial t} + \frac{\partial}{\partial x_j} \left(\rho u_i u_j + p \delta_{ij} - \tau_{ij} \right) = 0 \tag{4.2}$$

$$\frac{\partial \rho h}{\partial t} + \frac{\partial}{\partial x_j} \left(\rho u_j h \right) + \frac{\partial \rho K}{\partial t} + \frac{\partial}{\partial x_j} \left(\rho u_j K \right) + \frac{\partial p}{\partial t} = -\frac{\partial q_j}{\partial x_j} \tag{4.3}$$

For convenience, the energy equation has been defined using enthalpy instead of total enthalpy, such that the non-linear term of specific kinetic energy ($K = \frac{|U|^2}{2}$) can be used explicitly in the same time-step.

The equations described in Equations (4.1) to (4.3) have to be supplemented with models in order to find closure of the problem. The first model is defined for τ_{ij} in Equation (4.4), which complements terms in the momentum equation (Equation (4.2)). For convenience, and the fact that the flow mechanisms are mainly incompressible, the (laminar) viscosity μ is assumed to be a constant.

$$\tau_{ij} = \mu \left(\frac{\partial u_i}{\partial x_j} + \frac{\partial u_j}{\partial x_i} \right) - \frac{2}{3} \mu \frac{\partial u_k}{\partial x_k} \delta_{ij} \tag{4.4}$$

Second a heat flux model to complement the energy equation (Equation (4.3)), which has been defined as Equation (4.5). In which α resembles the thermal diffusivity and h resembles enthalpy.

$$q_i = -\alpha \frac{\partial h}{\partial x_i} \tag{4.5}$$

Furthermore, the complete system has to be complemented with a coupling between pressure, temperature and density, which is provided by the ideal gas law, presented in Equation (4.6).

$$p = \rho R T \tag{4.6}$$

In which R is the specific gas constant.

4.1.2 Turbulence closure

When discretising Equations (4.1) to (4.3), without additional modelling (hence direct numerical simulation), grid spacing requirements which are infeasible within the computational resources of

the project have to be met (Hulshoff, 2015). In order to stay within the computational resources of the project, additional modelling in order to capture turbulent effects has to be used. Several classes of methods exist such as large eddy simulation (LES), detached eddy simulation (DES) and Reynolds averaged Navier Stokes (RANS). For the Reynolds numbers involved in this project, LES is computationally too expensive (Spalart et al., 1997), therefore DES will be used. DES methods are designed to resolve turbulent scales (LES) away from the wall (separated flow regions) and model turbulence near wall (RANS).

In this section, further considerations introduced by DES methods starting with the principle of LES filtering, after which the sub-grid scale (SGS) and RANS model is discussed and the filtered Navier-Stokes equations are defined.

LES and Favre filtering

As specific regions in this technique rely on Large Eddy Simulation, LES filtering has to be introduced.

Filtering in LES is used to distinguish between resolved scales and modelled scales. In general, various shapes can be used. The filtering operation is defined as the convolution integral of variable ϕ and filter function G as presented in Equation (4.7) (Hulshoff, 2015).

$$\tilde{\phi}(x,t) = \int_{\Omega} \phi(y)G(x-y)dy \tag{4.7}$$

The most used filter is the top-hat filter, which is defined in Equation (4.8).

$$G(x) = \begin{cases} 1/\Delta & if |x| \leq \Delta/2 \\ 0 & otherwise \end{cases} \tag{4.8}$$

Many CFD solvers, including OpenFOAM, do not perform an explicit filtering operation. Instead of a specified Δ, the mesh is used as an implicit top-hat filter. If Δ is defined as a cell length, all eddies with a length scale larger than $\Delta/2$ are filtered out automatically (Hulshoff, 2015).

Furthermore, variable ϕ now consist of a low frequency (resolved) part and a high frequency part shown in Equation (4.9).

$$\phi = \tilde{\phi} + \phi'' \tag{4.9}$$

For compressible flows, Favre filtering is applied, which indicates density weighting of the variables,

as defined in Equation (4.10) (Garnier et al., 2009).

$$\overline{\rho\phi} = \bar{\rho}\tilde{\phi} \qquad (4.10)$$

SGS and RANS model

The RANS model, which is used in the design of the DES method, has been formulated by Spalart et al. (1994). The RANS model constitutes one transport equation for a variable closely related to turbulent viscosity.

$$\frac{\partial \tilde{\nu}}{\partial t} + \frac{\partial}{\partial x_j}(\tilde{\nu}u_j) = C_{b1}[1 - f_{t2}]\tilde{S}\tilde{\nu} + \frac{1}{\sigma}\{\nabla \cdot [(\nu + \tilde{\nu})\nabla\tilde{\nu}] + C_{b2}|\nabla\tilde{\nu}|^2\}$$
$$- \left[C_{w1}f_w - \frac{C_{b1}}{\kappa^2}f_{t2}\right]\left(\frac{\tilde{\nu}}{d}\right)^2 + f_{t1}\Delta U^2 \qquad (4.11)$$

For further definitions of variables, constants and equations, one can refer to Appendix A. It can be found that in the transport equation (Equation (4.11)), the destruction term (third term on the right hand side) is dependent on wall distance d. This term is the departure point of the formulation of the hybrid RANS-LES model designed in Spalart et al. (1997).

First a the wall-distance d is replaced with a new variable $\tilde{d}$ defined by Equation (4.12).

$$\tilde{d} = min(d, C_{DES}\Delta) \qquad (4.12)$$

For which the following definitions apply.

- d: geometric wall-distance [m]
- C_{DES}: model constant [-]
- Δ: grid cell length scale [m]

The variable Δ is by implementation in OpenFOAM implicitly determined by the grid spacing. Typically, this variable is defined as presented in Equation (4.13).

$$\Delta = (\Delta x \Delta y \Delta z)^{\frac{1}{3}} \qquad (4.13)$$

Combining this definitions and the working principle of the transport equation of the SA RANS model, it can be found that the model is functioning as SGS model when $\Delta \ll d$ (indicating a cell is in LES mode) and functioning as SA RANS when $d \ll \Delta$ (indicating a cell is in RANS mode).

The definition of RANS/LES zondes, immediately indicates an issue with the use of DES: a grey area, in which the model does not behave as LES mode or RANS mode exists as transition region between a RANS and LES region. Another issue regarding the implementation of DES is the malfunctioning of the region indicator when refinement is inevitable in the boundary layer. When small scale cells are found, small isolated areas of LES mode are causing problems like flow separation in the boundary layer (Spalart, 2009).

A fix for this problem of isolated LES mode areas has been proposed by Spalart et al. (2006), named Delayed Detached Eddy Simulation. An alteration compared to the original formulation of DES has been introduced in the form of a blending function.

Using the internal length scale of the model, defined in Equation (A.6), with a slight modification as presented in Equation (4.14), a blending function has been composed as defined in Equation (4.15).

$$r_d = \frac{\nu_t + \nu}{\sqrt{u_{i,j} u_{i,j}} \kappa^2 d^2} \tag{4.14}$$

$$f_d = 1 - tanh((8r_d)^3) \tag{4.15}$$

Using the newly defined blending function, an alteration of the length scale d has been defined as in Equation (4.16).

$$\tilde{d} = d - f_d max(0, d - C_{DES}\Delta) \tag{4.16}$$

Although mathematical changes to the model are limited, a physical change has been established: length scale $\tilde{d}$ is not only grid dependent like in DES, but depends on turbulent viscosity as well.

It has been indicated by Spalart et al. (2006) that next to the "shielding" of the boundary layer, the change in DES limiter has also established a faster transition to LES mode, which eliminates part of the gray area.

4.1.3 Favre Filtered Navier-Stokes

In order to close the Navier-Stokes equations with a turbulence model, the Favre filtered Navier-Stokes equations are applied in OpenFOAM. The Favre filtered Navier-Stokes equations are pre-

sented in Equations (4.17) to (4.22).

$$\frac{\partial \bar{\rho}}{\partial t} + \frac{\partial \bar{\rho} \tilde{u}_i}{\partial x_i} = 0 \tag{4.17}$$

$$\frac{\partial \bar{\rho} \tilde{u}_i}{\partial t} + \frac{\partial}{\partial x_j} \left(\bar{\rho} \tilde{u}_i \tilde{u}_j + \bar{p} \delta_{ij} - \tilde{\tau}_{ji}^{tot} \right) = 0 \tag{4.18}$$

$$\frac{\partial}{\partial t} \left(\bar{\rho} \tilde{h} + \bar{\rho} \tilde{K} + \bar{p} \right) + \frac{\partial}{\partial x_j} \left(\bar{\rho} \tilde{u}_j \tilde{h} + \bar{\rho} \tilde{u}_j \tilde{K} + \frac{\partial \tilde{q}_j^{tot}}{\partial x_j} \right) = 0 \tag{4.19}$$

$$\tilde{\tau}_{ij}^{tot} = (\mu + \mu_t) \left(\frac{\partial u_i}{\partial x_j} + \frac{\partial u_j}{\partial x_i} - \frac{2}{3} \frac{\partial u_k}{\partial x_k} \delta_{ij} \right) \tag{4.20}$$

$$\tilde{q}_i^{tot} = -(\alpha + \alpha_t) \frac{\partial \tilde{h}}{\partial x_i} \tag{4.21}$$

In these equations, the turbulent properties (μ_t, α_t) have to be provided by a separate turbulence model (in this case the SA model).

Finally, the ideal gas law is filtered as well, which is presented in Equation (4.22).

$$\bar{p} = \bar{\rho} R \tilde{T} \tag{4.22}$$

4.2 Solver Algorithm and Discretisation

The solver relies on a PIMPLE algorithm for compressible flow Greenshields (2015). Finite Volume Method is applied in OpenFOAM for the discretisation, according to specified in Jasak (1996).

4.2.1 Solver Algorithm

The PIMPLE algorithm is used a segregated solver for velocity-pressure coupling. The PIMPLE algorithm has been outlined in Algorithm 1.

Algorithm 1 Compressible pimple algorithm

1: **procedure** TIMESTEP N
2:     *Initialise* $p^* = p^{n-1}, \rho^* = \rho^{n-1}, \phi^* = \phi^{n-1}, \nu_t^* = \nu_t^{n-1}, \alpha_t^* = \alpha_t^{n-1}$
3:     **for** n=1 to $n_{outer-correctors}$ **do**
4:         *Solve* discretised momentum equation → u*
5:         *Solve* discretised enthalpy equation → h*
6:         *Initialise* inner-loop $u^{**} = u^*, \rho^{**} = \rho^*$
7:         **for** j=1 to $n_{inner-correctors}$ **do**
8:             *Solve* pressure (continuity) equation → p**
9:             *Correct* velocity and flux with p^{**} → u^{**}, ϕ^{**}
10:           *Calculate* ρ^{**}
11:         *Initialise* next outer loop $p^* = p^{**}, u^* = u^{**}, \phi^* = \phi^{**}, \rho^* = \rho^{**}$
12:         *Solve* turbulence transport → ν_t^*, α_t^*
13:     *Save* time-step in time n $p^n = p^*, u^n = u^*, \phi^n = \phi^*, \nu_t^n = \nu_t^*, \alpha_t^n = \alpha_t^*$

The finite volume discretised momentum, continuity and enthalpy equation are presented in Equations (4.23) to (4.25). Further details about this discretised equations can be found in Appendix B and (Jasak, 1996).

Using the correct interpolation schemes (for obtaining face values from cell values), second order discretisation is ensured.

Discretised momentum equation

Using the discretisation technique, further elaborated on in Appendix B, the momentum equation has been discretised as presented in Equation (4.23).

$$
\frac{\frac{3}{2}(\bar{\rho}\tilde{\boldsymbol{u}})^n - 2(\bar{\rho}\tilde{\boldsymbol{u}})^{n-1} + \frac{1}{2}(\bar{\rho}\tilde{\boldsymbol{u}})^{n-2}}{\Delta t} V_P + \sum_f F\tilde{\boldsymbol{u}}_f^n - \sum_f (\mu_{eff})_f \, \boldsymbol{S} \cdot (\nabla \tilde{\boldsymbol{u}})_f^n =
$$
$$
- \sum_f S_f p_f^{n-1} + \sum_f \boldsymbol{S} \cdot \left(\mu_{eff} \left[\nabla \tilde{\boldsymbol{u}}^T - \frac{2}{3} tr(\nabla \tilde{\boldsymbol{u}}^T) \right] \right)_f^{n-1}
\tag{4.23}
$$

Discretised continuity (pressure) equation

Using the discretisation technique, further elaborated on in Appendix B, the continuity equation has been discretised as presented in Equation (4.24).

$$
\frac{\frac{3}{2}(\Psi\bar{p})^n - 2(\Psi\bar{p})^{n-1} + \frac{1}{2}(\Psi\bar{p})^{n-2}}{\Delta t} V_P - \sum_f \left(\frac{\bar{\rho}}{a_p} \right)_f \boldsymbol{S} \cdot (\nabla \bar{p})_f^n =
$$
$$
- \sum_f \boldsymbol{S} \cdot \left(\frac{\bar{\rho}}{a_p} \boldsymbol{H}(\tilde{\boldsymbol{u}}) \right)_f^{n-1}
\tag{4.24}
$$

Discretised enthalpy equation

Using the discretisation technique, further elaborated on in Appendix B, the enthalpy equation has been discretised as presented in Equation (4.25).

$$
\frac{\frac{3}{2}\left(\bar{\rho}\tilde{h}\right)^n - 2\left(\bar{\rho}\tilde{h}\right)^{n-1} + \frac{1}{2}\left(\bar{\rho}\tilde{h}\right)^{n-2}}{\Delta t}V_P + \frac{\frac{3}{2}\left(\bar{\rho}\tilde{K}\right)^n - 2\left(\bar{\rho}\tilde{K}\right)^{n-1} + \frac{1}{2}\left(\bar{\rho}\tilde{K}\right)^{n-2}}{\Delta t}V_P
$$
$$
+ \frac{\frac{3}{2}\left(\bar{p}\right)^n - 2\left(\bar{p}\right)^{n-1} + \frac{1}{2}\left(\bar{p}\right)^{n-2}}{\Delta t}V_P + \sum_f \boldsymbol{S} \cdot \left(\bar{\rho}\tilde{\boldsymbol{u}}\right)_f \left(\tilde{h}\right)_f^n - \sum_f \left(\alpha_{eff}\right)_f \boldsymbol{S} \cdot \left(\nabla\tilde{h}\right)_f^n
$$
$$
+ \sum_f \boldsymbol{S} \cdot \left(\bar{\rho}\tilde{\boldsymbol{u}}\right)_f \left(\tilde{K}\right)_f^n = 0
$$

$$(4.25)$$

4.3   Computational Aero Acoustics

In order to resolve acoustics in in CFD, in general three (classes of) methods exist. These methods are explained in the following.

- **Direct Noise Computation (DNC)**

  Direct noise computation is the most sophisticated technique for computational aero acoustics. Using the compressible Navier-Stokes equations, the acoustics are solved as a part of the flow field, introducing no further assumptions for the acoustics. Fluctuations in the pressure form the acoustic perturbations in the flow field. DNC is the most computational expensive method for aero acoustic computation (Colonius and Lele, 2004).

- **Hybrid methods**

  Hybrid methods rely on techniques in which the flow fields is solved separated from the acoustics (Colonius and Lele, 2004). Typically, low Mach number flows (in which the acoustics are dominated by the hydrodynamic pressure spectrum) are solved using incompressible flow after which a different technique is used to compute/solve the aero acoustics and propagation. Popular techniques for computing the acoustics are acoustic analogies of which Curle's analogy is implemented in OpenFOAM. Curle's analogy, which is only able to capture surface dipole sources. Acoustic analogies are typically used for computation of far-field acoustics, however Koschatzky et al. (2010) shows rather good agreement in the near field.

- **Stochastic reconstruction of noise**

  For stochastic reconstruction of noise, steady-state flow simulations are used. As aerodynamic noise mainly is produced by turbulent structures, the turbulent properties are used in a stochastic model for the prediction of broad-band noise (Bailly et al., 1995).

As indicated in Section 2.2, flows over cavities produce sound sources of both the dipole surface type and the monopole volume type. In order to accurately capture the sound sources, the hybrid

methods in OpenFOAM are not sufficient. Furthermore, broad-band noise is not of interest, as discrete peaks at low frequencies are expected, therefore stochastic reconstruction of noise is not applicable to the current study.

A DNC approach will be used for this study. By limiting the bandwidth of interest to 0-100 Hz, the computational expenses are limited. A similar approach was used by (Langtry and Spalart, 2009).

4.4   Domain truncation

In order to scale down on computational power, it is critical to truncate the domain of the sky-dive tunnel. As the cavity, formed by the waiting room, is responsible for the buffeting noise effects, the domain can be truncated such that this part is included. In Figure 4.1, both the complete tunnel (left) and the truncated domain (right) has been visualised.
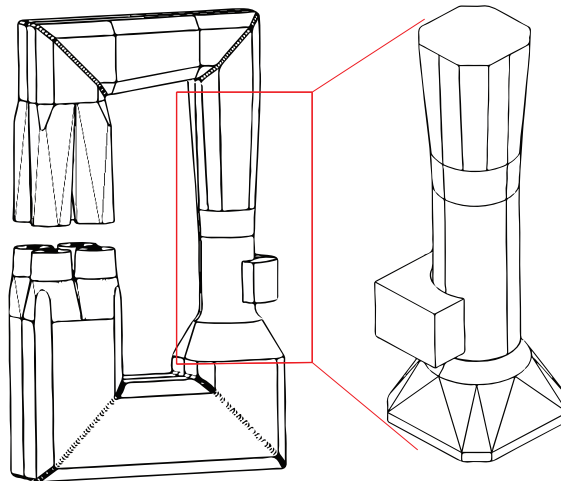

Figure 4.1: Truncation of the computational domain

As can be seen, the contraction, sky-dive section and expansion are included in the domain. As a possible consequence of the domain truncation, the flow might not be fully developed in the sky-dive section, which might be a discrepancy compared to the real tunnel. Consequently, boundary layers can be thinner influencing the oscillation strength of the shear-layer.

4.5   Boundary-Conditions

In order to solve the equations, it is needed to apply boundary conditions to both the artificial and physical boundaries of the domain. Physical boundary conditions are (in this case) applied to solid walls. Artificial boundary conditions are applied to the boundaries which are introduced

by truncating the domain (inlet and outlet). The boundary conditions, applied for this study are tabulated in Table 4.1.

Table 4.1: Overview boundary conditions

Regions (color)	Pressure	Velocity	Temperature	$\tilde{\nu}$	ν_t	α_t
Walls	zeroGradient	noSlip	zeroGradient	0	*	**
Inlet	zeroGradient	925 m^{3}s^{-1}	293.15K	0.05	calc.	calc.
Outlet	waveTransmissive	inletOutlet	inletOutlet	inletOutlet	calc.	calc.

ν_t and α_t are calculated results of $\tilde{\nu}$, which is the only turbulent variable for which is solved. Nevertheless, in order to reduce the computational cost, wall functions are applied such that correct values are found without excessive refinement near the wall. The boundary conditions applied for ν_t (*) is based on Spalding law of the wall (White and Corfield, 2006). For α_t a wall-function is used which calculates α_t based on the turbulent Prandtl number (Pr_t): $\alpha_t = \frac{\rho\nu_t}{Pr_t}$, where $Pr_t = 0.85$.

Next to these special boundary conditions, more straightforward conditions as zeroGradient (Neumann condition normal the to wall), noSlip (no-slip condition) and prescribed values can be found in Table 4.1. The inletOutlet conditions behaves as a switch between zeroGradient (when outflow is detected) and a prescribed value (when reversed flow is detected), which in this study will behave as a zeroGradient condition.

Last but not least, a special boundary condition is specified as pressure condition on the outlet: waveTransmissive. This boundary condition solves a partial differential equation on the boundary faces, in order to eliminate reflections and propagate disturbances which travel with wave velocity.

4.6 Grid Generation

In order to solve a flow problem in OpenFOAM, a grid has to be constructed. Beta CAE ANSA 17.0.0 will be used for the grid generation in this project. In this section, the different refinement levels for the different grids and regions in the grids are discussed.

For resolving turbulent scales in the shear layer, refinement of the shear-layer is necessary. Next to this, the acoustic properties regarding the feedback mechanism need refinement as well. Due to this requirements, three refinement boxes have been defined as in Figure 4.2. Box 1 and Box 2 represent refinement in the shear layer and the close surroundings of the shear layer. Where Box 3 represents the refinement of the waiting room, in which acoustic feedback is expected.

Based on Langtry and Spalart (2009), between 30 and 58 grid points per wavelength are required. The wavelengths can be estimated using the Rossiter modes. The modes are calculated using Equation (2.2), with the input from Table 4.2 and are presented in Table 4.3.

Before simulation it is not evident which Rossiter mode will occur for the current flow problem.

Table 4.2: Rossiter mode calculation input

Variable	Value	Units
L	2.3	m
M_∞	0.22	-
U_∞	70	ms^{-1}
n	1,2,3,4	-

Table 4.3: Estimated Rossiter modes with wavelength

Mode number	St_L [-]	Frequency [Hz]	Wavelength [m]
1	0.38	12.2	28.13
2	0.89	28.4	12.09
3	1.40	44.7	7.68
4	1.91	60.9	5.63

In order to test grid dependency, three different grid are constructed with different refinement lengths for the different refinement zones. The respective lengths of the three grids are defined as in Table 4.4.

Table 4.4: Different refinements for different refinement zones

Grid name	Box 1 [mm]	Box 2 [mm]	Box 3 [mm]
Coarse	24	100	140
Medium	20	90	130
Fine	12	50	70

Furthermore, refinement near the walls is required. Wall functions are used in this study. Refinement near the walls is adjusted such that non-dimensional wall-normal length (y^+) of the first cell centre is kept below 200 near the cavity opening by generating prism layers before meshing the remainder of the volume.
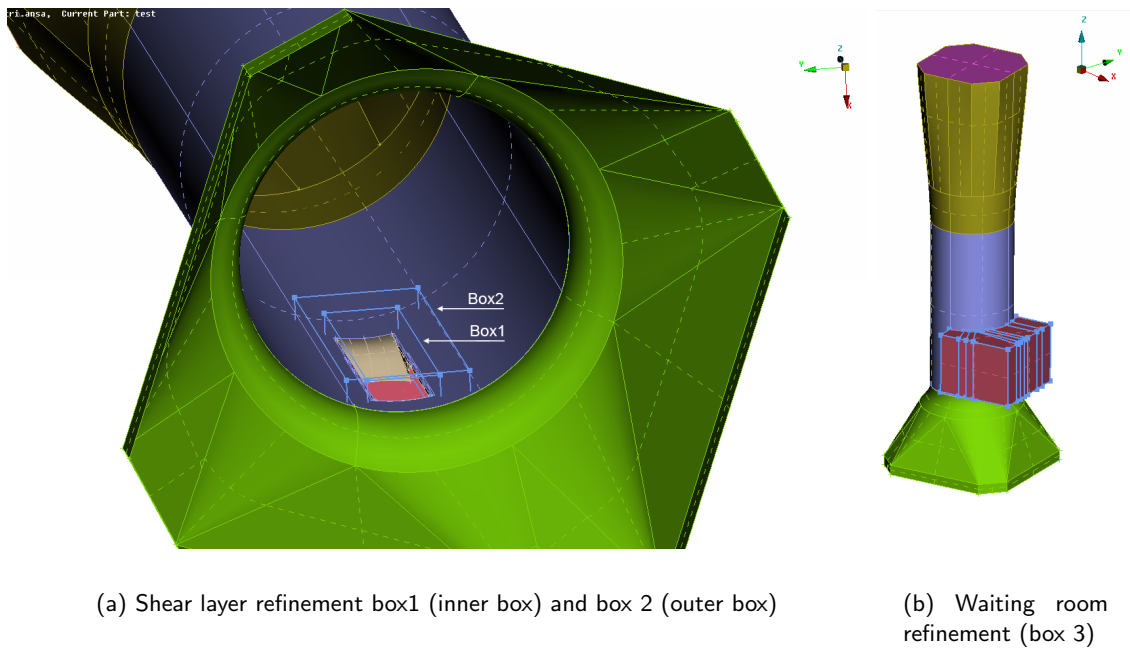
(a) Shear layer refinement box1 (inner box) and box 2 (outer box)

(b) Waiting room refinement (box 3)

Figure 4.2: The three main refinement zones

**Table 4.5:** Grid points per wavelength, box 3 (waiting room)

Grid name / Mode number	1	2	3	4
Coarse	200	86	54	40
Medium	216	92	59	54
Fine	401	172	109	80

4.7 Geometry

Different geometries will be tested in the numerical set-up. In this section, the current geometry will be presented after which the retrofit designs and the intended working principles will be discussed.

4.7.1 Current Geometry

The current geometry around the cavity opening in City sky-dive centre has been presented in Figure 4.3. The current geometry is a result of a design study, based on incompressible CFD, which showed to be highly effective in an inaccurate CFD set-up.
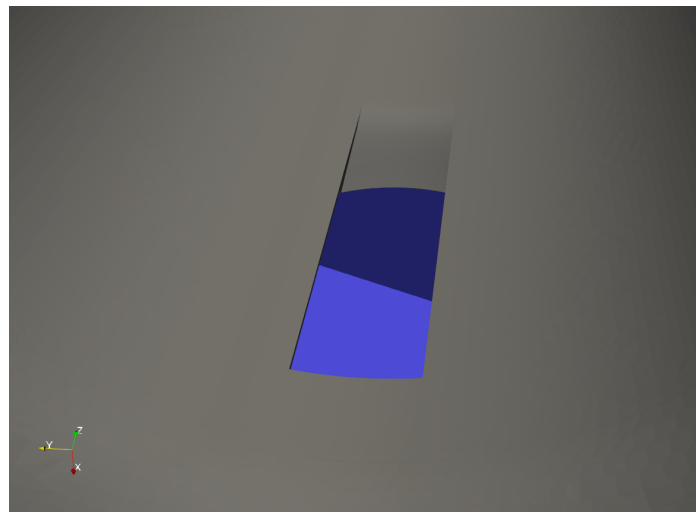
(a) Current cavity opening geometry
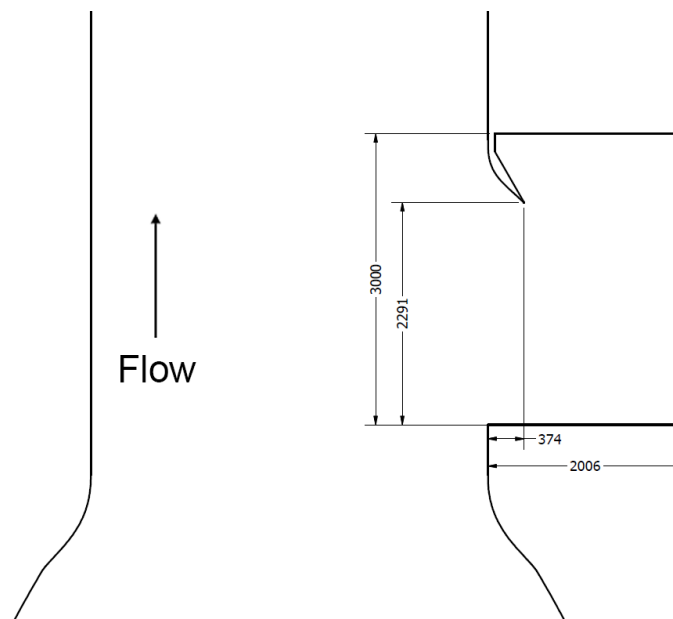
(b) Current cavity dimensions

Figure 4.3: Ineffective geometry of the current situation.

4.7.2   Retrofit Designs

A hypothesis regarding the ineffectiveness of the current situation has been formulated: the current trailing edge geometry does not protrude deep enough in the cavity, which allows a strong span-wise vortex to partially slip past the trailing edge, impinging on the ceiling of the waiting

room.

The following four alterations on the geometries are proposed in order to suppress the flow mechanisms which are responsible for cavity buffeting noise for the current situation.

1. Wing and span-wise cylinder: as found in literature, by lifting the shear layer, the large scale vortices are lifted out of the cavity opening, weakening the impingement of the large scale vortices.

   The geometries of the span wise cylinder and the wing have been presented in Figure 4.4 and Figure 4.5. The span-wise cylinder is defined as a cylinder of 60 mm diameter, positioned 60 mm from the wall (center to wall) and 90 mm from the floor of the cavity. The wing defined using a slightly cambered slender airfoil, with a chord length of 349 mm, positioned 152 mm from the wall of the tunnel (leading edge to wall) inclined at an angle of 9 degrees.

2. A wall normal cylinder: breaking down the span-wise vortex. Similar effects have been observed in literature with the use of delta spoilers (see Section 3.2.4).

   The wall normal cylinder, visualised in Figure 4.6, is positioned 110 mm from the cavity floor and has a diameter of 80 mm.

3. Trailing edge extension: preventing the large scale vortex to slip past the trailing edge by extending the existing shape.

   The trailing edge extension, visualised in Figure 4.7, protrudes 402 mm further into the cavity than the original trailing edge shape, and reduces the height of the opening by 403 mm.
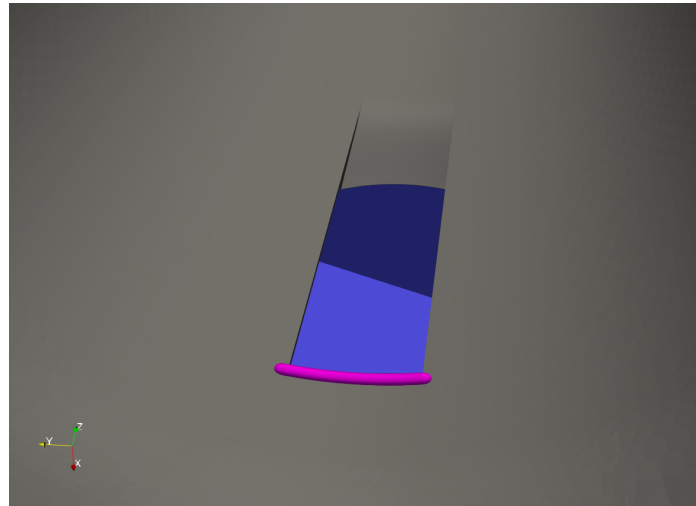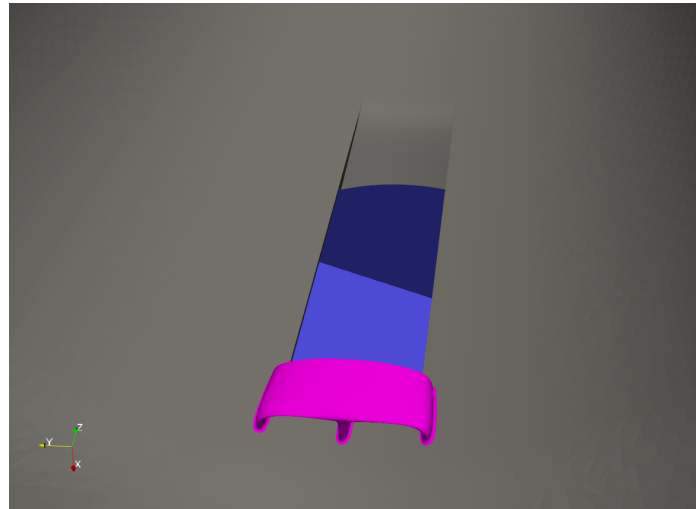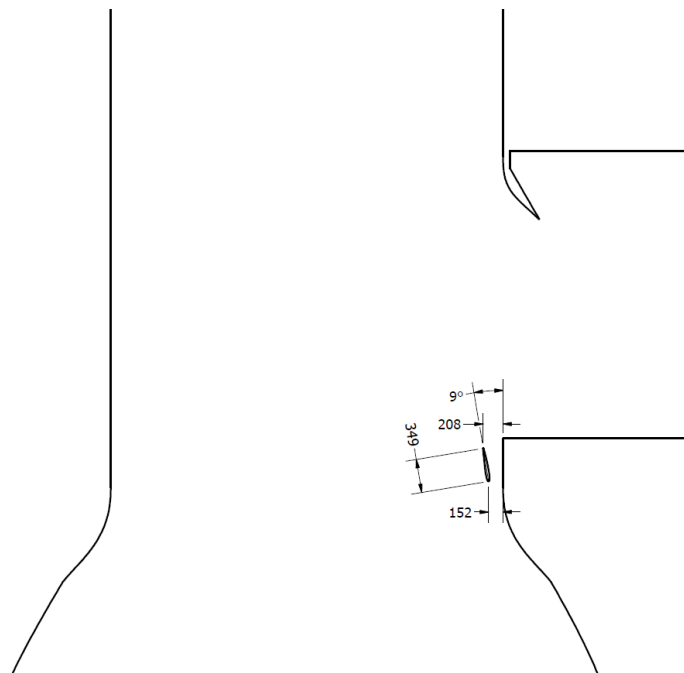
(a) Span-wise cylinder geometry
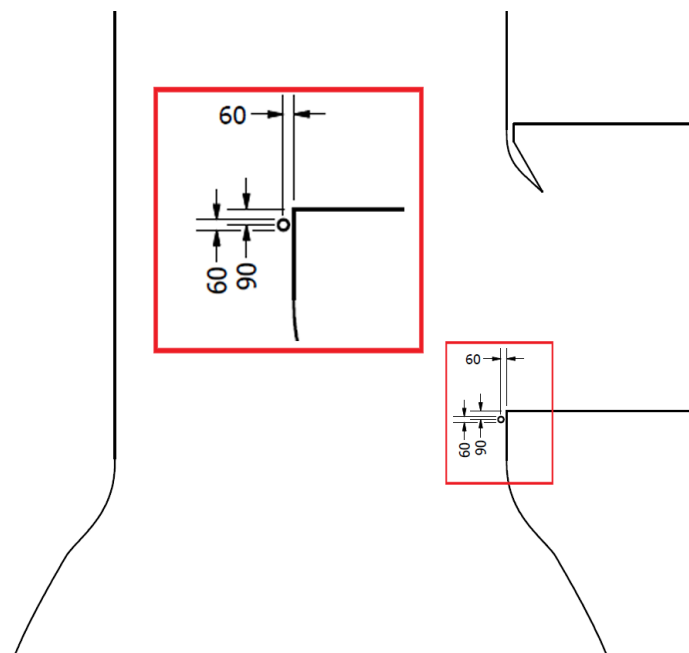
(b) Span-wise cylinder dimensions

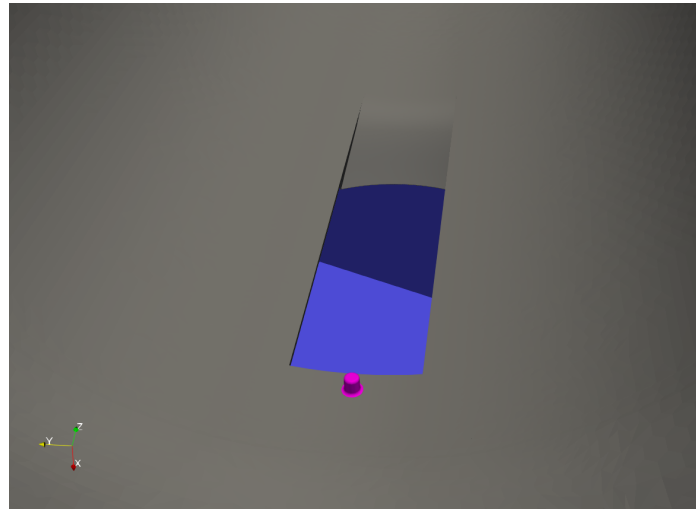**Figure 4.4:** Proposed span-wise cylinder geometry
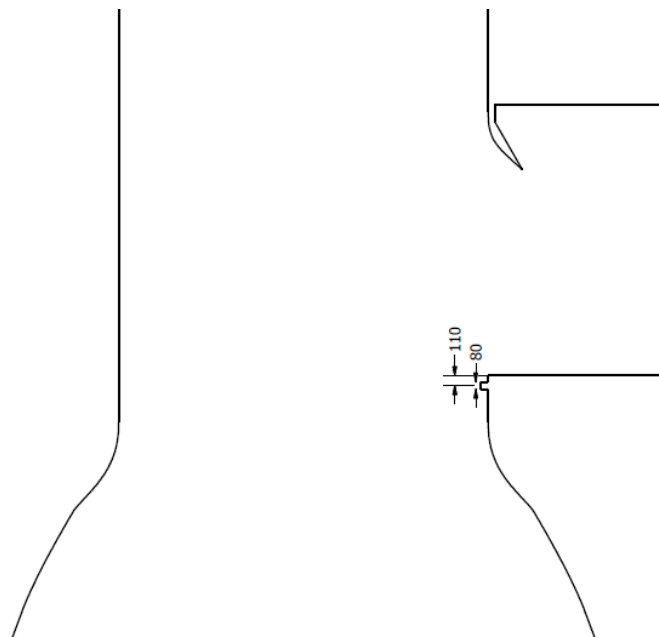
(a) Wing geometry

(b) Wing dimensions

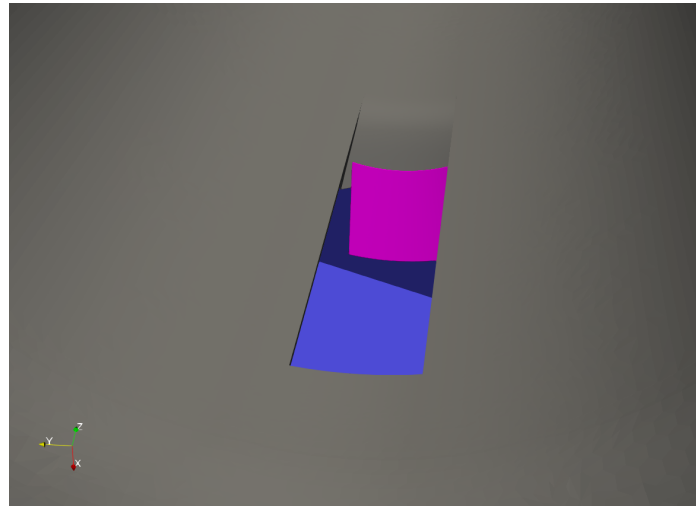**Figure 4.5:** Proposed wing geometry
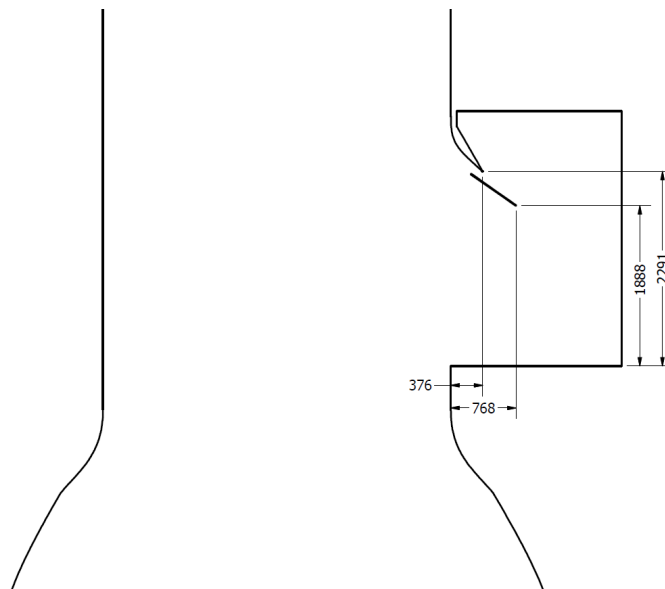
(a) Wall normal cylinder geometry

(b) Wall normal cylinder dimensions

Figure 4.6: Proposed wall normal cylinder geometry

(a) Trailing edge extension geometry

(b) Trailing edge extension dimensions

Figure 4.7: Proposed trailing edge extension geometry

Chapter 5

Experiment set-up

For the validation of the CFD set-up, it is critical to establish an experimental set-up which can quantify cavity buffeting noise. In this chapter, first the equipment and an overview of the experiment lay-out will be discussed. After which the influence of tube sizing, resonance and distortion compensation will be addressed.

5.1 Equipment and Set-up

A Scanivalve DSA3217 (presented in Figure 5.1(b)) is available for this project. This pressure scanner is able to scan multiple pressure probes. When set-up in binary mode, it is able to scan with a sampling frequency of 500 Hz (Scanivalve, 2009), which according Nyquist sample rate is sufficient to capture signals correctly up to 250 Hz (Ziemer et al., 1993).

The pressure scanner measures pressure relative to a reference port, which has to be lead to the outside of the cavity, such that the reference signal is as steady as possible. For data acquisition purposes, the pressure scanner has been equipped with an Ethernet port, which has to be connected with a PC directly. Data acquisition software called *Scantel* is used to download the data.

An overview of the placement of equipment during experiment has been presented in Figure 5.1(a). The overview indicates the need for the probe tubes to be routed to the outside of the waiting room. This means that rather long tubing is needed in order to reach for the correct locations. In the following section, the tube sizing and the influence on tube resonance will be discussed.
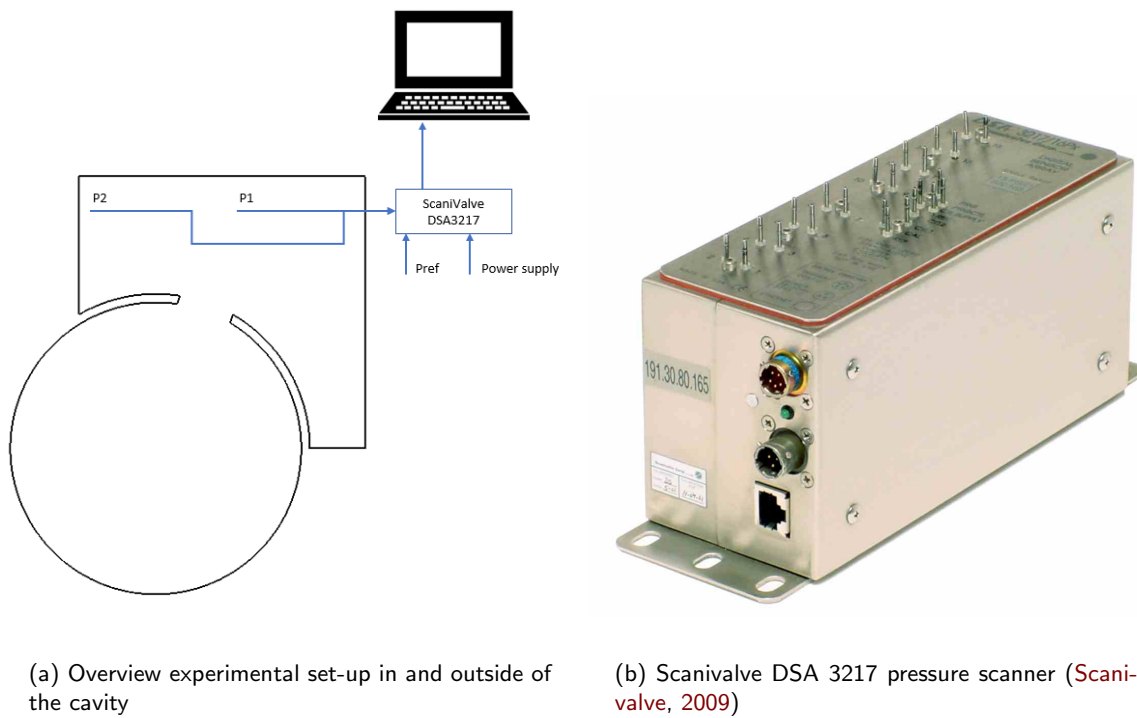
(a) Overview experimental set-up in and outside of the cavity

(b) Scanivalve DSA 3217 pressure scanner (Scanivalve, 2009)

Figure 5.1: Experiment set-up and used equipment

5.2   Tube Sizing and Resonance

For the measurement of transient pressure signals, it is critical to avoid tube resonance. Therefore careful sizing of the tubing is necessary. Bergh and Tijdeman (1965) describes a method for the determination of the occurrence of tube resonance for a given system volume. When Equation (5.1) holds, tube resonance is to be expected.

$$cot\left(\frac{fL}{a_0}\right) = \gamma\frac{V_v}{V_t}\left(\sigma + \frac{1}{k}\right)\left(\frac{fL}{a_0}\right) \tag{5.1}$$

Tube diameters are determined by the restrictions of connections on the pressure scanner. Tubing with a diameter of 3 mm has to be used to fit the connectors. Combining the values from Table 5.1 with Equation (5.1), the resonance tube length for the frequency range has been determined and presented in Figure 5.2.

It can be observed that for frequencies up to 100 Hz, no resonance should exist when the tubing length is kept under 3.8m. In order to be on the save side, tube lengths will be kept under 3m.

Table 5.1: Tube resonance length calculation input

Symbol	Description	Value	Units
f	Frequency	Variable: 10-100	Hz
a_0	Speed of sound	343.2	ms^{-1}
γ	Specific heat ratio	1.4	-
V_v	Measurement System Volume	8.462×10^{-6} (Pemberton, 2010)	m^3
V_t	Tube Volume	Function of length and diameter	m^3
σ	Relative System Volume Change	0.0012	-
k	Polytropic expansion constant	1.4	-
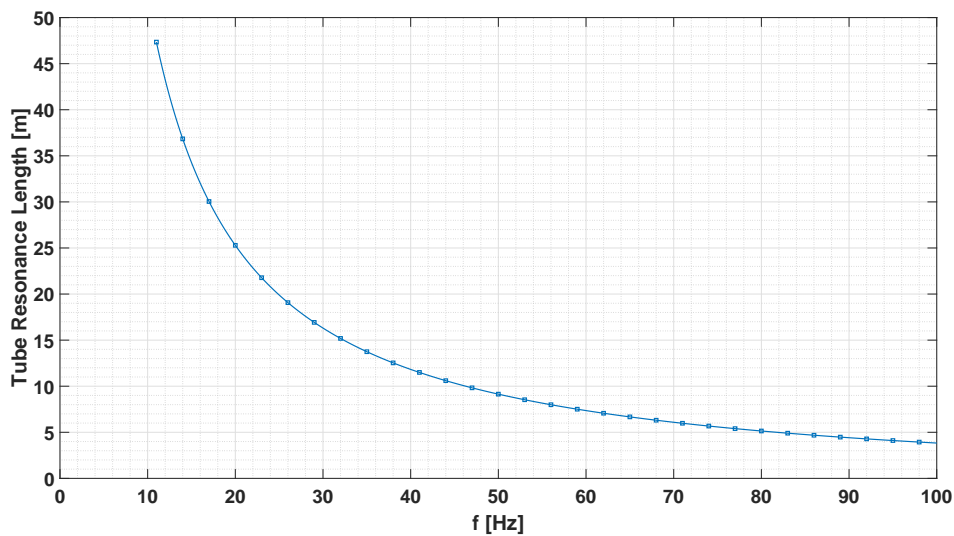
Figure 5.2: Resonance lengt as function of excitement frequency

5.3   Distortion Compensation

Distortion compensation has to be considered when a pressure scanner is used for the measurement of transient pressure signals. Bergh and Tijdeman (1965) formulated such a method. Assuming isentropic conditions in the tubing system, pressure ratio can be calculated for different frequencies using Equation (5.2), using input from Table 5.2.

$$\frac{p_1}{p_0} = \left[cos\left(\frac{fL}{a_0}\right) - \gamma \frac{V_v}{V_t}\left(\sigma + \frac{1}{k}\right)\frac{fL}{a_0}sin\left(\frac{fL}{a_0}\right) \right]^{-1} \tag{5.2}$$

After calculating the pressure ratios for frequencies between 0 and 100 Hz, a gain can be calculated using Equation (5.3), which can be added to the sound pressure levels, calculated from the raw
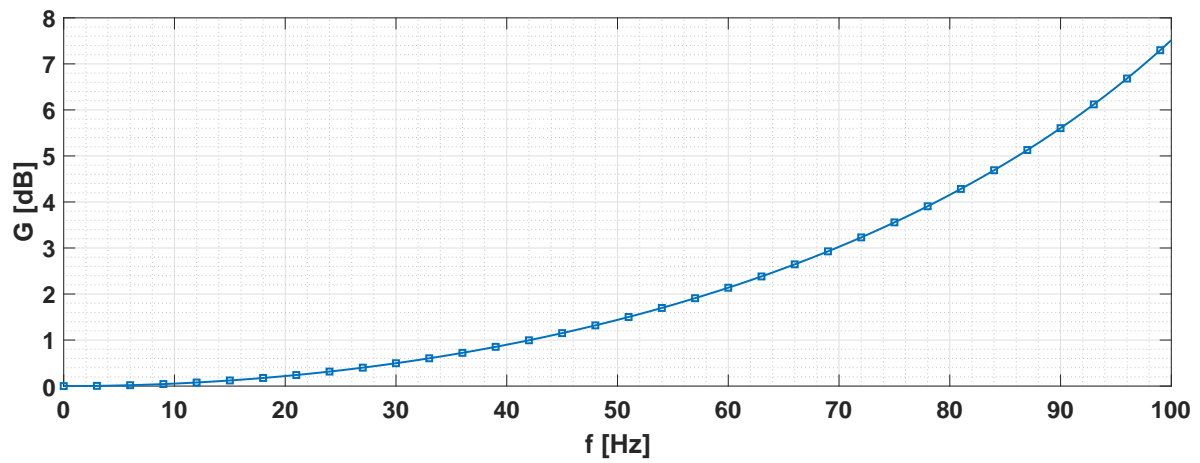
Table 5.2: Distortion compensation calculation input

Symbol	Description	Value	Units
L	Tube length	2.5	m
a_0	Speed of sound	343.2	ms^{-1}
γ	Specific heat ratio	1.4	-
V_v	Measurement System Volume	8.462×10^{-6} (Pemberton, 2010)	m^3
V_t	Tube Volume	Function of length and diameter	m^3
σ	Relative System Volume Change	0.0012	-
k	Polytropic expansion constant	1.4	-

signal.

$$G = 10 log_{10} \left[\left(\frac{p_1}{p_0} \right)^2 \right] \qquad (5.3)$$

The resulting frequency dependent gain has been shown in Figure 5.3.

Figure 5.3: Distortion compensation term as function of frequency

Chapter 6

Data Processing

Each simulation and experiment will supply a time dependent dataset. In order to provide an interpretation of the data, further processing is needed. In this chapter, the methodology and algorithms, used for further processing will be discussed in detail.

First a description of the post processing of pressure probes will be provided. After which visualisation techniques, for the purpose of identifying the flow mechanisms which are anticipated according to Chapter 2 will be discussed.

6.1 Pressure probes

One of goals of the project is to validate the numerical method for the use of cavity buffeting noise prediction. The experimental technique available (a pressure scanner) is only able to record time dependent (differential) pressure signals, which are difficult to compare quantitatively with simulation data. Therefore, a post-processing tool has been scripted in order to transform time dependent pressures to the frequency domain and create a sound pressure level spectrum.

The script which handles the probed pressure signals contains the following listed steps.

1. Read data: raw data in OpenFOAM output format or Scanivalve ASCII output is read into Matlab$^{\circledR}$.

2. Subtract Mean: the mean value of pressure is subtracted to isolate the fluctuating (time varying) part of the pressure, which represent cavity buffeting noise.

3. Windowing: the pressure signal is conditioned with a Hanning window.

4. Fast Fourier Transform: standard fast fourier transform algorithm of Matlab$^{\circledR}$ will be applied to the window conditioned signal.

5. Compute sound pressure level: the frequency domain pressure signal will be converted to a sound pressure level spectrum using Equation (6.1).

$$SPL = 10log_{10}\left(\left[\frac{p(f)}{p_{ref}}\right]^2\right) \tag{6.1}$$

6.2   Visualisation of flow mechanisms

In order to asses the simulation technique for the correctness of the flow mechanisms (and therefore as part of the validation of the numerical set-up) various visualisation techniques can be used. First the visualisation of vortex shedding, in simulation, will be discussed. Second the visualisation of the feedback mechanisms will be explained. Last the extraction of the flow mechanism from experiment data will be provided.

6.2.1   Vortex shedding

One of the main flow mechanisms, which is expected to be present in the current flow problem, is vortex shedding from the leading wall of the cavity. Multiple techniques for the detection of vortices exist. Example of such techniques are the minimum pressure criterion and the Q-criterion. A more complete technique for vortex detection is the λ_2-criterion (Jeong and Hussain, 1995), which can be computed directly as a post-processing step in OpenFOAM.

The λ_2-criterion is based on principle of a pressure minimum, similar to the pressure minimum criterion. The pressure minimum criterion fails due to two effects which have to be accounted for. The firs effect is caused by unsteady straining of the flow, which can cause a pressure minimum without rotation motions. The second effect is caused by the viscosity of a fluid, which is able to suppress a pressure minimum in the vicinity of vortices. The λ_2-criterion simply ignores these effects as shown in the following (Jeong and Hussain, 1995).

When taking the gradient of the Navier-Stokes equations, Equation (6.2) can be formulated based on the symmetric parts of the acceleration gradient (Jeong and Hussain, 1995).

$$\frac{DS_{i,j}}{Dt} - \nu S_{ij,kk} + \Omega_{ik}\Omega_{kj} + S_{ik}S_{kj} = -\frac{1}{\rho}p_{ij} \tag{6.2}$$

The first and second term of Equation (6.2) are causing the two effects mentioned before, which are the main contribution to the minimum pressure criterion to fail. For the λ_2-criterion , the first two terms are simply ignored. The remaining is to find the eigenvalues of $\boldsymbol{S^2 + \Omega^2}$. When two subsequent eigenvalues are found to be negative of this symmetric matrix, a vortex core exists. Suppose this matrix has eigenvalues $\lambda_1 \leq \lambda_2 \leq \lambda_3$ then two subsequent eigenvalues are found to

be negative when $\lambda_2 < 0$, hence the name λ_2-criterion . Although the λ_2-criterion is the most usable method in OpenFOAM for determining whether a cell belongs to a vortex core, it can be hard to distinguish between vortices, when multiple vortices exists near each other (Jiang et al., 2005).

A post-process utility of OpenFOAM, which automatically reads the velocity field and calculates λ_2 will be used. After this calculation, Paraview is used to visualise the location and movement of the vortices by plotting iso-surfaces of a value of λ_2.

6.2.2   Feedback Mechanism

The second flow mechanism which is anticipated is the feedback mechanism. The feedback mechanism is expected to consists of acoustic waves, which require a rather special technique for visualisation. Greschner et al. (2010) shows that acoustic waves can be visualised by showing the time derivative of pressure.

The pressure time derivative is not defined as a standard output of OpenFOAM. An extension needs to be used in order to specify this output. This extension has been formulated by Gschaider (2017), a library called Swiss Army Knive For Foam.

Using the time derivative of pressure, it is made evident to distinguish between the hydrodynamic perturbations, which transport with convection velocity and the acoustic pressure perturbation, which travel with the acoustic velocity corrected by convection velocity (Greschner et al., 2010).

The pressure time derivative will be visualised by contours on a slice in Paraview. This slice will be located on the centreline of the door opening.

6.2.3   Experiments

Due to the limited experimental resources available, information about the flow mechanisms can only be extracted from pressure probes. For identification of the main flow mechanism which is contributing to the oscillation in the experiments, a post-processing tool has been scripted.

This post-processing tool using the exact same methodology as described in Section 6.1. However it uses the raw data from the Scanivalve DSA3217 pressure scanner for different tunnel settings and therefore different velocities. Using the different spectra found at different velocities, a heat map of the dominant frequencies, over a range of velocities will be constructed. Comparing the relation between velocity and dominant frequency with the Rossiter modes found in using Equation (2.2), this tool will be able to confirm the flow mechanism which is responsible for the pressure oscillation.

6.3   Grid Dependence

In order asses the reliability the numerical solution, a grid dependence study is performed. Roy (2005) describes tests in order to verify the order of accuracy of the numerical solution, which verifies the correct implementation of the the mathematical side of the numerical simulations. For the current study, a method which relies on the observed order of convergence, can confirm the correct implementation of the numerical schemes.

Slater (2006) describes such a method using numerical solutions only. At least three levels of grid refinement are necessary for this method. The solution on the finest grid serves as the reference solution to calculate the relative error. The relative error, will as function of a variable which is proportional to grid cell size, represent the relation found in Equation (6.3). In this relation, the logarithm of the error ($error$) is equal to the observed order of convergence p_{conv}, multiplied with the logarithm of cell size variable (h_{conv}) added with a constant term.

$$log_{10}(error) = p_{conv} \times log_{10}(h_{conv}) + log_{10}(C) \tag{6.3}$$

Using the relative error between the two coarse grids and the fine grid will provide enough information. The error will be calculated using the SPL of the cavity buffeting peak, extracted from the pressure probes, using the methodology discussed in Section 6.1. As an indication of cell size, dealing with hybrid grids, it is most convenient to chose h to be defined as Equation (6.4).

$$h_{conv} = \sqrt[3]{\frac{1}{Number of cells}} \tag{6.4}$$

Using the information probed at two locations in the cavity will be used to show the order of convergence by fitting a linear relation on the logarithmic values.

Part III

Results

Chapter 7

Current Situation

Analysis of the current situation has been conducted trough CFD simulation and experimental measurements using the methodology defined in Chapters 4 and 5.

This chapter starts with the discussion of the results found in simulation and experiment, after which a comparison is made between both experiment and simulation for validation purposes.

7.1 Simulation

In this section, first quantitative results from pressure probes will be presented and discussed, after which the flow mechanisms, extracted from simulation results are extracted and visualised.

7.1.1 Pressures Probes

During simulation, pressure results have been probed at two specific locations in the waiting room. The pressure signals have been processed using the methodology in Chapter 6 and presented in Figures 7.1 and 7.2.

Examining the results from both probes, the behaviour can be found to be very similar. Quantitative data has been extracted from the spectrum, shown in Figure 7.1(b) and presented in Table 7.1. It is evident that the spectrum is dominated by an oscillation which is associated to a frequency of 15 Hz. This low frequency component is most likely caused by a single vortex mode above or in the cavity opening.

Furthermore, an even lower peak has been found at 3.2 Hz. This frequency has no physical origin from the flow trough the sky-dive tunnel geometry. Due to boundary conditions, in which

a constant velocity is enforced on the inlet of the domain, blockage effects by the periodic wake, propagating from the top-side of the cavity mouth towards the expansion of the tunnel, induces the pressure difference over the domain to periodically increase. These effects are not expected to be present in the experimental results, as the fans of the tunnel in fact show different physical behaviour than the boundary conditions applied in this simulations. More details regarding this oscillation have been presented in Appendix C.

Next to this, three harmonics of the first Rossiter mode are clearly visible as indicated in Figures 7.1(b) and 7.2(b) and table 7.1. Furthermore a more vaguely defined mode can be observed around 54 Hz. This mode can be correlated to a theoretical estimate of the third Rossiter mode, which originates from the presence of three shed vortices above the cavity opening. However, as this mode smears over multiple frequencies surrounding 54 Hz, it is plausible that the three vortices are not always present at the same time.

Table 7.1: Frequency content for probe 1 (P1) and probe 2 (P2)

P1 f [Hz]	P1 SPL [dB]	P2 f [Hz]	P2 SPL [dB]	Mode
3.2	133.2	3.2	132.7	BC induced
15.0	148.7	15.0	149.6	First Rossiter mode
29.9	118.4	29.6	121.7	First Rossiter mode harmonic 1
44.9	111.1	44.9	106.4	First Rossiter mode harmonic 2
54.6	110.2	53.7	113.6	Rossiter mode 3
59.8	114.4	59.8	116.5	First Rossiter mode harmonic 3

When further examining Figures 7.1(b) and 7.2(b), multiple extra peaks above the last harmonic are visible. However, no related flow mechanism in the scope of the theory explained in Chapter 2 can be found to be responsible for this peaks.
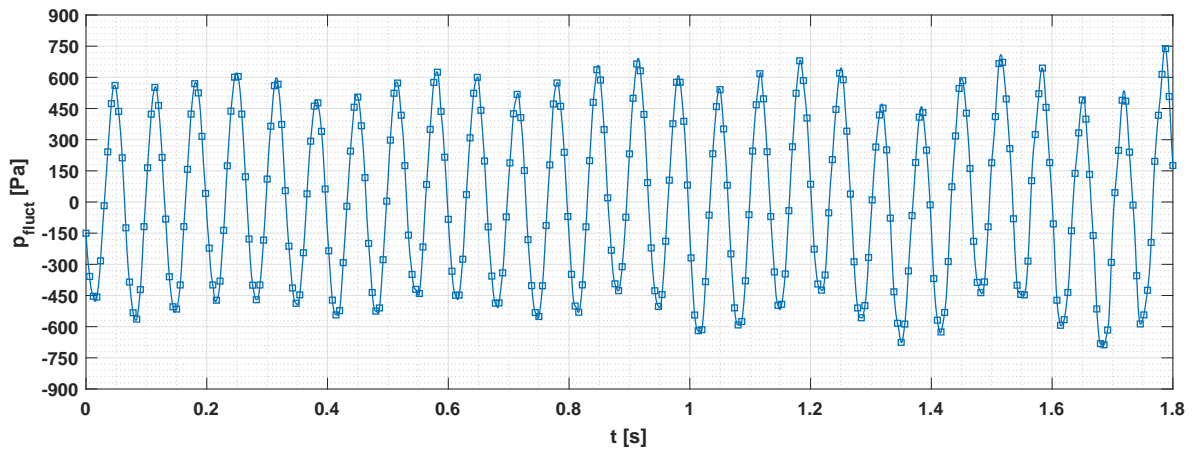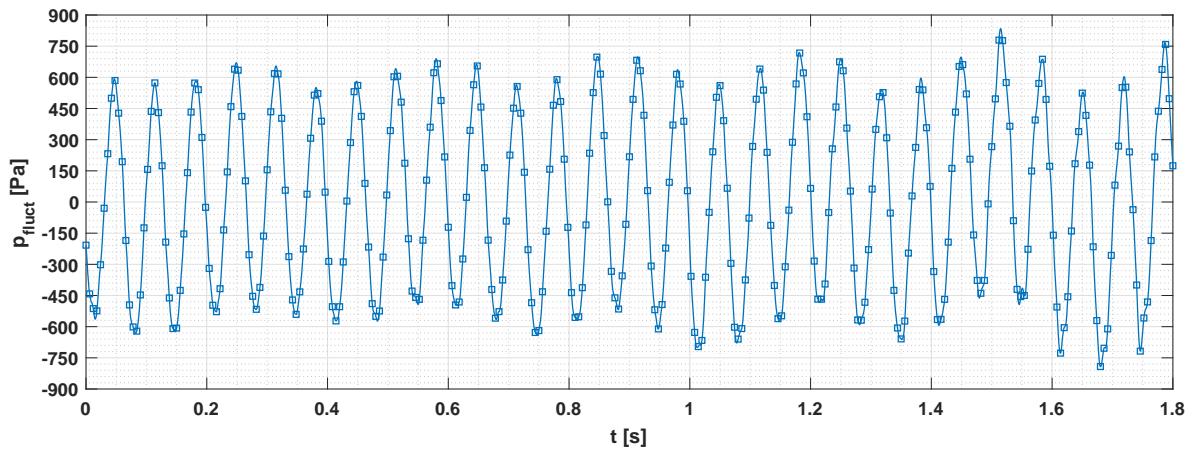
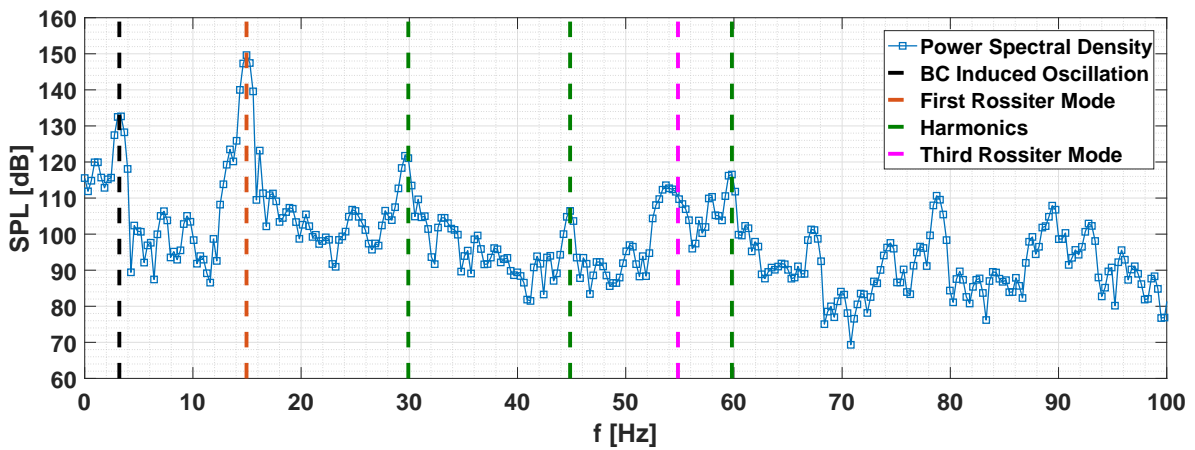(a) Time series pressure fluctuation probe 1
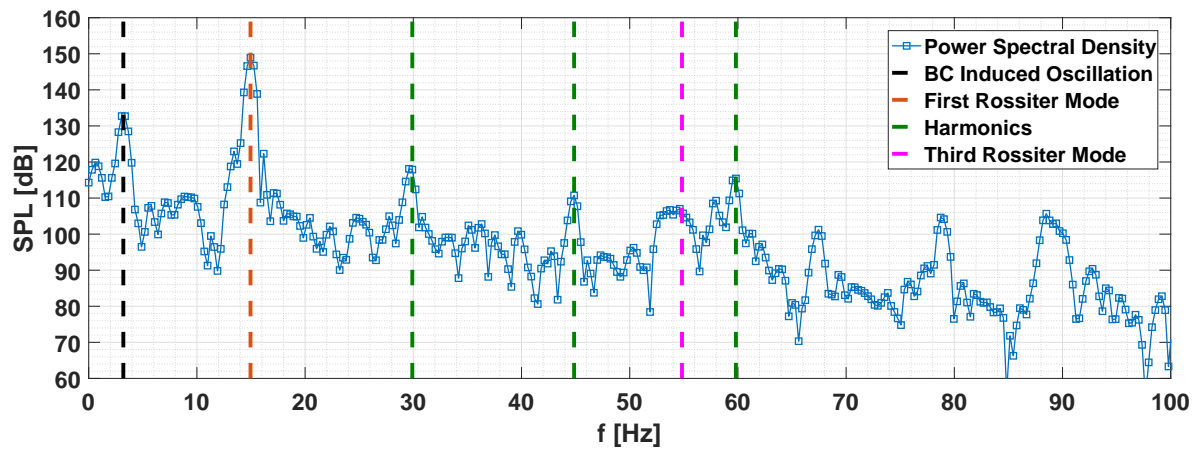
(b) Sound pressure level spectrum probe 1

Figure 7.1: Probe 1 time series and spectral results

(a) Time series pressure fluctuation probe 2

(b) Sound pressure level spectrum probe 2

**Figure 7.2:** Probe 2 time series and spectral results

7.1.2 Grid Convergence

Considered as an important check for numerical studies, a grid dependence study has been carried out. Using the method described in Section 6.3, grid convergence of the sound pressure level, associated to the main buffeting frequency has been calculated.

The sound pressure level of the cavity buffeting peak has been extracted from the spectral results for the three different mesh refinements. The resulting values have been presented in Table 7.2 and are converted to relative error and h_{conv} using the methodology described in Section 6.3.

Table 7.2: Peak SPL for both probes at different grid refinements

Grid	Number of Cells	SPL probe 1	SPL probe 2
Fine	3645986	148.03	148.73
Medium	2441930	148.92	149.64
Coarse	2374734	148.93	149.66

(a) Convergence Probe 1

(b) Convergence Probe 2
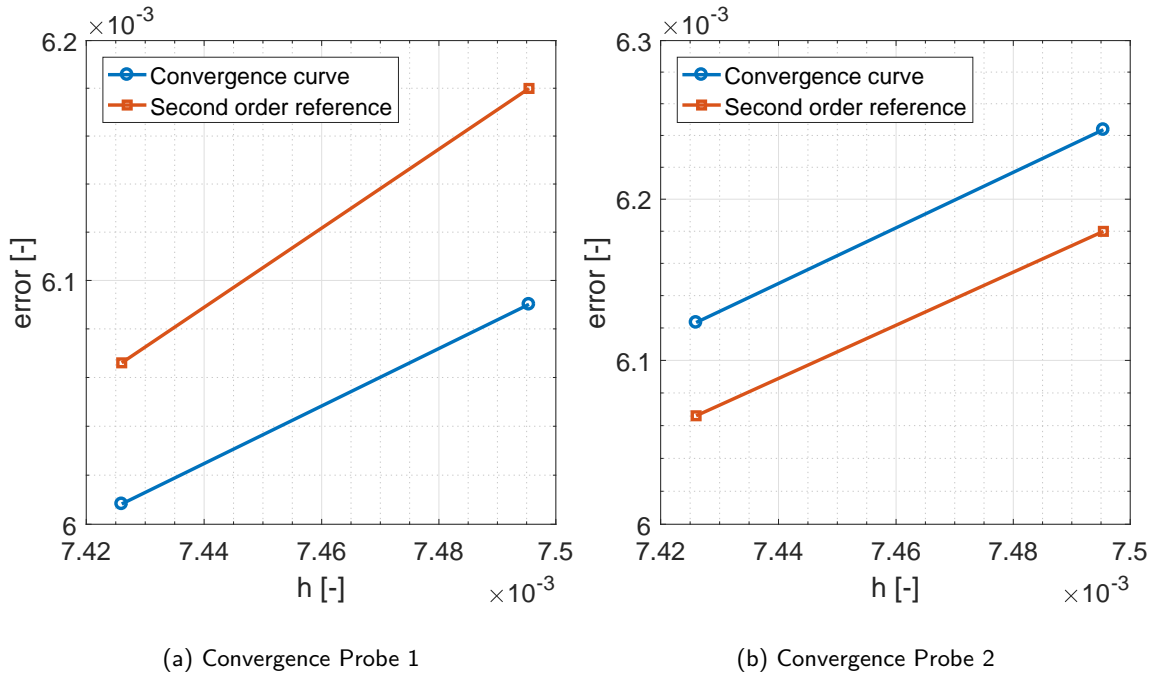
Figure 7.3: Error grid convergence and comparison with second order reference

Fitting linear curves (similar to Equation (6.3)) on the logarithmic values of both the probes, the rate of convergence for spatial discretisation can be found to be respectively 1.45 and 2.09 for probe1 and probe2.

Both show a discrepancy with the theoretical value of 2 associated with the numerical schemes. These discrepancies potentially originate from the use of unstructured grids. The refinement factor can not be ensured for the complete volume as a similar surface mesh has been used, which makes the scale used for h_{conv} (see Equations (6.3) and (6.4)) bad defined due to local refinements.

Despite that, the discrepancies are not too big and the author remains confident that the chosen numerical schemes are correctly implemented. Furthermore, the differences between the peak sound pressure levels found for the fine and medium mesh, show an error of only 0.6%. Therefore, cell-sizes defined for the medium mesh will be used for the retrofit designs.

7.1.3 Flow Mechanisms

In order to address the origin of discrete frequencies in the pressure oscillation, it is critical to visualise the flow mechanisms which are prone to cause the oscillation.
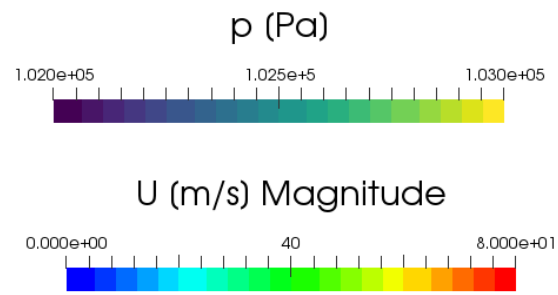
Vortex Shedding

In order to identify the dominant flow mechanisms, it is convenient to track the flow properties at different time steps in one period of the cavity buffeting oscillation.

Using the λ_2-criterion , iso-surfaces above the cavity opening have been constructed as described in the methodology of Section 6.2.1. Together with slices of pressure contours, the iso-surfaces are presented in Figure 7.4, the vortex shedding mechanism and the relevant pressure oscillation is shown.

Analysing the results, it is evident that multiple vortices are shed in a rather narrow time-frame. In Figure 7.4 it is shown that during one period of oscillation, a three vortices are constantly present (or developing) above and in the cavity opening.

Following the two shed vortices, VT1 and VT2, developing in Figure 7.4(e), the two merge into a lager scale vortex (LSVT1) in Figure 7.4(f). The bigger vortex propagates into the cavity as seen in Figures 7.4(g) and 7.4(h) and finally impinges with the trailing edge shape. Part of LSVT1 slips past the trailing edge (ILSVT1) shape towards the ceiling in Figure 7.4(i) and part propagate downwards into the cavity (ILSVT2). During the formation of LSVT1, two extra vortices (VT3 and VT4) develop in Figures 7.4(f) to 7.4(i) and propagate over the opening of the cavity.

The development of the larger scale vortex and the impingement that follows, occurs in one time per period of the dominant oscillation frequency. Combining the observation of the behaviour of the vortices, with the pressure contours presented Figure 7.4, the different stages during vortex propagation can be linked to the pressure behaviour. During the development of the larger scale vortex (Figures 7.4(d) to 7.4(h)) the pressure rises, which is caused by the entrainment of air into the cavity. After impingement/interaction with the trailing edge shape (Figure 7.4(i)), the pressure decreases again. These observations yield that a single large scale vortex is responsible for the dominant oscillation, which therefore can be linked to the first Rossiter mode.

(a) Legend
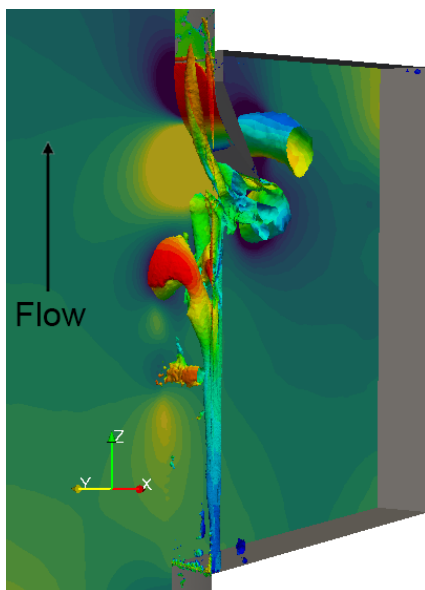
(b) t=0.00s
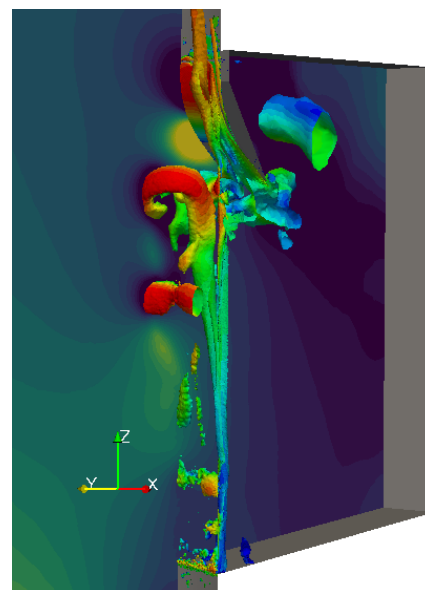
(c) t=0.01s
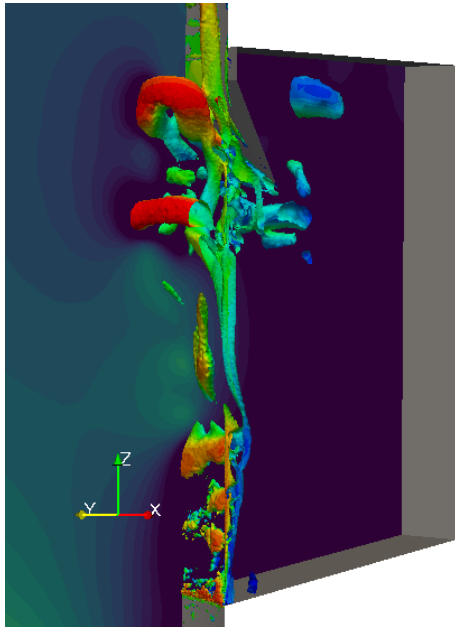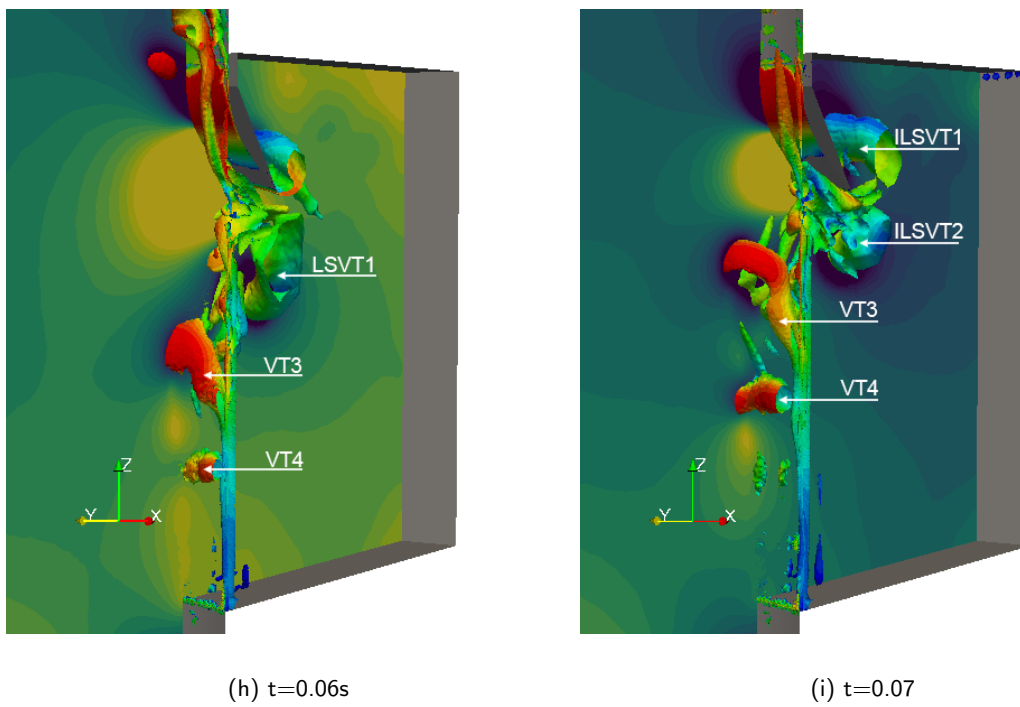
(d) t=0.02s
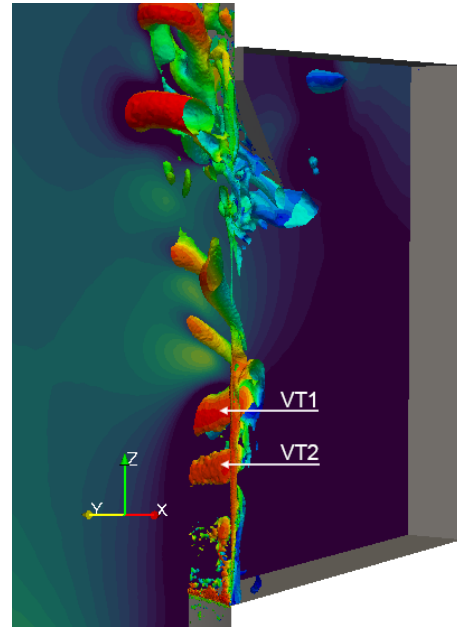
(e) t=0.03s

(f) t=0.04s

(g) t=0.05s

(h) t=0.06s   (i) t=0.07
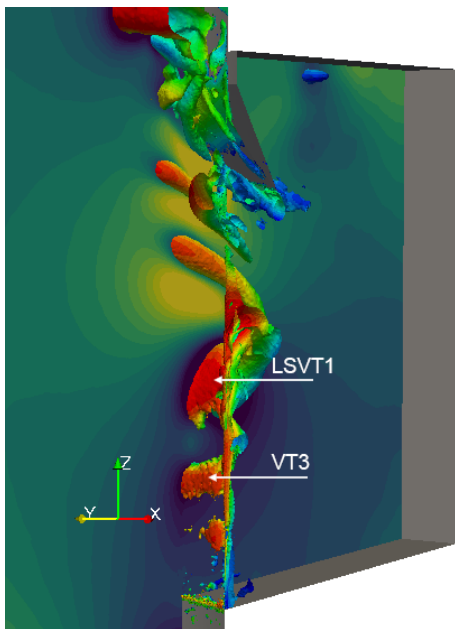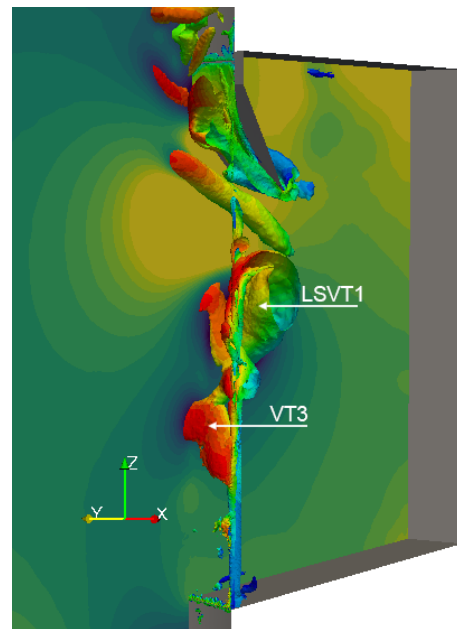
Figure 7.4: Vortex visualisation using λ_2-criterion iso-surfaces at $\lambda_2 = -10000$

Feedback Mechanism

The feedback mechanism is more difficult to visualise than the vortex shedding. Using the methodology described in Section 6.2.3, the time derivative of pressure has been visualised in Figure 7.5.

It is evident that the strongest pressure fluctuations originate from the vortices in the shear-layer. However these propagate with local convection velocity and are therefore not part of the acoustic feedback mechanism. Different, must faster propagating disturbances can be found in the cavity itself. In order to track one of these disturbances, a red line has been drawn in Figures 7.5(c) and 7.5(d). Although difficult to visualise and to track due to the large wavelength of these acoustic disturbances, the visualisation confirms the existence of the feedback mechanism in the cavity.
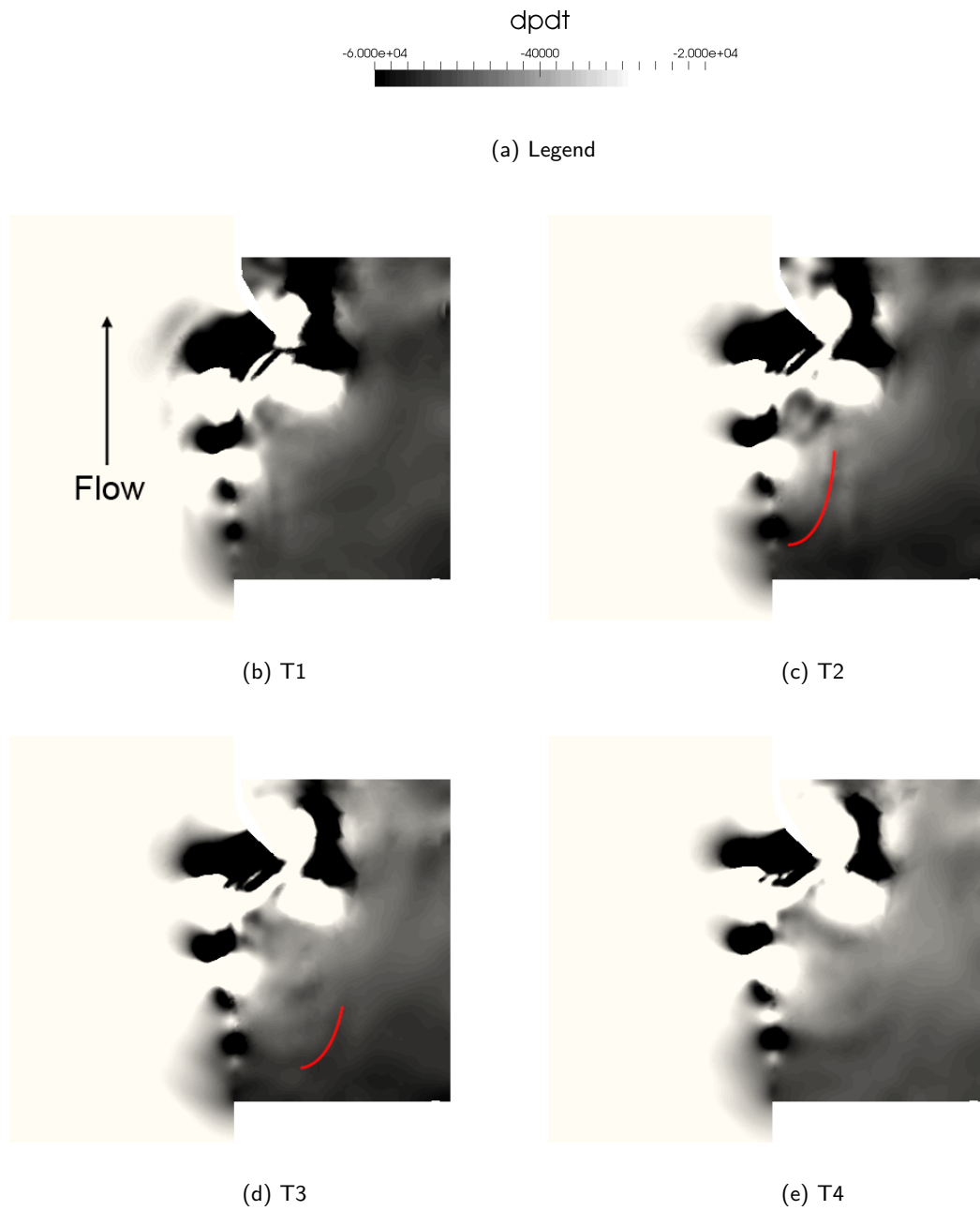
(a) Legend

(b) T1   (c) T2

(d) T3   (e) T4

Figure 7.5: Slices showing $\frac{dp}{dt}$ for visualisation of feedback mechanism

7.2   Experiment

In order to confirm the capabilities of the CFD set-up to predict cavity buffeting noise, experimental measurements have been conducted for the current situation. In this section, the spectral results following from these measurements will be discussed, after which the flow mechanisms will be identified.

7.2.1   Spectral Result

After simulation a strong fluctuation in pressure is expected for the pressure probes in experiment. Using the same methodology as for the probe locations in the simulation, the spectrum for the case of an average velocity of 68.4 ms^{-1} has been calculated and presented in Figure 7.6. When examining the spectrum, only one distinct peak can be identified, which can be related to cavity buffeting noise. At a frequency of 16.6 Hz, a peak of 131.4 dB is observed.

Firs observations show that the First Rossiter mode is dominating the spectrum. The frequency of the first harmonic, second Rossiter mode and third Rossiter mode have been estimated and shown in Figure 7.6. However, no distinct peaks can be identified near these frequencies.

Hypothetically, these frequencies could be of a strength equal of the measurement noise.
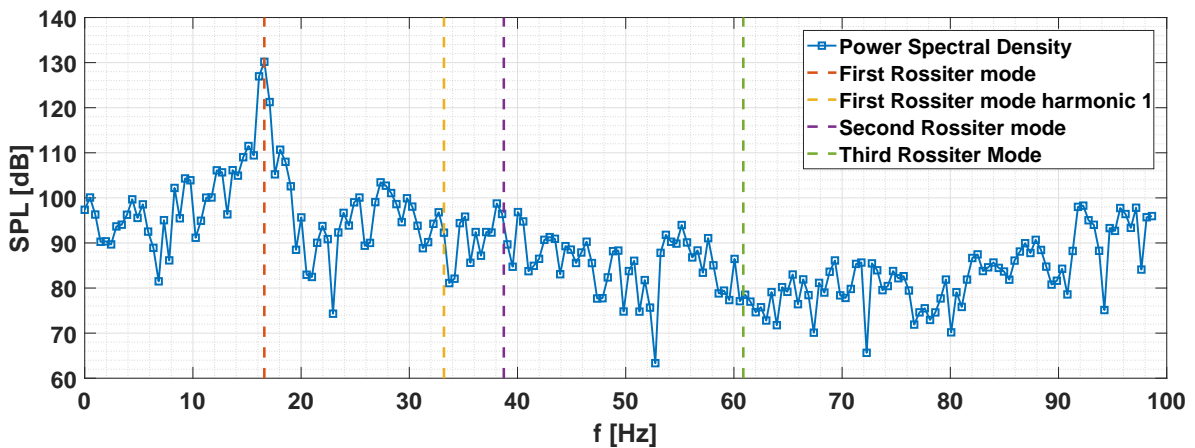

Figure 7.6: Sound pressure level spectrum experimental measurement of current situation at 68.4 ms^{-1}

7.2.2 Flow Mechanism

Applying the experimental set-up, described in Chapter 5, together with the processing tool described in Section 6.2.3, a heatmap consisting of the sound pressure levels over the 0 to 100 Hz spectrum has been created and presented in Figure 7.7.

An theoretical, semi-empirical estimate of the Rossiter frequency has been calculated using Equation (2.2) and the input from Table 7.3.

Table 7.3: Rossiter mode calculation input

Symbol	Description	Value	Units
L	Cavity length scale	2.3	m
n	Number of vortices	1	-

Varying over the same velocity range as the experiments, the Rossiter modes have been determined.

Next to the Rossiter modes, the Helmholtz frequency can be estimated using Equation (2.3) and input from Table 7.4. The Helmholtz frequency has been estimated to be 12.0 Hz.

Table 7.4: Helmholtz frequency calculation input

Symbol	Description	Value	Units
a_0	Speed of sound	343	ms^{-1}
A	Area of cavity opening	1.54	m^2
V_c	Cavity volume	29.2	m^3
h_n	Cavity neck length	0.07	m

In order to identify the flow mechanism, responsible for cavity buffeting noise, theoretical estimates of the first Rossiter mode and Helmholtz frequency have been plotted in the heatmap presented in Figure 7.7.

It can be observed that the estimate of the trend of the first Rossiter mode correlates with the dominant frequency in the heat map. Exact values do not match perfectly, which most probable can be related to the vague definition of the cavity length due to the shape of the trailing edge of the cavity (see Section 4.7).

Furthermore, the largest sound pressure levels are not found at the highest inflow velocities. The strongest fluctuation is found for 45.6 ms^{-1}. At this velocity the vortex shedding frequency is close to the theoretical estimate of the Helmholtz frequency of 12.0 Hz.
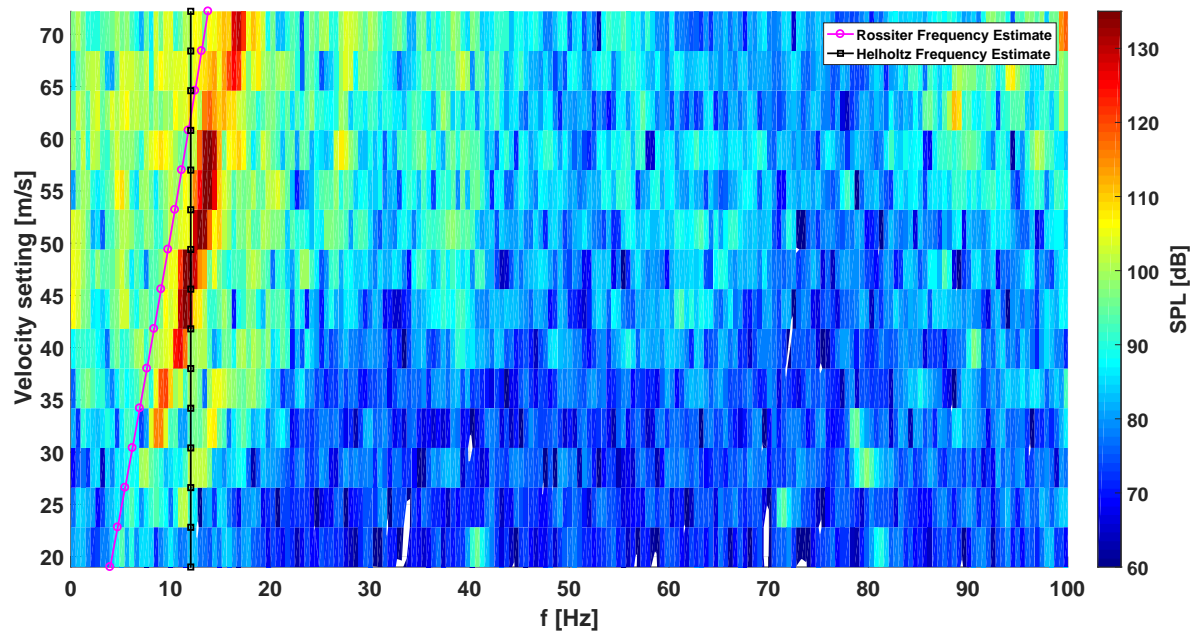
Figure 7.7: Heatmap of sound pressure levels at different tunnel velocities for 0-100 Hz

7.3   Validation

The spectral results of both the CFD simulation and experiment have been presented in Figure 7.8. Evidently discrepancies appear.

The first discrepancy is found for the boundary condition induced oscillation in the simulation results. Due to the behaviour of the fans, this oscillation does not exist in the spectrum extracted from experiment data.

The dominant sound pressure peak shows a large difference between simulation and CFD. Quantitatively, the difference is found to be 17.5 dB which is resembles an error of 11.8%. It has been found in Chapter 2 that the strength of the cavity buffeting oscillation is dependent on the thickness of the boundary layer. Due to domain truncation and imperfections of the building quality, the boundary layer is likely to be much thicker in experiment than in CFD, which increases the thickness of the shear-layer, reducing the strength of the oscillation. Furthermore, perforated panels have been installed between the waiting room and the sky-dive section, which were not taken into account in the simulation (see Appendix D).

The frequency of the dominant peak shows 1.6 Hz difference between simulation and experiment which resembles an error of 10.7 %. The difference in frequency is most likely caused by a mismatch in inflow velocity between simulation and experiment.
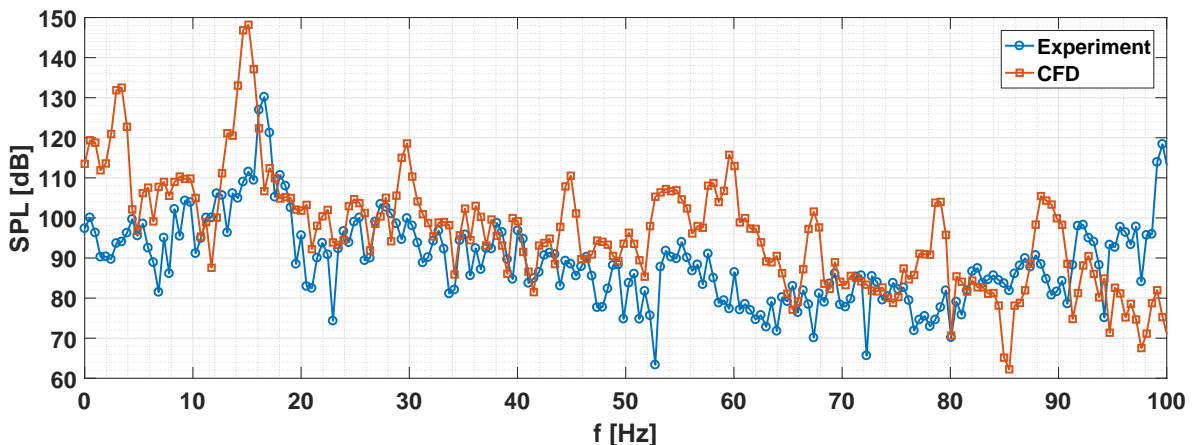

Figure 7.8: Comparison sound pressure levels CFD and experiment

Where the exact values, associated to the current problem, tend to show a rather large variation between experiment and simulation, a qualitative comparison can show similar flow mechanisms to be present.

Using the results involving the flow mechanisms found in Sections 7.1 and 7.2, it is evident that both the experiment and simulation contain very similar flow mechanisms. Despite the mismatch in oscillation strength, the frequencies show rather good agreement in absolute sense. Next to this, both the simulation and experiment have been linked to the first Rossiter mode, which confirms

that the simulation set-up is able to predict the onset of cavity buffeting noise.

Further investigation has to show the correct prediction of a reduction for different geometries. This fill be further discussed in Section 8.3

Chapter 8

Retrofit Designs

Using the same methodology as for the current situation, various retrofit designs have been compared to the current situation. Next to this, an experimental evaluation study has been carried out on the best performing retrofit design. In this chapter, first the simulation results will be discussed, after which the experimental evaluation is addressed. Following the experimental results, further validation of the CFD set-up is provided.

8.1 Simulation Results

For the purpose of finding cavity buffeting noise reductions, CFD has been been applied using the methodology in Chapter 4 employing the proposed retrofit designs in Section 4.7.2.

In this section, the effect of the retrofit designs, combined with the existing geometry, will be discussed. First the spectral quantitative results will be discussed by comparison with the current situation. Second the suppressing flow mechanisms/features will be identified using the results of the most effective solution.

### 8.1.1 Pressure Probe Results

The sound pressure level spectra have been presented in Figure 8.1 and table 8.1. First of all it can be observed that the trailing edge extension and wing reduced the the cavity buffeting sound pressure level by respectively 6.0 dB (4.0%) and 2.5 dB (1.7%). Furthermore it can be observed that both the wall-normal Cylinder and the span-wise cylinder do not perform according to expectation. Both are not capable of reducing the strength of the oscillation and even increases of respectively 1.5 dB (1.0%) and 3.6 dB (2.4%) in sound pressure levels are observed.

Table 8.1: Peak sound pressure levels for retrofit solutions (TEE = trailing edge extension, SWC = span wise cylinder, WNC = wall normal cylinder)
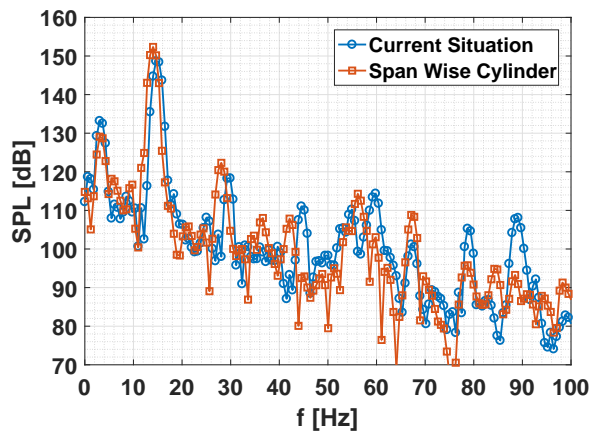
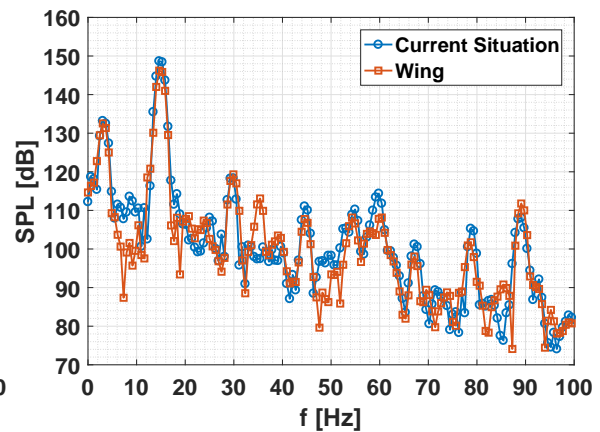| Geometry	Current	TEE	SWC	WNC	Wing
SPL [dB]	148.7	142.7	152.3	150.2	146.2
ΔSPL [dB]	-	-6	3.6	1.5	-2.5
ΔSPL [%]	-	-4.0%	2.4%	1.0%	-1.7%
f [Hz]	14.7	15.3	14	14.7	14.7
Δf [Hz]	-	0.6	0.7	0	0
Δf [%]	-	4.1%	4.8%	0.0%	0.0%
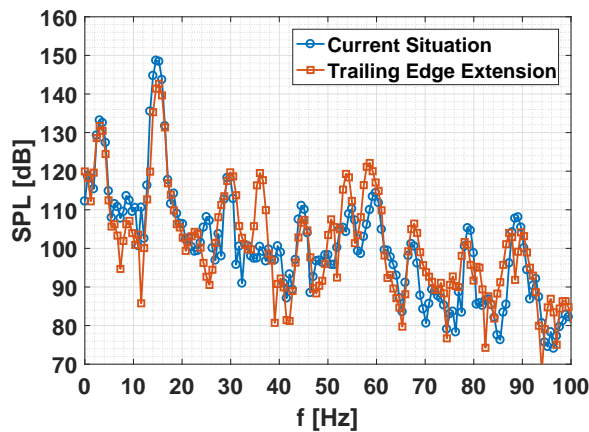
(a) Trailing edge extension
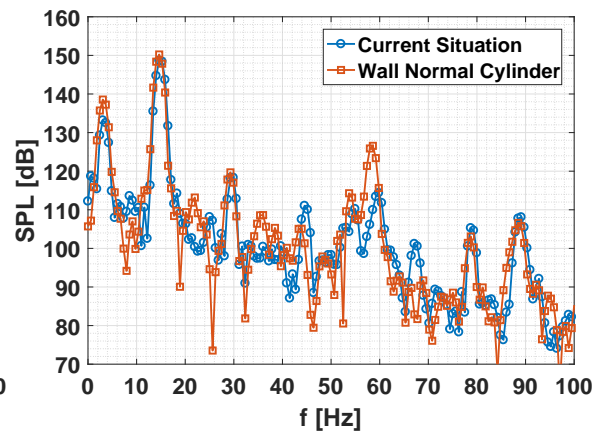
(b) Wall normal cylinder

(c) Span wise cylinder

(d) Wing

Figure 8.1: Sound pressure level spectra for the four different retrofit designs and comparison with the current situation

8.1.2   Influence on velocity

Another important aspect of the novel solutions is the velocity distribution downstream of the cavity opening. When a large wake is created to reduce cavity buffeting noise, the wake is noticeable downstream of the cavity opening, possibly disabling sky-dive simulation abilities. For reference purposes, the wake above the cavity for the current situation has been visualised by means of velocity contours in Figure 8.2. The area of the cross-sections, which is exposed to velocities smaller than 70 ms^{-1} has been calculated and tabulated in Table 8.2.

Table 8.2: Wake area (velocity smaller than 70 ms^{-1}) and change relative to current situation (TEE = trailing edge extension, SWC = span wise cylinder, WNC = wall normal cylinder)

Case	Wake area [m^2]	Relative change
Current	0.97	-
TEE	0.92	-5.2%
WNC	1.09	12.4%
SWC	1.21	24.7%
Wing	0.99	2.1%

On the right side of the tunnel, an area of reduced velocity (wake) is visible. For this situation, it has been observed that sky-dive simulation is possible, without difficulties. Evidently, when a cavity buffeting reducing solution causes the wake to grow, negative influence on the abilities of sky-diving above the cavity mouth will be observed.
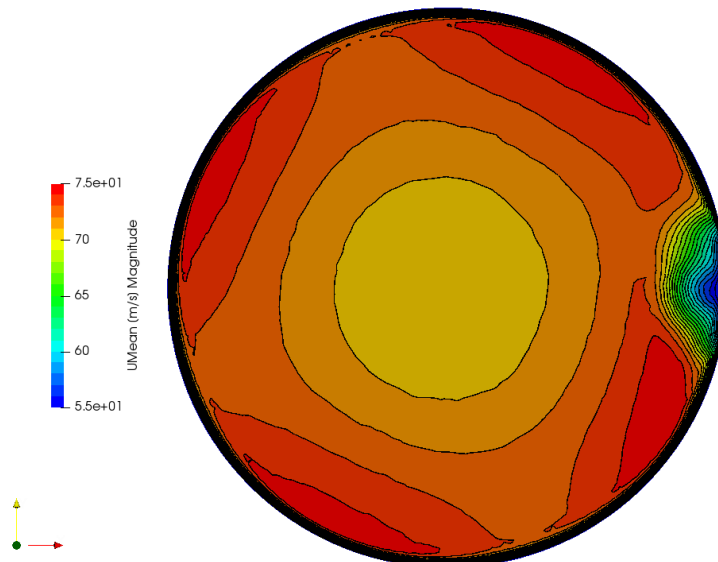

Figure 8.2: Velocity contours downstream of cavity, z-slice, current situation

Trailing edge extension

The velocity contours downstream of the cavity opening, for the case of the application of the trailing edge shape extension has been presented in Figure 8.3.

Similar to the current situation, shown in Figure 8.2, a wake can be recognised at the right hand side of the tunnel. Compared to the current situation, the wake has been reduced in size by 5.1%, which is a positive effect for the performance of the tunnel.
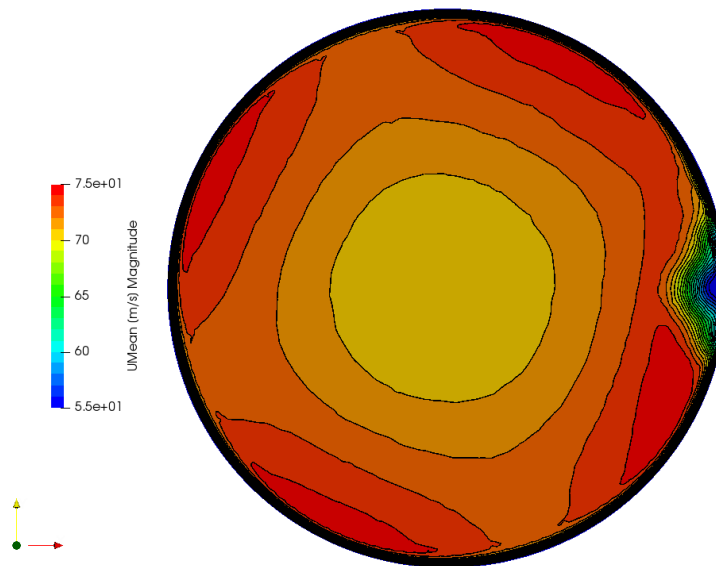

Figure 8.3: Velocity contours downstream of cavity, z-slice, trailing edge extension

Wall-normal Cylinder

The velocity contours downstream of the cavity opening, for the case of the application of the wall normal cylinder has been presented in Figure 8.4.

Compared to the current situation, the wake has been increased in size by 12.4%, which evidently is a negative effect on the tunnel performance.
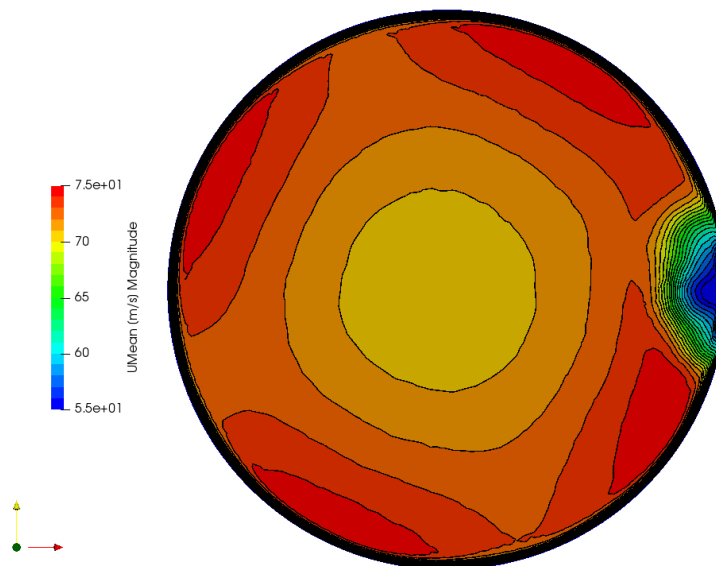

Figure 8.4: Velocity contours downstream of cavity, z-slice, wall normal cylinder

Span-wise Cylinder

The velocity contours downstream of the cavity opening, for the case of the application of the span wise cylinder has been presented in Figure 8.5.

Compared to the current situation, the wake has been increased in size by 24.7%, which evidently is a negative effect on the tunnel performance. Next to this, the size of the wake, compared to the wall normal cylinder, has been increased further.
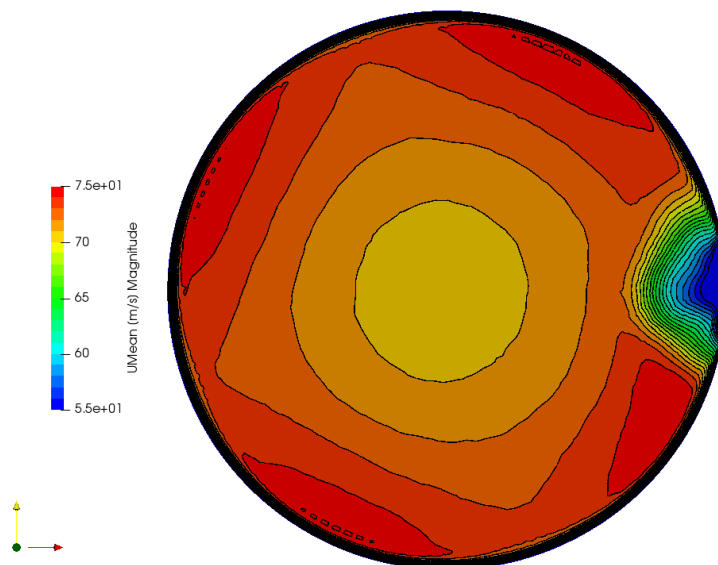

Figure 8.5: Velocity contours downstream of cavity, z-slice, span-wise cylinder

Wing

The velocity contours downstream of the cavity opening, for the case of the application of the wing has been presented in Figure 8.3.

Compared to the current situation, the wake remains very similar and only slightly grows by 2.1%.
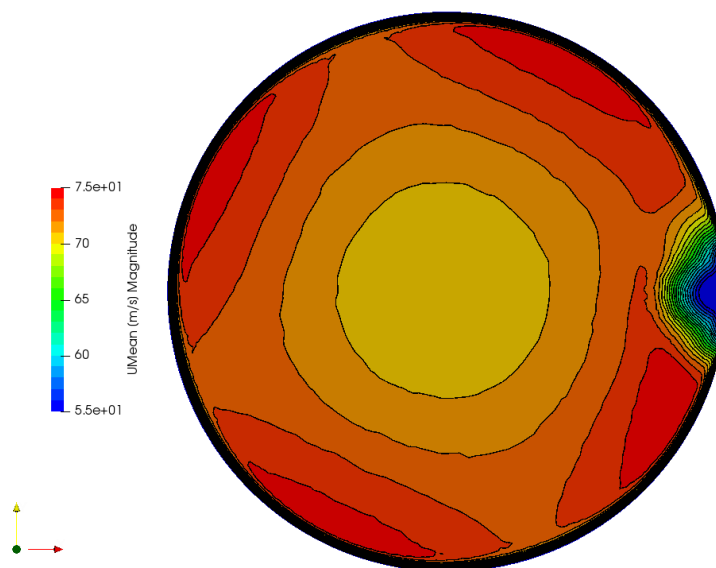

Figure 8.6: Velocity contours downstream of cavity, z-slice, wing

8.1.3   Flow Mechanisms

In analysis of the current situation it has been found that vortex shedding is responsible for the cavity buffeting noise. In this section, the vortex shedding mechanism of application of the trailing edge extension and span-wise cylinder will be analysed and compared to the current situation. The results regarding the wall-normal cylinder and the wing have been added in Appendix E.
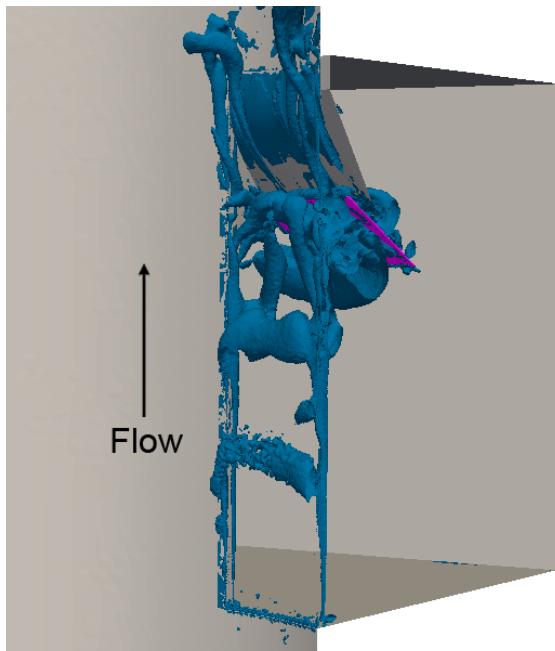
Trailing edge extension

As determined before, the shed vortices are responsible for the pressure oscillation in the cavity. Especially the interaction of the larger scale vortex with the trailing edge of the cavity has large influence on the pressure behaviour.

Investigating the behaviour of vortices for the case in which an extension of the trailing edge shape has been applied, it can be observed that the initial behaviour of vortex shedding and development of the large scale vortex remains very similar to what has been observed in Section 7.1.3.

Although the flow mechanisms are very similar, the two initially shed vortices VT1 and VT2 merge further downstream (shown in Figures 8.7(d) to 8.7(g)). Shortly after the two initially shed vortices are merged, the larger scale vortex (LSVT1) impinges on the trailing edge extension (Figure 8.7(h)). As a result of the impingement, part of LSVT1 propagates down the trailing edge extension as ILSVT2 and part of the vortex propagates out of the cavity as ILSVT1.
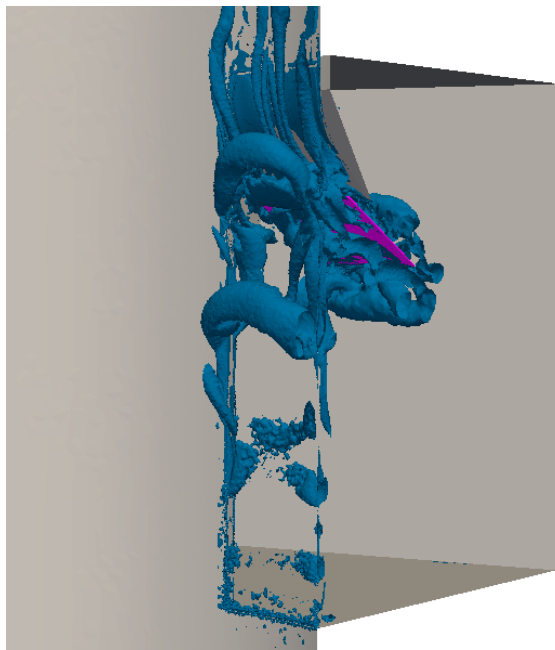
Compared to the current situation, the impingement of the large scale vortex has changed, as it is not able to slip past the trailing edge shape due to the extension. The change in impingement is very likely to reduce the strength of the vortex and therefore the pressure oscillation in the cavity.
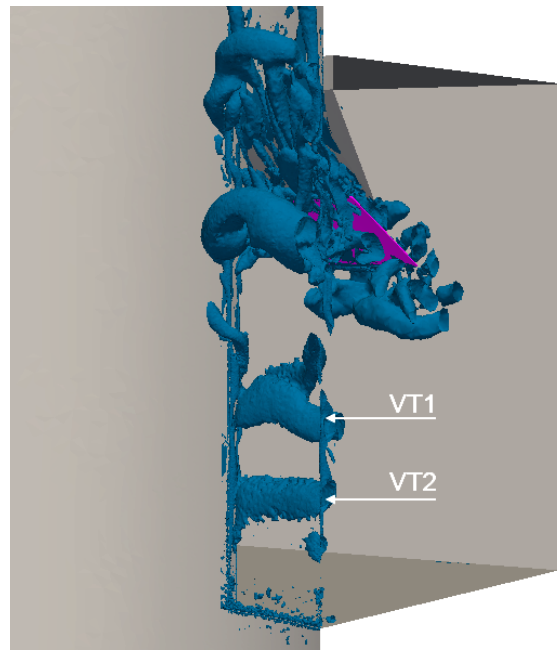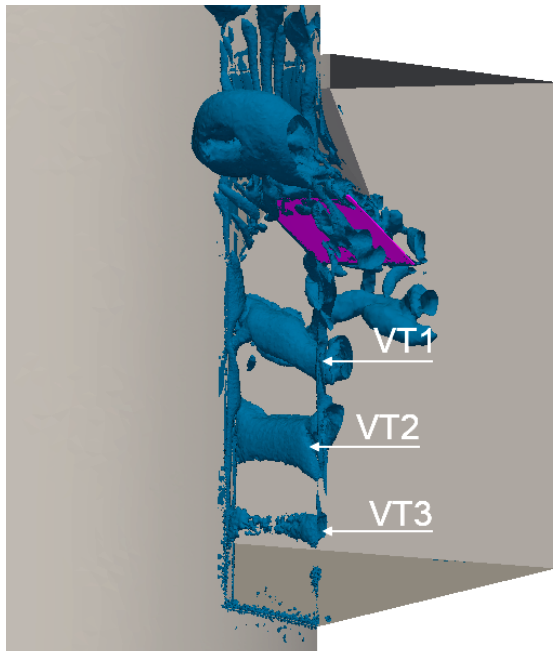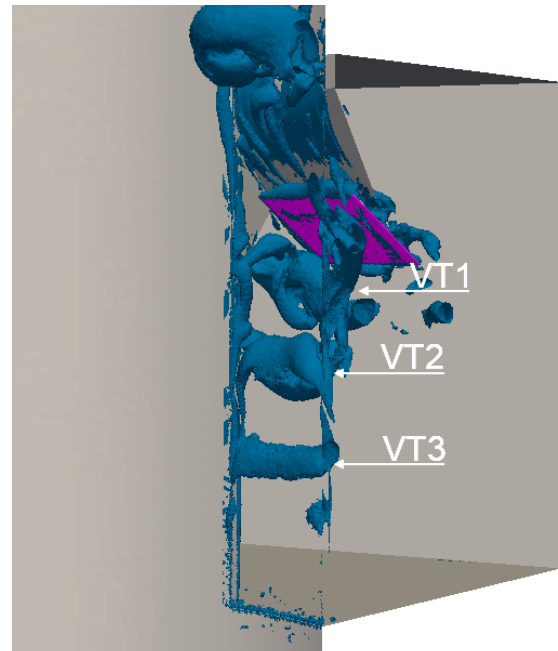
(a) t=0.00
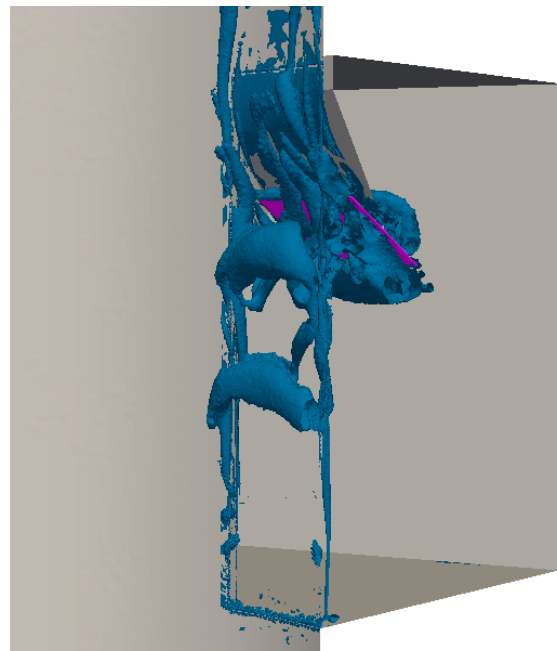
(b) t=0.01

(c) t=0.02

(d) t=0.04

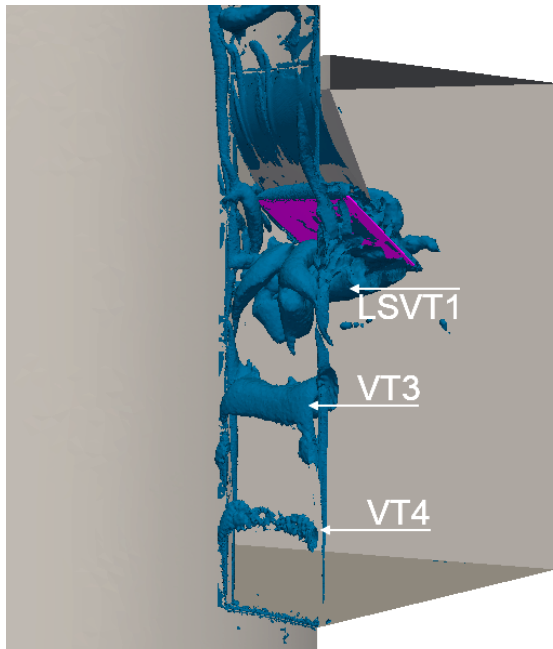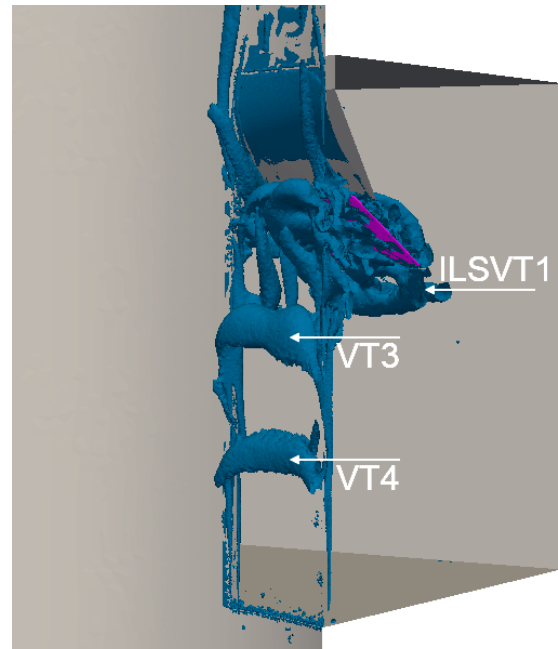(e) t=0.05

(f) t=0.06
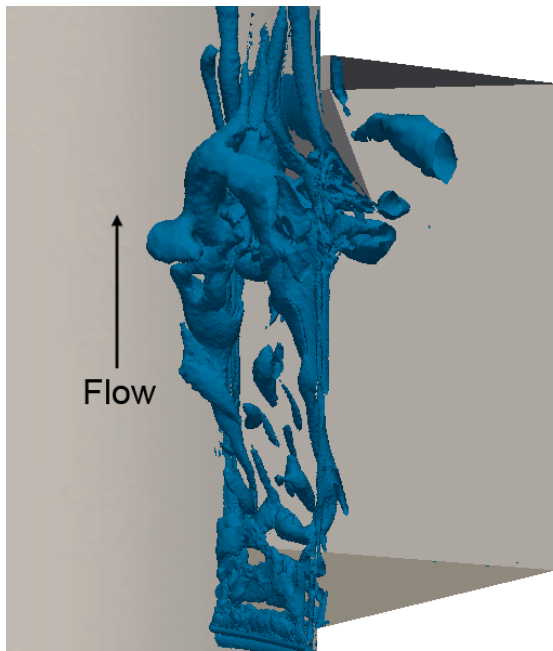

(g) t=0.07

(h) t=0.08

Figure 8.7: Vortex visualisation trailing edge extension using λ_2-criterion iso-surfaces at $\lambda_2 = -10000$

Span-wise cylinder

The span wise cylinder increases the oscillation strength. The associated vortex visualisation for the span wise cylinder has been presented in Figure 8.8. Due to vortex scales, introduced by the cylinder, it is more difficult to identify the vortex mechanism which is responsible for cavity buffeting noise.

However, careful observations reveal interaction between the shed-vortices from the cavity edge and the shed-vortices originating from the cylinder. In Figure 8.8(b) a vortex shed from the cylinder (CVT1) and a vortex shed from the cavity leading edge (VT1) are shown. A small step in time later, Figure 8.8(c) these vortices are merged into a larger scale vortex (LSVT1), which propagates downstream in Figure 8.8(d) and Figure 8.8(e). Finally, the larger scale vortex impinges on the trailing edge of the cavity Figure 8.8(f).

Compared to the current situation, the larger scale vortex travels further inward into the cavity (Figure 8.8(f)). Furthermore the larger scale vortex starts further upstream with developing compared to the current situation, opposite to the downstream development in the trailing edge extension.

(a) t=0.00s
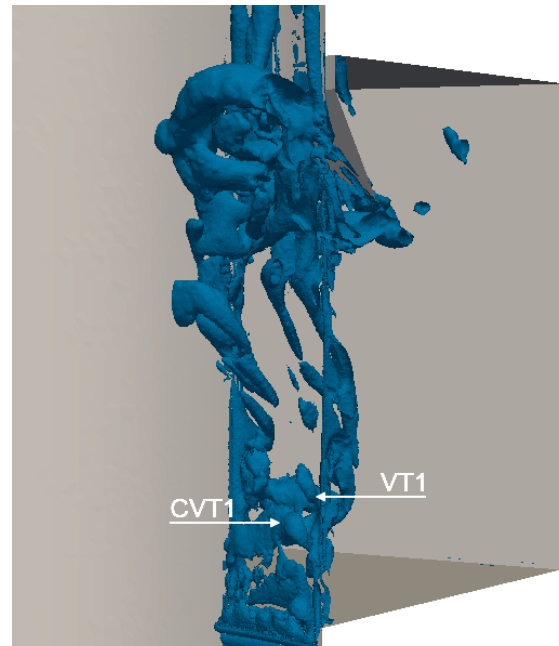
(b) t=0.01s
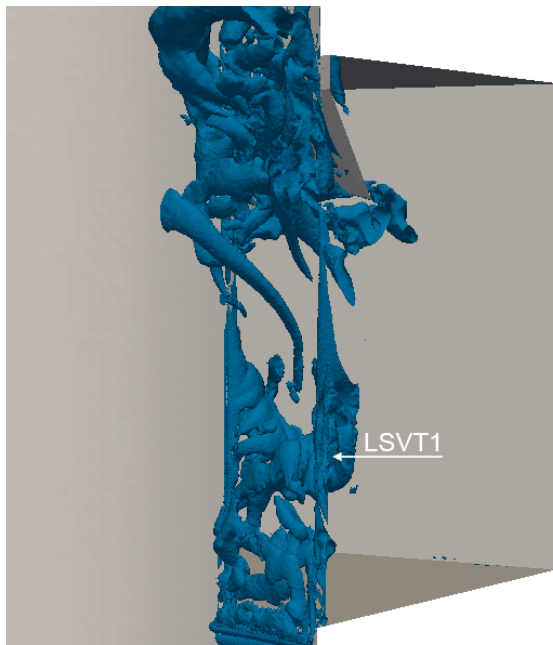
(c) t=0.02s
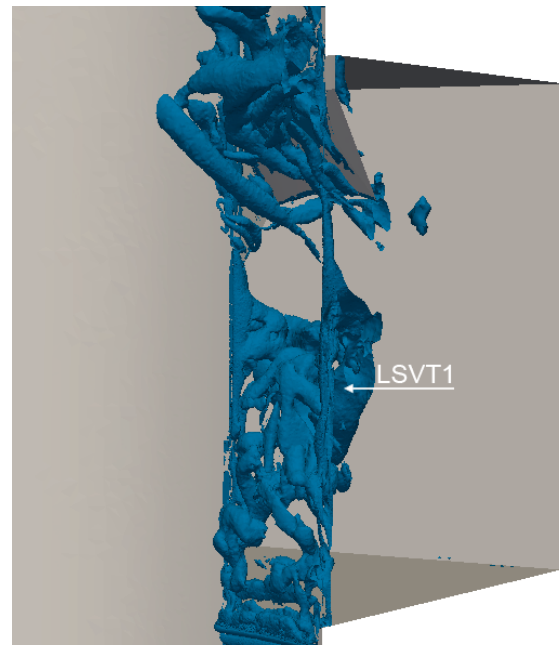
(d) t=0.03s
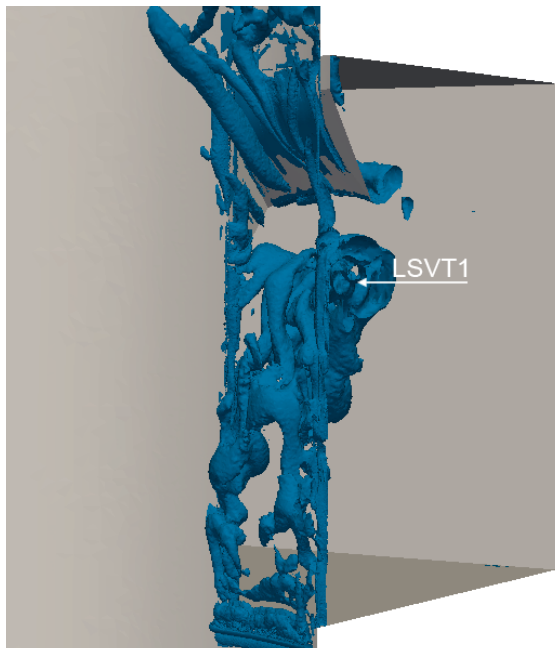
(e) t=0.04s

(f) t=0.05s
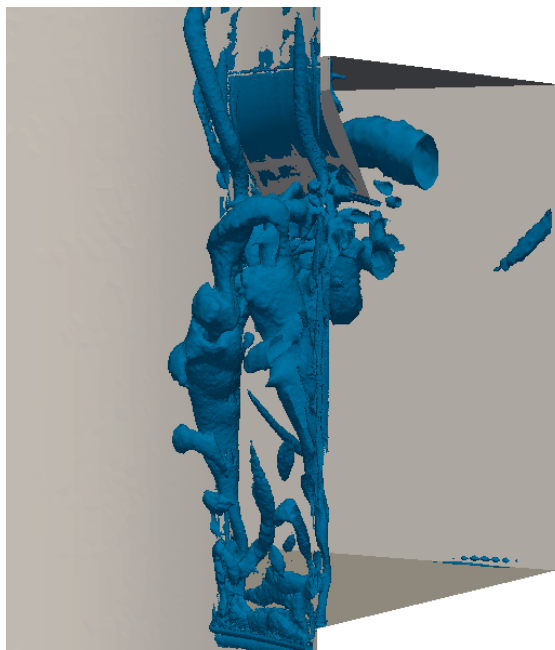
(g) t=0.06s
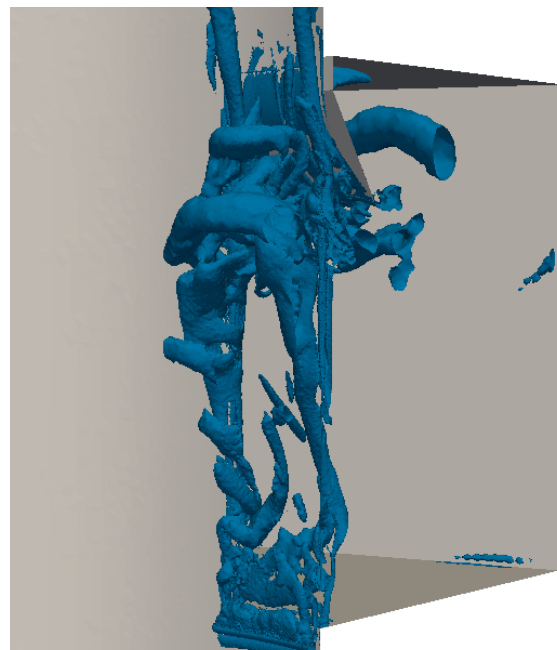
(h) t=0.07s

Figure 8.8: Vortex visualisation span wise cylinder using λ_2-criterion iso-surfaces at $\lambda_2 = -10000$

8.2 Experimental Results

An experimental investigation of the trailing edge extension has been carried out. In this section, the effect of the trailing edge extension on the full range of tunnel operating conditions will be presented. Furthermore spectra for specific operating points will be discussed. Last but not least, a comparison of the experiment with CFD data will be shown, adding additional insights to the validation carried out in Section 7.3.

8.2.1 Oscillation strength

The cavity buffeting peaks of the sound pressure spectra at velocity settings from 25% to 95%, corresponding to velocities between 19 and 76.6 ms^{-1}, in steps of 5% (3.8 ms^{-1}) have been extracted and presented in Figure 8.9(a) for both the current situation and the case with the extension. The difference between both cases has been calculated and presented in Figure 8.9(b). A positive ΔSPL represents a reduction in sound pressure. The same data has been tabulated in Table 8.3.

It is shown that for velocities of 19 and 22.8 ms^{-1}, an increase in sound pressure has been established by utilising the extension. Despite an increase in sound pressure, the absolute values of the sound pressure level are relatively low for the indicated velocities, yielding no immediate problem induced by the increase.

Furthermore for all other velocity settings, a reduction ranging from 7.7 dB to a maximum of 20.6 dB has been found. Especially in the range of 55 % to 75%, in which the cavity buffeting has been experience to be strong, the maximum sound pressure levels have been reduced below 130.1 dB. Subjective testing yields a large increase in comfort for the complete range of tunnel velocities.

Table 8.3: Peak sound pressure levels, for current situation and trailing edge extension at various tunnel velocities

Fan Setting	25%	30%	35%	40%	45%	50%	55%
Velocity [ms^{-1}]	19	22.8	26.6	30.4	34.2	38.0	41.8
Current Situation [dB]	89.2	98.4	104.8	119.1	118.3	129.2	135.9
Extension [dB]	107.7	99.3	95.0	98.7	108.1	112.0	125.7
Difference [dB]	-18.5	-0.9	9.9	20.4	10.2	17.2	10.2

Fan Setting	60%	65%	70%	75%	80%	85%	90%	95%
Velocity [ms^{-1}]	45.6	49.4	53.2	57.0	60.8	64.6	68.4	72.2
Current Situation [dB]	138.2	137.3	136.7	137.1	121.9	124.1	131.4	131.3
Extension [dB]	130.1	119.5	121.5	128.2	114.1	109.6	117.6	110.7
Difference [dB]	8.1	17.9	15.2	8.8	7.7	14.5	13.7	20.6
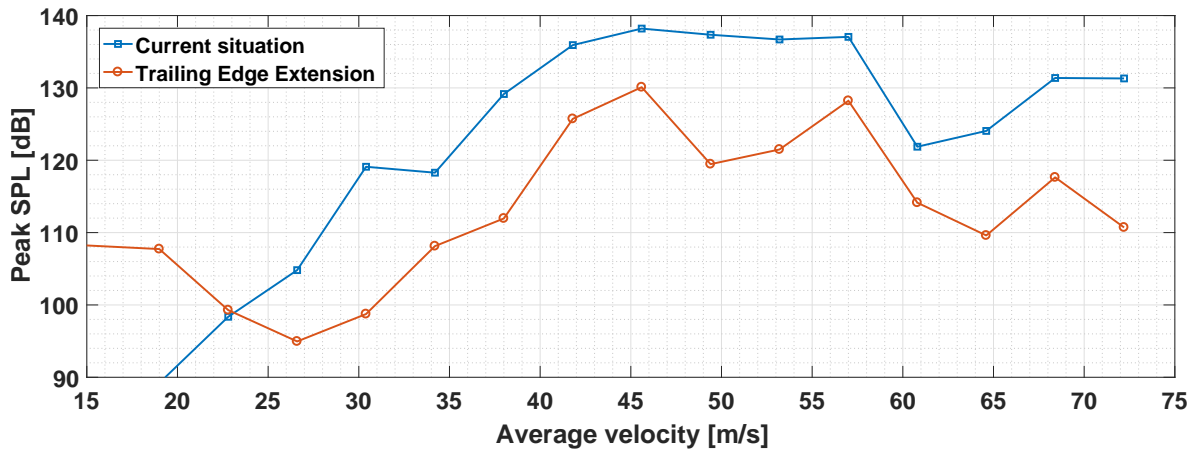
(a) Comparison peak sound pressure levels at different tunnel velocities
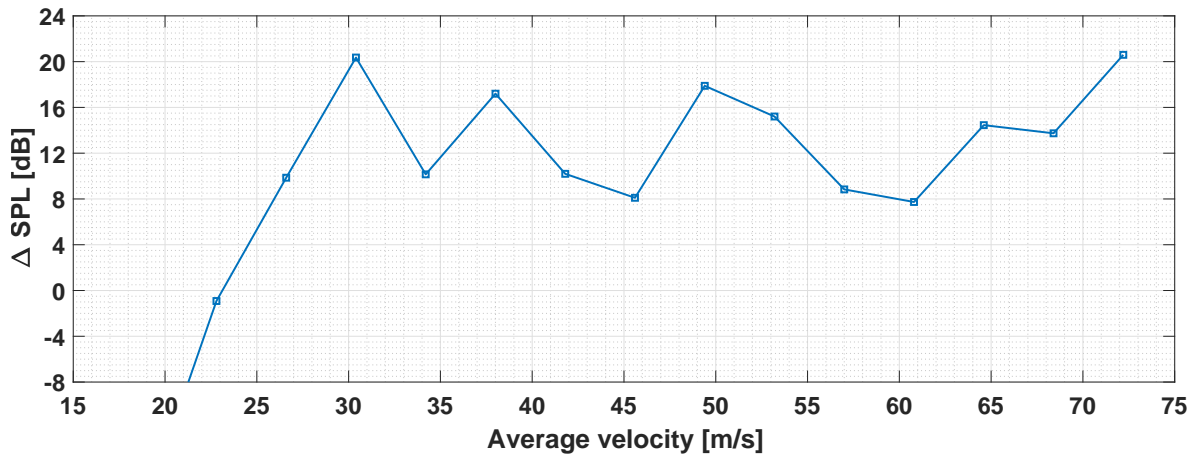
(b) Difference in peak sound pressure level at different tunnel velocities

Figure 8.9: Peak sound pressure level comparison current situation and trailing edge extension

8.2.2 Spectral results

Following the evident sound pressure reductions found in Section 8.2.1, the spectrum for the operating velocity of 68.4 ms^{-1}, which approximately corresponds to the simulated velocity in CFD (70 ms^{-1}), has been presented in Figure 8.10. A very large difference in the peak of the spectrum when the current situation is compared with the case using the extension is observed immediately. Where a clear distinct peak is observed in the current situation at 16.6 Hz, the sound pressure level is largely reduced at this frequency. The second Rossiter mode (based on an estimation shown in Figure 8.10) has been introduced mildly. However, this mode remains of less interest, as the corresponding sound pressure levels are much lower.
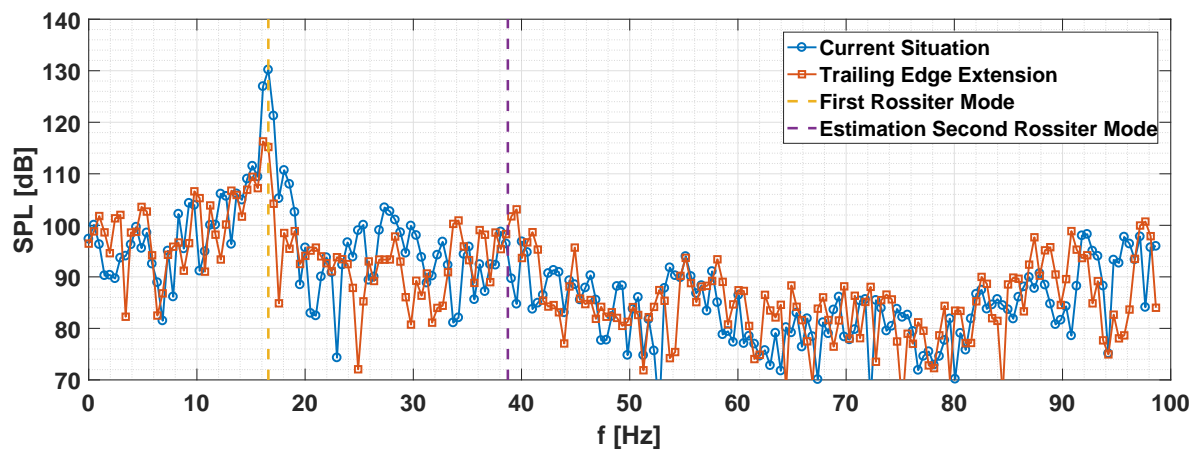
Figure 8.10: Experiment sound pressure level spectrum at 68.4 ms^{-1}, comparison current situation and trailing edge extension

Furthermore, the results in Section 8.2.1 yield a very strong sound pressure reduction for an operating velocity of 49.4 ms^{-1}. The spectra of both the current situation and the case in which the trailing edge extension has been applied have been presented in Figure 8.11. Again a large reduction for the first Rossiter mode can be observed. An interesting result can be observed around 50 Hz, in which a new peak has been introduced by the trailing edge extension. No evident flow mechanism has been found to cause this particular peak at this frequency. However, this new mode is observed to have a much lower sound pressure level than the first Rossiter mode, which suggests it has very low influence of cavity buffeting noise.
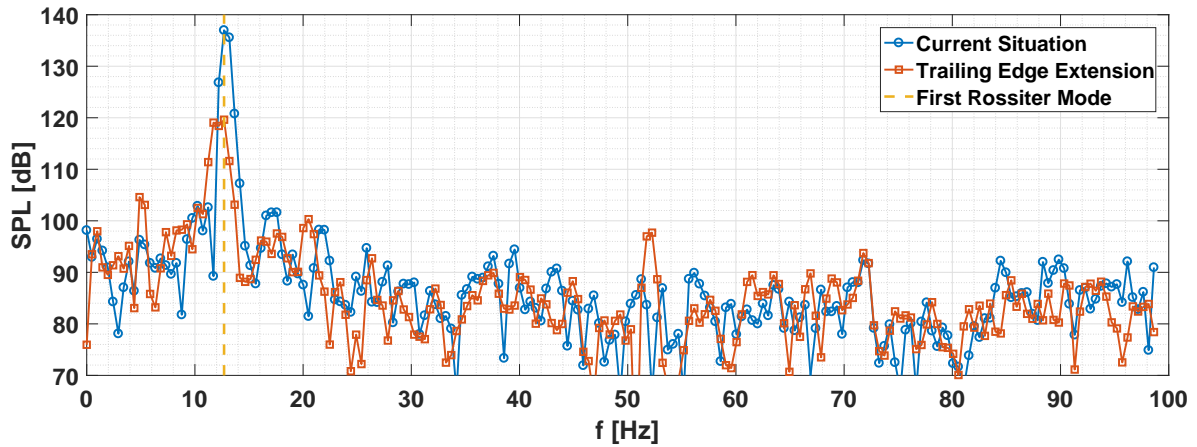
Figure 8.11: Experiment sound pressure level spectrum at 49.4 ms^{-1}, comparison current situation and trailing edge extension

8.3   Validation

Following the comparison between CFD and experiment in Section 7.3, a comparison for the extended trailing edge has been presented in Figure 8.12.

The peak sound pressure level in CFD has been found to be 142.7 dB and the peak sound pressure level in the experiment was found to be 117.6 dB, which resembles a 25.1 dB difference corresponding to an error of 17.6%.

Furthermore a reduction of 13.7 dB has been established in the experiment, which shows a large difference with CFD (Figure 8.1(a)) for which a reduction of only 6.0 dB was found.
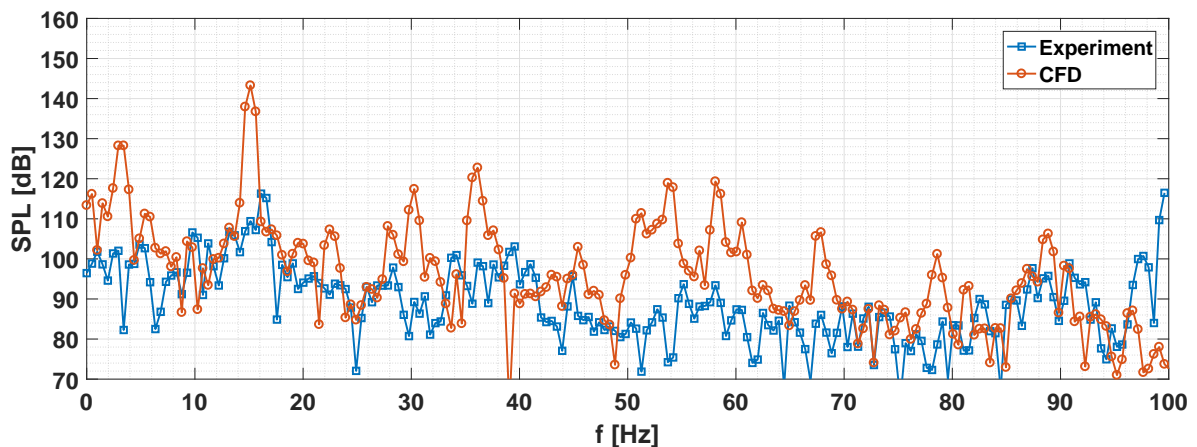
Figure 8.12: Comparison sound pressure level spectra CFD and Experiment using trailing edge extension

Part IV

Conclusions and Recommendations

Chapter 9

Conclusions

Following the results and discussion presented in Part III, the research questions formulated in Section 1.3 will be answered systematically in this chapter.

To which extend can the numerical set-up be validated for sky-dive cavity buffeting noise prediction?

- *Which flow mechanisms have to be anticipated according to existing literature?*

  Existing literature has indicated that a vortex shedding and a feedback mechanism has to be anticipated for a numerical set-up for the prediction of cavity buffeting noise. Furthermore, acoustic volume monopoles and surface dipoles have to be anticipated. Strong discrete frequencies have to be expected. The flow mechanisms restrict to the use of numerical models to those which can account for compressibility of the feedback mechanism.

- *Which numerical set-ups have been validated before for similar problems and are feasible to use within the scope of the thesis project, according to existing literature?*

  A compressible transient solver using Detached Eddy Simulation has shown to be capable of predicting cavity buffeting noise and cavity buffeting noise reductions in existing literature and appeared within the scope of the thesis work.

- *How do the numerical predictions correlate with experimental measurements?*

  Comparison of the current situation at City Sky-Dive Utrecht between numerical prediction and experiment has shown errors of 11.8% in Sound Pressure Level and 10.7% in frequency. Evaluation measurements after applying the trailing edge extension has shown an error of 17.6% in sound pressure level. In experiment a reduction of the oscillation strength of 13.8 dB has been found compared to 6 dB reduction in CFD.

Summarising, consistent with existing literature on the issue of cavity buffeting noise, the correct flow mechanisms have been found in numerical simulation. However the strength of the

mechanisms is predicted wrong. Furthermore a reduction have been found in both the numerical simulation and experiment. However the reduction is under estimated by the numerical simulation compared to reality. Concluding the validity of the numerical model limits to the prediction of a reduction, of which the effect is underestimated for this specific test case.

Which retrofit design is most effective in suppressing cavity buffeting noise, according to the numerical set-up?

- *Which retrofit designs can be proposed based on existing literature and the expected flow mechanisms?*

  Four retrofit designs have been proposed. A wall-normal cylinder, a span-wise cylinder and wing at the leading edge of the cavity to either break-up the strong large-scale span-wise vortices or to lift the shear-layer. Furthermore an retrofit extension of the trailing edge has been proposed in order to prevent the shear layer to slip over the edge.

- *How do the retrofit designs affect cavity buffeting noise and the associated flow mechanisms, according to the numerical set-up?*

  The tailing edge extension and wing have shown a cavity buffeting noise reduction of respectively 6 dB and 2.3 dB. The wall-normal cylinder and span-wise cylinder have shown cavity buffeting noise increases of respectively 1.5 dB and 3.6 dB. Changes in vortex formation/development in the cavity opening have been observed. The span-wise cylinder and wall normal-cylinder influence the shed vortices directly. However, the formation of a larger scale vortex is observed to occur further upstream than for the current situation. Furthermore, for the wing and trailing edge extension, the formation of a larger scale vortex has been shifted downstream compared to the current situation.

- *How do the retrofit designs affect tunnel performance in the sky-dive section, according to the numerical set-up?*

  Downstream of the cavity, a wake is observed, which is affected by the retrofit designs. The trailing edge extension reduces the size of the wake by 5.2%. The span-wise cylinder and wall-normal cylinder increase the size of the wake of respectively 12.4% and 24.7%. The wing shows a wake which is very similar to the current situation: a grow of 2.1% has been observed.

Concluding, the trailing edge extensions show the largest reduction of cavity buffeting noise in simulation. When a reduction is found, the formation of the larger scale vortex is delay downstream. Next to this the tunnel performance is increased as the wake, downstream of the cavity opening is reduced.

To what extend is the cavity buffeting noise suppression effective, according the evaluation measurements?

- *Which oscillation strength reduction is found for the simulate tunnel velocity according to experimental measurements?*

  Evaluation measurements have shown a reduction of 13.8 dB at the velocity used in numerical simulations, which is a larger reduction that found in the simulation.

- *How does the retrofit design influence oscillation strength for other tunnel velocities?*

  The maximum sound pressure levels, for all operating velocities which resulted in high sound pressure levels in the current situation, reductions between 7.7 dB and 22.6 dB have been observed using the trailing edge extension. Over the whole range of operating velocities, the maximum sound pressure level has been reduced to 130.1 dB and below, yielding an improvement of comfort.

Concluding, the application of a trailing edge extension is very effective. Large reductions are found for all critical tunnel velocities, yielding a large improvement in comfort.

Chapter 10

Recommendations

Regarding the current study, the following recommendations for future work on the validation and numerical set-up for the prediction of sky-dive cavity buffeting noise can be proposed.

1. In order reduce the over-estimation of the oscillation strength, porous models (and zones) can be considered in order to model the effect of the perforated plates. Implementation of suitable numerical models can be tedious, as porous zones are not oriented in the flow direction.

2. Furthermore, boundary-layer thickness measurements can be considered for matching of the boundary-layer thickness in simulation. Boundary conditions modelling rough patches can be used in order to match the correct thickness. Closer validation can be expected when correct boundary-layer thickness is observed in the simulation.

3. A newer version of OpenFOAM (V1706) contains a solver for compressible low Mach number flows, which improves on the mitigation of spurious waves. This particular solver might be interesting for improved accuracy.

4. Implementation of adapted fan curve boundary conditions for the inlet of the truncated domain, which could lead to the elimination of the boundary condition induced oscillation and to improve on matching of the physical behaviour of a sky-dive tunnel.

Furthermore, after the advantage of using geometric solutions near the trailing edge of the cavity has been shown by the current study, a parametric study can be executed in order to find the optimal trailing edge shape for a typical sky-dive cavity (recommended to perform this study in 2 dimensions to reduce computational cost). Next to this a multiple tunnel velocities can be simulated in order to validate the velocity dependent trend.

Bibliography

KK Ahuja and Jeff Mendoza. Effects of cavity dimensions, boundary layer, and temperature on cavity noise with emphasis on benchmark data to validate computational aeroacoustic codes. 1995.

Christophe Bailly, Philippe Lafon, and Sebastien Candel. A stochastic approach to compute noise generation and radiation of free turbulent flows. *DGLR BERICHT*, pages 669–669, 1995.

H Bergh and Hendrik Tijdeman. Theoretical and experimental results for the dynamic response of pressure measuring systems. 1965.

Michael Bolduc, Manar Elsayed, and Samir Ziada. Effect of upstream edge geometry on the trapped mode resonance of ducted cavities. In *ASME 2013 Pressure Vessels and Piping Conference*, pages V004T04A028–V004T04A028. American Society of Mechanical Engineers, 2013.

NORMAN Broner. The effects of low frequency noise on peoplea review. *Journal of Sound and Vibration*, 58(4):483–500, 1978.

Tim Colonius and Sanjiva K Lele. Computational aeroacoustics: progress on nonlinear problems of sound generation. *Progress in Aerospace sciences*, 40(6):345–416, 2004.

Sławomir Dykas, Sebastian Rulik, and Włodzimierz Wróblewski. Numerical modelling of aerodynamic noise in compressible flows. *Open Journal of Fluid Dynamics*, 2(03):65, 2012.

Bence Farkas and György Paál. Numerical study on the flow over a simplified vehicle door gap-an old benchmark problem is revisited. *Periodica Polytechnica. Civil Engineering*, 59(3):337, 2015.

E Garnier, N Adams, and P Sagaut. Les governing equations. *Large Eddy Simulation for Compressible Flows*, pages 5–39, 2009.

M Gharib and A Roshko. The effect of flow oscillations on cavity drag. *Journal of Fluid Mechanics*, 177:501–530, 1987.

Xavier Gloerfelt. Cavity noise. *VKI lecture series*, 3, 2009.

Xu Gong, Jun Wang, Chaoyi Deng, Penghui Wei, Bo Liu, and Lin Li. Optimization and simulation of suv sunroof buffeting noise. In *Society of Automotive Engineers (SAE)-China Congress*, pages 365–373. Springer, 2016.

Christopher J Greenshields. Openfoam user guide. *OpenFOAM Foundation Ltd, version*, 3(1), 2015.

Björn Greschner, Julien Grilliat, Marc C Jacob, and F Thiele. Measurements and wall modeled les simulation of trailing edge noise caused by a turbulent boundary layer. *International Journal of Aeroacoustics*, 9(3):329–355, 2010.

Bernhard F.W. Gschaider. swak4foam. http://hg.code.sf.net/p/openfoam-extend/swak4Foam, 2017.

KE Haneke, BL Carson, CA Gregorio, and EA Maull. Infrasound: brief review of toxicological literature. *Research Triangle Park, NC: National Institute of Environmental Health Sciences*, 2001.

H Heller and D Bliss. The physical mechanism of flow-induced pressure fluctuations in cavities and concepts for their suppression. In *2nd Aeroacoustics Conference*, page 491, 1975.

Brenda Henderson. Automobile noise involving feedback- sound generation by low speed cavity flows. In *Third Computational Aeroacoustics(CAA) Workshop on Benchmark Problems*, volume 1, 2000.

MS Howe. Mechanism of sound generation by low mach number flow over a wall cavity. *Journal of sound and vibration*, 273(1):103–123, 2004.

S.J. Hulshoff. *CFD II Part2: Computation and Modelling of Turbulence*. Faculty of Aerospace Engineering, TU Delft, 2015.

M Inagaki, O Murata, T Kondoh, and K Abe. Numerical prediction of fluid-resonant oscillation at low mach number. *AIAA journal*, 40(9):1823–1829, 2002.

H Jasak. *Error Analysis and Estimation for the Finite Volume Method with Applications to Fluid Flows, 1996*. PhD thesis, Ph. D. Thesis, University of London Imperial College, 1996.

Jinhee Jeong and Fazle Hussain. On the identification of a vortex. *Journal of fluid mechanics*, 285:69–94, 1995.

Ming Jiang, Raghu Machiraju, and David Thompson. Detection and visualization of. *The Visualization Handbook*, 295, 2005.

HS Kook. Visualization of periodic flows over a sunroof opening by using a phase-marked piv measurement. *International Journal of Automotive Technology*, 9(4):493–500, 2008.

Valentina Koschatzky, Jerry Westerweel, and Bendiks Jan Boersma. Comparison of two acoustic analogies applied to experimental piv data for cavity sound emission estimation. In *16th AIAA/CEAS Aeroacoustics Conference*, page 3812, 2010.

RB Langtry and PR Spalart. Des investigation of a baffle device for reducing landing-gear cavity noise. In *46th AIAA Aerospace Sciences Meeting and Exhibit, Reno, NV, Jan*, pages 7–10, 2008.

Robin Langtry and Philippe Spalart. Detached eddy simulation of a nose landing-gear cavity. In *IUTAM Symposium on Unsteady Separated Flows and Their Control*, pages 357–366. Springer, 2009.

Morton K Ohlbaum. Mechanical resonant frequency of the human eye'in vivo'. Technical report, DTIC Document, 1976.

Ahmed Omer and Atef Mohany. Suppression of acoustic resonance in rectangular cavities using spanwise control cylinder. In *ASME 2015 Pressure Vessels and Piping Conference*, pages V004T04A042–V004T04A042. American Society of Mechanical Engineers, 2015.

Ahmed Omer, Atef Mohany, and Marwan Hassan. Effect of flow impingement on the acoustic resonance excitation in a shallow rectangular cavity. *Advances in Structural Engineering and Mechanics*, 2015.

R Pemberton. An overview of dynamic pressure measurement considerations. 2010.

Enrico Ribaldone, Mauro Casella, Giuseppe Scantamburlo, and Roberto Tregnago. Computational aeroacoustic of buffeting phenomena coming from an open sunroof. In *ASME 8th Biennial Conference on Engineering Systems Design and Analysis*, pages 833–838. American Society of Mechanical Engineers, 2006.

D Rockwell and C Knisely. Vortex-edge interaction: Mechanisms for generating low frequency components. *The Physics of Fluids*, 23(2):239–240, 1980.

D. Rockwell and E. Naudascher. Review - Self-sustaining oscillations of flow past cavities. *ASME Transactions Journal of Fluids Engineering*, 100:152–165, June 1978.

J.E. Rossiter. *Wind-tunnel Experiments on the Flow Over Rectangular Cavities at Subsonic and Transonic Speeds*. Reports and memoranda. H.M. Stationery Office, 1967.

CW Rowley, T Colonius, and AJ Basu. On self-sustained oscillations in two-dimensional compressible flow over rectangular cavities. *JOURNAL OF FLUID MECHANICS*, 455:315–346, MAR 25 2002. ISSN 0022-1120.

Christopher J Roy. Review of code and solution verification procedures for computational simulation. *Journal of Computational Physics*, 205(1):131–156, 2005.

Scanivalve. Dsa3217/3218 series pressure scanner operation and service manual. (Software Version 1.23), 2009.

John W Slater. Examining spatial (grid) convergence. *Public tutorial on CFD verification and validation, NASA Glenn Research Centre, MS*, 86, 2006.

Philipe R Spalart, Steven R Allmaras, et al. A one equation turbulence model for aerodynamic flows. *RECHERCHE AEROSPATIALE-FRENCH EDITION-*, pages 5–5, 1994.

Philippe R Spalart. Detached-eddy simulation. *Annual review of fluid mechanics*, 41:181–202, 2009.

Philippe R Spalart, Shur Deck, ML Shur, KD Squires, M Kh Strelets, and A Travin. A new version of detached-eddy simulation, resistant to ambiguous grid densities. *Theoretical and computational fluid dynamics*, 20(3):181–195, 2006.

PR Spalart, WH Jou, M Strelets, SR Allmaras, et al. Comments on the feasibility of les for wings, and on a hybrid rans/les approach. *Advances in DNS/LES*, 1:4–8, 1997.

Yiping Wang, Yadong Deng, Zhendong Yang, Tao Jiang, Chuqi Su, and Xue Yang. Numerical study of the flow-induced sunroof buffeting noise of a simplified cavity model based on the slightly compressible model. *Proceedings of the Institution of Mechanical Engineers, Part D: Journal of Automobile Engineering*, 227(8):1187–1199, 2013.

Yiping Wang, Shuai Li, and Xue Yang. Numerical investigation of the passive control of cavity flow oscillations by a dimpled non-smooth surface. *Applied Acoustics*, 111:16–24, 2016.

Frank M White and Isla Corfield. *Viscous fluid flow*, volume 3. McGraw-Hill Higher Education Boston, 2006.

Rodger E Ziemer, William H Tranter, and D Ronald Fanin. *Signals and systems: Continuos and discrete*. Macmillan Publishing Company, 1993.

Appendix A

SA RANS definitions

A.1 Transport equation

$$\frac{\partial \tilde{\nu}}{\partial t} + \frac{\partial}{\partial x_j}(\tilde{\nu} u_j) = C_{b1}[1 - f_{t2}]\tilde{S}\tilde{\nu} + \frac{1}{\sigma}\{\nabla \cdot [(\nu + \tilde{\nu})\nabla \tilde{\nu}] + C_{b2}|\nabla \tilde{\nu}|^2\} - \left[C_{w1}f_w - \frac{C_{b1}}{\kappa^2}f_{t2}\right]\left(\frac{\tilde{\nu}}{d}\right)^2 + f_{t1}\Delta U^2 \tag{A.1}$$

A.2 Definitions

$$\nu_t = \tilde{\nu} f_{v1}, \quad f_{v1} = \frac{\chi^3}{\chi^3 + C_{v1}^3}, \quad \chi := \frac{\tilde{\nu}}{\nu} \tag{A.2}$$

$$\tilde{S} \equiv S + \frac{\tilde{\nu}}{\kappa^2 d^2}f_{v2}, \quad f_{v2} = 1 - \frac{\chi}{1 + \chi f_{v1}} \tag{A.3}$$

$$S = \sqrt{2\Omega_{ij}\Omega_{ij}} \tag{A.4}$$

$$\Omega_{ij} \equiv \frac{1}{2}(\frac{\partial u_i}{\partial x_j} - \frac{\partial u_j}{\partial x_i}) \tag{A.5}$$

$$f_w = g \left[\frac{1 + C_{w3}^6}{g^6 + C_{w3}^6} \right]^{1/6}, \quad g = r + C_{w2}(r^6 - r), \quad r \equiv \frac{\tilde{\nu}}{\tilde{S}\kappa^2 d^2} \tag{A.6}$$

$$f_{t1} = C_{t1}g_t \exp\left(-C_{t2}\frac{\omega_t^2}{\Delta U^2}[d^2 + g_t^2 d_t^2]\right) \tag{A.7}$$

$$f_{t2} = C_{t3}\exp(-C_{t4}\chi^2) \tag{A.8}$$

A.3   Constants

$$
\begin{aligned}
\sigma &= && 2/3 \\
C_{b1} &= && 0.1355 \\
C_{b2} &= && 0.622 \\
\kappa &= && 0.41 \\
C_{w1} &= && C_{b1}/\kappa^2 + (1 + C_{b2})/\sigma \\
C_{w2} &= && 0.3 \\
C_{w3} &= && 2 \\
C_{v1} &= && 7.1 \\
C_{t1} &= && 1 \\
C_{t2} &= && 2 \\
C_{t3} &= && 1.1 \\
C_{t4} &= && 2
\end{aligned}
\tag{A.9}
$$

Discretisation

B.1   Discretised Gaussian Integration

An essential part of the discretisation in OpenFOAM is the use of the divergence theorem. Jasak (1996) describes how this theorem is discretised in OpenFOAM, of which the result is presented in Equation (B.1).

$$\int_{V_p} \nabla \cdot \boldsymbol{a} \, dV = \oint_{\delta V_p} d\boldsymbol{S} \cdot \boldsymbol{a} = \sum_f \boldsymbol{S} \cdot \boldsymbol{a_f} \tag{B.1}$$
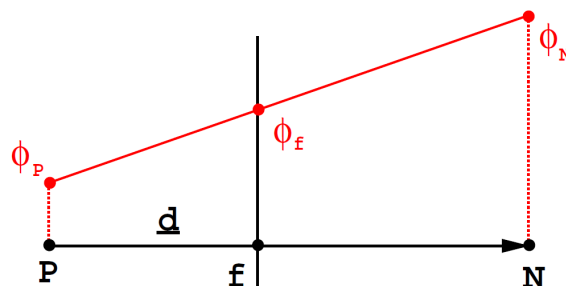
B.2   Numerical schemes

Figure B.1: 1D control volume (Jasak, 1996)

B.2.1 Upwind

The upwind interpolation scheme is only first order accurate. It however it ensures stability. Following the one dimesional control volume, presented in Figure B.1, in which flow is assumed from P to N, the interpolation is preformed as presented in Equation (B.2).

$$\phi(\boldsymbol{x_f}) = \phi(\boldsymbol{x_p}) \tag{B.2}$$

B.2.2 Linear Upwind

Suppose a one dimensional control volume, as presented in Figure B.1 exists, on which a variable ϕ exists. Assuming flow is from left to right (from volume P to N) the variable ϕ on the face (separating P and N) may only depend on ϕ_p.

Suppose variable ϕ varies over the volume of volume P, the following taylor series expansion can be formulated.

$$\phi(\boldsymbol{x_f}) = \phi(\boldsymbol{x_P}) + (\boldsymbol{x_f} - \boldsymbol{x_P}) \cdot (\nabla\phi)_P + \frac{1}{2}(\boldsymbol{x_f} - \boldsymbol{x_P})^2 : (\nabla\nabla\phi)_P + O((\boldsymbol{x_f} - \boldsymbol{x_P})^3) \tag{B.3}$$

Truncating the Taylor expansion further to obtain second order accuracy, the scheme presented in Equation (B.4) is obtained.

$$\phi(\boldsymbol{x_f}) = \phi(\boldsymbol{x_P}) + (\boldsymbol{x_f} - \boldsymbol{x_P}) \cdot (\nabla\phi)_P \tag{B.4}$$

B.2.3 Central Differencing

Central differencing is the easiest method for implementing second order accurate interpolation. Using the cell definition in Figure B.1, the values in the cells are interpolated to the faces based on Equation (B.5)

$$\phi_f = f_x \phi_P + (1 - f_x)\phi_N \tag{B.5}$$

With $f_x = \frac{\bar{fN}}{\bar{PN}}$.

B.2.4 Momentum Equation

For the discretisation of the equations, it is convenient to formulate them in vector form. When exploring the code of OpenFOAM, the momentum equation presented in Equation (B.6) can be found. All terms on the left hand side are handled implicit, all the terms on the right hand side are handled explicit.

$$\frac{\partial \bar{\rho}\tilde{\boldsymbol{u}}}{\partial t} + \nabla \cdot (\bar{\rho}\tilde{\boldsymbol{u}}\tilde{\boldsymbol{u}}) - \nabla \cdot (\mu_{eff}\nabla\tilde{\boldsymbol{u}}) = -\nabla p - \nabla \cdot \left(\mu_{eff} \left[\nabla\tilde{\boldsymbol{u}}^T - \frac{2}{3}tr(\nabla\tilde{\boldsymbol{u}}^T) \right] \right) \qquad (B.6)$$

For the application of the finite volume method, the momentum equation is integrated over control volume V_P and over a time-step Δt, as presented in Equation (B.7)

$$\int_t^{t+\Delta t} \left[\frac{\partial}{\partial t} \int_{V_p} \bar{\rho}\tilde{\boldsymbol{u}}dV + \int_{V_p} \nabla \cdot (\bar{\rho}\tilde{\boldsymbol{u}}\tilde{\boldsymbol{u}})\, dV - \int_{V_p} \nabla \cdot (\mu_{eff}\nabla\tilde{\boldsymbol{u}})\, dV \right] dt =$$
$$\int_t^{t+\Delta t} \left[-\int_{V_p} \nabla p dV - \int_{V_p} \nabla \cdot \left(\mu_{eff} \left[\nabla\tilde{\boldsymbol{u}}^T - \frac{2}{3}tr(\nabla\tilde{\boldsymbol{u}}^T) \right] \right) dV \right] dt \qquad (B.7)$$

B.2.5 Temporal term

The first term of the equation is the time derivative. Using backward differencing with Gaussian integration, this term is discretised as shown in Equation (B.8).

$$\frac{\partial}{\partial t} \int_{V_P} \bar{\rho}\tilde{\boldsymbol{u}}dV = \frac{\frac{3}{2}(\bar{\rho}\tilde{\boldsymbol{u}})^n - 2(\bar{\rho}\tilde{\boldsymbol{u}})^{n-1} + \frac{1}{2}(\bar{\rho}\tilde{\boldsymbol{u}})^{n-2}}{\Delta t}V_P \qquad (B.8)$$

B.2.6 Convective term

In order to discretise the convective term, a non-linearity has to be dealt with. In OpenFOAM, linearisation of this term is achieved by using part of this term explicitly form the previous iteration, which implies the following for the convective term. An iterative process is used until $F \approx \tilde{\boldsymbol{u}}$.

Using the identities, presented in Appendix B.1, the following is derived.

$$
\begin{aligned}
\int_{V_p} \nabla \cdot (\bar{\rho}\tilde{\boldsymbol{u}}\tilde{\boldsymbol{u}})\, dV &= \sum_f \boldsymbol{S} \cdot (\bar{\rho}\tilde{\boldsymbol{u}}\tilde{\boldsymbol{u}})_f \\
&= \sum_f \boldsymbol{S} \cdot (\bar{\rho}\tilde{\boldsymbol{u}})_f\, \tilde{\boldsymbol{u}}_f \\
&= \sum_f F\tilde{\boldsymbol{u}}_f
\end{aligned}
\tag{B.9}
$$

Equation (B.9) suggests that an interpolation scheme is needed to relate the velocity in the cells to the velocity on the faces of the cells. Furthermore, face fluxes (F) from previous iterations are stored, for explicit use in the new iteration.

In order to avoid un-physical oscillations (Jasak, 1996), a second order upwind scheme will be used (*linearUpwind*) for the interpolation from cell to face values.

B.2.7 Diffusion Term

Similar to the convective term, the diffusion term contains a divergence operator. Again the following derivation can be obtained by applying the identities in Appendix B.1.

$$
\begin{aligned}
\int_{V_p} \nabla \cdot (\mu_{eff}\nabla\tilde{\boldsymbol{u}})\, dV &= \sum_f \boldsymbol{S} \cdot (\mu_{eff}\nabla\tilde{\boldsymbol{u}})_f \\
&= \sum_f (\mu_{eff})_f\, \boldsymbol{S} \cdot (\nabla\tilde{\boldsymbol{u}})_f
\end{aligned}
\tag{B.10}
$$

The derivation in Equation (B.10) shows the need for a scheme to determine the velocity gradient in the cell-faces. In order to minimize the error made in the diffusion term, it is convenient to split $\boldsymbol{S} \cdot (\nabla\tilde{\boldsymbol{u}})_f$ in a orthogonal part and a non-orthogonal correction as shown in Equation (B.11).

$$
\boldsymbol{S} \cdot (\nabla\tilde{\boldsymbol{u}})_f = \underbrace{\left(\boldsymbol{\Delta} \cdot (\nabla\tilde{\boldsymbol{u}})_f\right)}_{orthogonal} + \underbrace{\left(\boldsymbol{k} \cdot (\nabla\tilde{\boldsymbol{u}})_f\right)}_{non-orthogonal correction}
\tag{B.11}
$$

Evidently, $\boldsymbol{S} = \boldsymbol{\Delta} + \boldsymbol{k}$ has to hold.

Suppose two one dimensional control volumes (P and N) are neighbours, as presented in Figure B.2. Now as $\boldsymbol{\Delta}$ is chosen to be parallel to $\boldsymbol{d}$, the following holds when central differencing is

used.

$$\left(\boldsymbol{\Delta} \cdot (\nabla \tilde{\boldsymbol{u}})_f\right)_{orthogonal} = |\boldsymbol{\Delta}| \frac{\tilde{\boldsymbol{u}}_N - \tilde{\boldsymbol{u}}_P}{|\boldsymbol{d}|} \tag{B.12}$$

Furthermore, the non-orthogonal correct is handled implicitly, by calculating the cell based velocity gradient, after which central differencing (linear scheme in OpenFAOM, see Appendix B.2) is used to interpolate towards the cell faces.
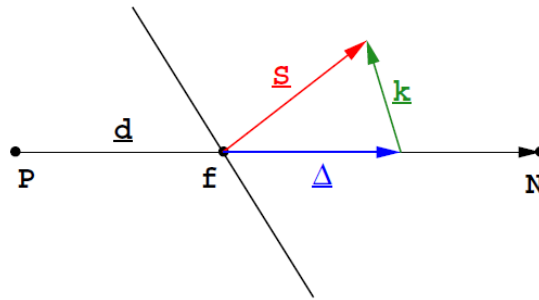

Figure B.2: One dimensional cells (Jasak, 1996)

B.2.8   Pressure gradient term

The pressure gradient term is handled explicitly. Using the identity related to gradients in Appendix B.1, the approximation in Equation (B.13) is derived.

$$\int_{V_p} \nabla \bar{p} dV \approx \sum_f S_f p_f \tag{B.13}$$

Clearly a need for interpolation of pressure towards the cell faces is needed. This is achieved by using central differencing (linear scheme in OpenFOAM, see Appendix B.2).

B.2.9   Stress tensor term

The extra stress tensor term on the right hand side of the momentum equation, is handled explicitly. This term is discrtised as shown in Equation (B.14)

$$\int_{V_p} \nabla \cdot \left(\mu_{eff} \left[\nabla \tilde{\boldsymbol{u}}^T - \frac{2}{3} tr(\nabla \tilde{\boldsymbol{u}}^T)\right]\right) dV \approx \sum_f \boldsymbol{S} \cdot \left(\mu_{eff} \left[\nabla \tilde{\boldsymbol{u}}^T - \frac{2}{3} tr(\nabla \tilde{\boldsymbol{u}}^T)\right]\right)_f \tag{B.14}$$

In order to achieve this, the velocity gradient has to be interpolated from the cell centers to the faces, which is achieved by central differencing (linear scheme in OpenFOAM, see Appendix B.2)

B.2.10 Final Discretised Equation

$$
\frac{\frac{3}{2}(\bar{\rho}\tilde{u})^n - 2(\bar{\rho}\tilde{u})^{n-1} + \frac{1}{2}(\bar{\rho}\tilde{u})^{n-2}}{\Delta t} V_P + \sum_f F\tilde{u}_f^n - \sum_f (\mu_{eff})_f \, \boldsymbol{S} \cdot (\nabla \tilde{u})_f^n =
$$
$$
- \sum_f S_f p_f^{n-1} + \sum_f \boldsymbol{S} \cdot \left(\mu_{eff} \left[\nabla \tilde{u}^T - \frac{2}{3} tr(\nabla \tilde{u}^T) \right] \right)_f^{n-1}
\tag{B.15}
$$

B.2.11 Continuity Equation

The continuity equations resembles the base for the pressure correction. Rewriting the ideal gas law of Equation (4.6) and combining it with Equation (4.1), the following becomes apparent for the pressure equation (Equation (B.16)). In which ψ resembles the compressibility defined by Equation (4.6), and is equal to $(RT)^{-1}$.

$$
\frac{\partial \psi \bar{p}}{\partial t} + \nabla \cdot \bar{\rho}\tilde{u} = 0
\tag{B.16}
$$

Equation (B.16) is integrated over time and control volume P, as shown in Equation (B.17).

$$
\int_t^{t+\Delta t} \left[\frac{\partial}{\partial t} \int_{Vp} \psi \bar{p} dV + \int_{Vp} \nabla \cdot (\bar{\rho}\tilde{u}) \, dV \right] dt = 0
\tag{B.17}
$$

B.2.12 Temporal Term

$$
\frac{\partial}{\partial t} \int_{Vp} \psi \bar{p} dV \approx \frac{\frac{3}{2}(\Psi \bar{p})^n - 2(\Psi \bar{p})^{n-1} + \frac{1}{2}(\Psi \bar{p})^{n-2}}{\Delta t} V_P
\tag{B.18}
$$

B.2.13 Divergence Term

$$
\int_{Vp} \nabla \cdot (\bar{\rho}\tilde{u}) \, dV = \sum_f \boldsymbol{S} \cdot (\bar{\rho}\tilde{u})_f \approx \sum_f \bar{\rho}_f \boldsymbol{S} \cdot (\tilde{u})_f
\tag{B.19}
$$

Furthermore, a semi discretised form of the momentum equation has to be formulated in order to derive a pressure equation. According to Jasak (1996) this equation can be formulated as in Equation (B.20).

$$\tilde{\boldsymbol{u}}_{\boldsymbol{p}} = \frac{1}{a_p} \boldsymbol{H}(\tilde{\boldsymbol{u}}) - \frac{1}{a_p} \nabla \bar{p} \qquad \text{(B.20)}$$

For which a_p and $\boldsymbol{H}(\tilde{\boldsymbol{u}})$ are inherited from the discretisation of the momentum equation (for further details one can refer to Jasak (1996)). Interpolation of $\tilde{\boldsymbol{u}}_{\boldsymbol{p}}$ to the cell faces will produce the following.

$$\tilde{\boldsymbol{u}}_{\boldsymbol{f}} = \left(\frac{1}{a_p} \boldsymbol{H}(\tilde{\boldsymbol{u}})\right)_f - \left(\frac{1}{a_p}\right)_f (\nabla \bar{p})_f \qquad \text{(B.21)}$$

Combining Equation (B.21) and Equation (B.19), produces

$$\sum_f \bar{\rho}_f \boldsymbol{S} \cdot (\tilde{\boldsymbol{u}})_f = \sum_f \boldsymbol{S} \cdot \left(\frac{\bar{\rho}}{a_p} \boldsymbol{H}(\tilde{\boldsymbol{u}})\right)_f - \sum_f \left(\frac{\bar{\rho}}{a_p}\right)_f \boldsymbol{S} \cdot (\nabla \bar{p})_f \qquad \text{(B.22)}$$

Of these two terms, the first one is handled explicit and the second is discretised similar to the diffusion term in Appendix B.2.4.

B.2.14 Final Discretised Equation

The discretised pressure equation has been established as the following.

$$\frac{\frac{3}{2}(\Psi\bar{p})^n - 2(\Psi\bar{p})^{n-1} + \frac{1}{2}(\Psi\bar{p})^{n-2}}{\Delta t} V_P - \sum_f \left(\frac{\bar{\rho}}{a_p}\right)_f \boldsymbol{S} \cdot (\nabla \bar{p})_f^n =$$
$$-\sum_f \boldsymbol{S} \cdot \left(\frac{\bar{\rho}}{a_p} \boldsymbol{H}(\tilde{\boldsymbol{u}})\right)_f^{n-1} \qquad \text{(B.23)}$$

B.3 Enthalpy Equation

$$\frac{\partial}{\partial t}\left(\bar{\rho}\tilde{h}\right) + \frac{\partial}{\partial t}\left(\bar{\rho}\tilde{K}\right) + \frac{\partial}{\partial t}(\bar{p}) + \nabla \cdot \left(\bar{\rho}\tilde{\boldsymbol{u}}\tilde{h}\right) + \nabla \cdot \left(\bar{\rho}\tilde{\boldsymbol{u}}\tilde{K}\right) - \nabla \cdot \left(\alpha_{eff}\nabla\tilde{h}\right) = 0 \quad \text{(B.24)}$$

$$\int_{t}^{t+\Delta t} \left[\frac{\partial}{\partial t} \int_{V_P} \left(\bar{\rho}\tilde{h} \right) dV + \frac{\partial}{\partial t} \int_{V_P} \left(\bar{\rho}\tilde{K} \right) dV + \frac{\partial}{\partial t} \int_{V_P} \left(\bar{p} \right) dV \right] dt +$$
$$\int_{t}^{t+\Delta t} \left[\int_{V_P} \nabla \cdot \left(\bar{\rho}\tilde{\boldsymbol{u}}\tilde{h} \right) dV + \int_{V_P} \nabla \cdot \left(\bar{\rho}\tilde{\boldsymbol{u}}\tilde{K} \right) dV - \int_{V_P} \nabla \cdot \left(\alpha_{eff}\nabla\tilde{h} \right) dV \right] dt = 0$$

$$\text{(B.25)}$$

B.3.1   Temporal terms

As the enthalpy equation is used to solver for $\tilde{h}$ and is solved after the momentum and pressure equation in the algorithm, only the first temporal term is used to construct the linear system. The second and third term are based on values, calculated from the momentum and pressure equation. For these three terms, the same backward differencing as in Appendix B.2.4.

B.3.2   Convective terms

$$\int_{V_P} \nabla \cdot \left(\bar{\rho}\tilde{\boldsymbol{u}}\tilde{h} \right) dV = \sum_f \boldsymbol{S} \cdot \left(\bar{\rho}\tilde{\boldsymbol{u}}\tilde{h} \right)_f = \sum_f \boldsymbol{S} \cdot (\bar{\rho}\tilde{\boldsymbol{u}})_f \left(\tilde{h} \right)_f \qquad \text{(B.26)}$$

For this term $(\bar{\rho}\tilde{\boldsymbol{u}})_f$ is inherited from the momentum equation. Interpolation of the quantities in this term to the cell faces is needed. In order to achieve stability, the first order upwind scheme is used.

$$\int_{V_P} \nabla \cdot \left(\bar{\rho}\tilde{\boldsymbol{u}}\tilde{K} \right) dV = \sum_f \boldsymbol{S} \cdot \left(\bar{\rho}\tilde{\boldsymbol{u}}\tilde{K} \right)_f = \sum_f \boldsymbol{S} \cdot (\bar{\rho}\tilde{\boldsymbol{u}})_f \left(\tilde{K} \right)_f \qquad \text{(B.27)}$$

For this term, all variables are calculated using the result of the momentum equation, which makes this term explicit for the enthalpy equation.

B.3.3   Diffusion Term

The diffusion term in the enthalpy equation can be discretised as shown in Equation (B.28).

$$\int_{V_P} \nabla \cdot \left(\alpha_{eff}\nabla\tilde{h} \right) dV = \sum_f \boldsymbol{S} \cdot \left(\alpha_{eff}\nabla\tilde{h} \right)_f = \sum_f (\alpha_{eff})_f \, \boldsymbol{S} \cdot \left(\nabla\tilde{h} \right)_f \qquad \text{(B.28)}$$

Further, this term discretised the same as the difussion term in Appendix B.2.4 using central differencing and implicitly handling of the orthogonal part and the application of an explicit correction.

B.3.4 Final Discretised Equation

$$
\frac{\frac{3}{2}\left(\bar{\rho}\tilde{h}\right)^{n} - 2\left(\bar{\rho}\tilde{h}\right)^{n-1} + \frac{1}{2}\left(\bar{\rho}\tilde{h}\right)^{n-2}}{\Delta t}V_P + \frac{\frac{3}{2}\left(\bar{\rho}\tilde{K}\right)^{n} - 2\left(\bar{\rho}\tilde{K}\right)^{n-1} + \frac{1}{2}\left(\bar{\rho}\tilde{K}\right)^{n-2}}{\Delta t}V_P
$$

$$
+\frac{\frac{3}{2}\left(\bar{p}\right)^{n} - 2\left(\bar{p}\right)^{n-1} + \frac{1}{2}\left(\bar{p}\right)^{n-2}}{\Delta t}V_P + \sum_f \boldsymbol{S}\cdot(\bar{\rho}\tilde{\boldsymbol{u}})_f\left(\tilde{h}\right)_f^{n} - \sum_f (\alpha_{eff})_f\,\boldsymbol{S}\cdot\left(\nabla\tilde{h}\right)_f^{n}
$$

$$
+\sum_f \boldsymbol{S}\cdot(\bar{\rho}\tilde{\boldsymbol{u}})_f\left(\tilde{K}\right)_f^{n} = 0
$$

(B.29)

Appendix C

BC induced pressure oscillation

A non-physical has been observed in the simulation results. This oscillation is caused by a result from the combination of the propagation of a periodic wake downstream of the cavity, together with the prescribed pressure boundary conditions. This behaviour has been visualised in Figure C.1.

The wake downstream of the cavity introduces a blockage effect which fades when the periodic wake leaves the domain. Probing the time-averaged velocity near the wall, an average velocity of 50.6 ms^{-1} over a length of 13.4 m from the cavity to outlet of the domain has been observed. Resulting in a frequency of 3.8 Hz, which is rather close to the observed low-frequency component in Section 7.1.
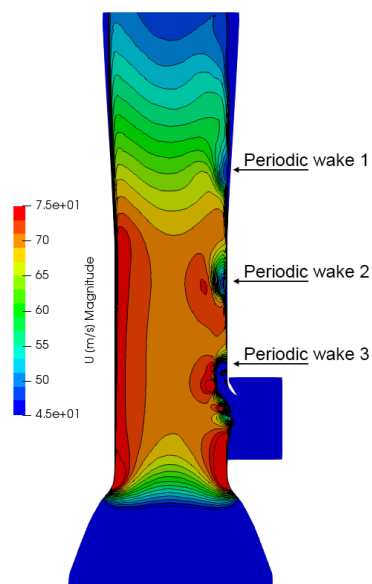
Figure C.1: Instantaneous velocity contours showing periodic wake behaviour.

Appendix D

Geometric deviations
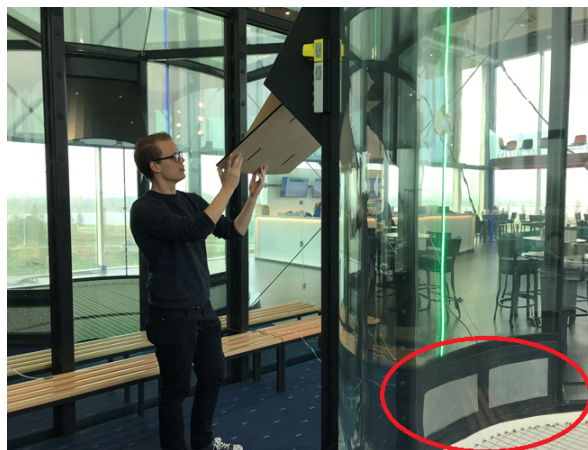
Figure D.1: On-site photo showing installed porous panels and Werner-light

Figure D.2: On-site photo showing big imperfection in building quality

Appendix E

Retrofit designs

E.1 Simulations results

E.1.1 Flow Mechanisms

Wall-normal cylinder

Opposite to the trailing edge extension, the wall normal cylinder increased the oscillation strength. The vortices in the cavity opening are shown in Figure E.1.

Furthermore, the vortex shedding and development of the large scale vortex is very similar as observed before. Two shed-vortices (VT1 and VT2) can be identified in Figure E.1(b), which propagate in Figure E.1(c) and merge in Figure E.1(d) to become a larger scale vortex (LSVT1). In the meanwhile, two new shed vortices (VT3 and VT4) develop. LSVT1, VT3 and VT4 propagate downstream in Figure E.1(e). Finally LSVT1 impinges on the trailing edge in Figure E.1(f).

Compared to the current situation, stretched vortex scales are introduced behind the cylinder, splitting the span-wise vortices. Next to the introduction of length-wise stretched scales, no large differences with the current situation can be identified, which is consistent with the the relative small change in oscillation strength.
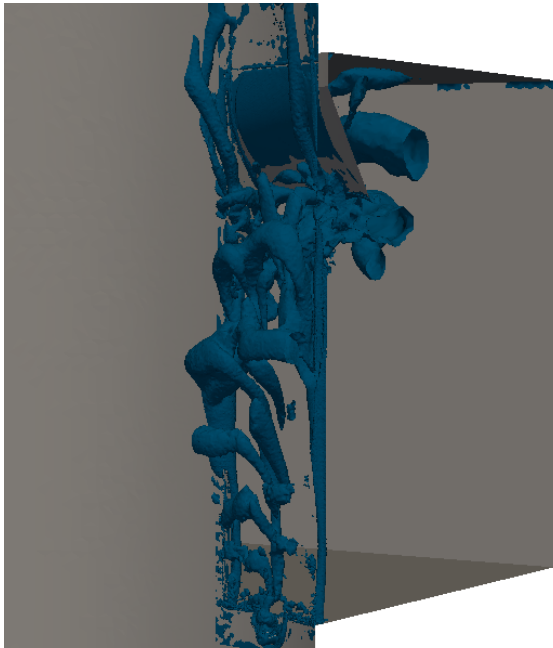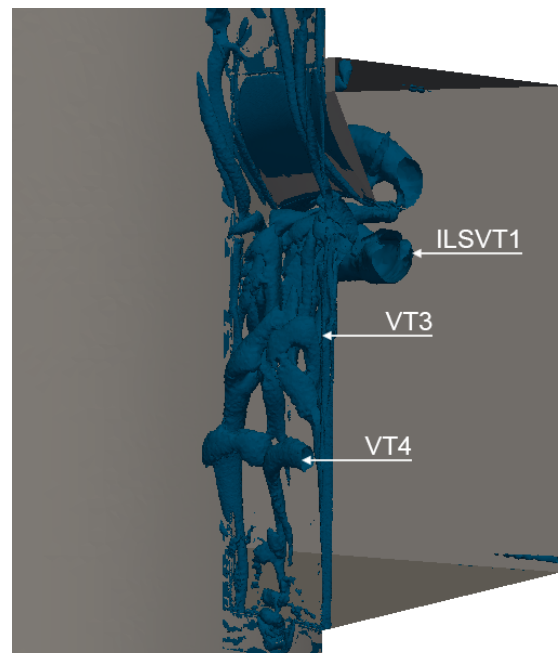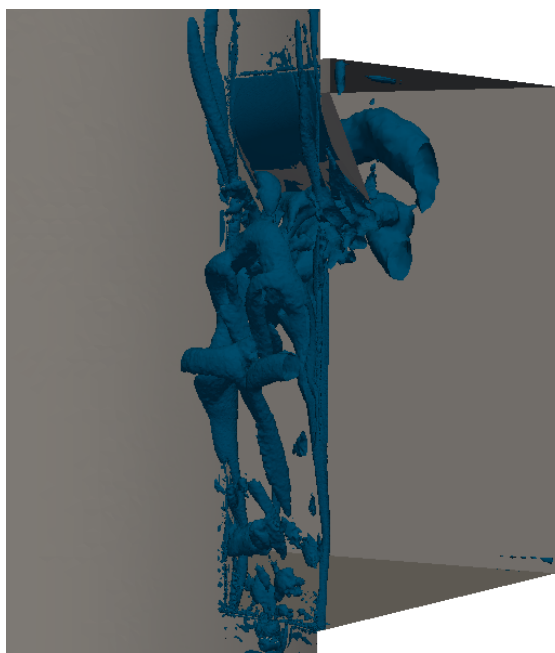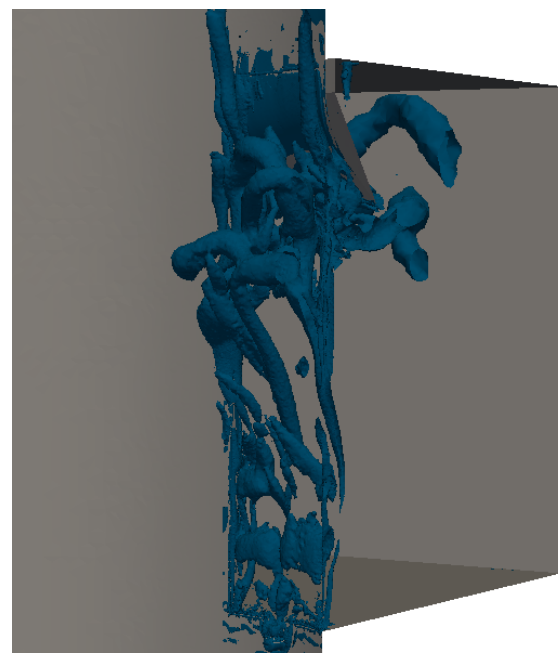
(a) T1
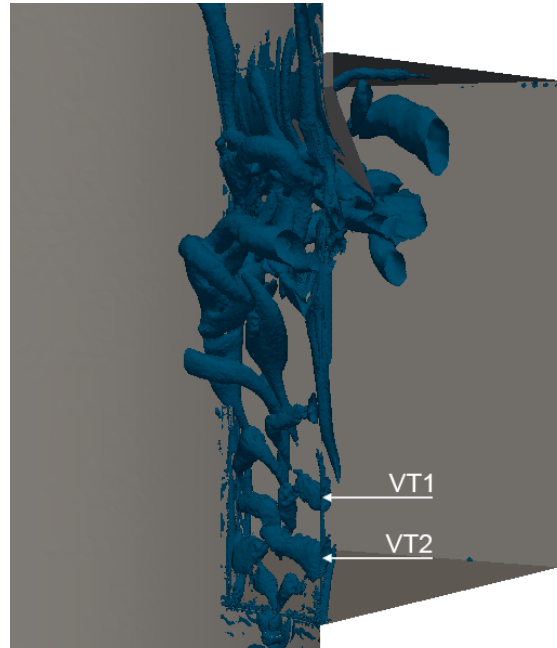
(b) T2
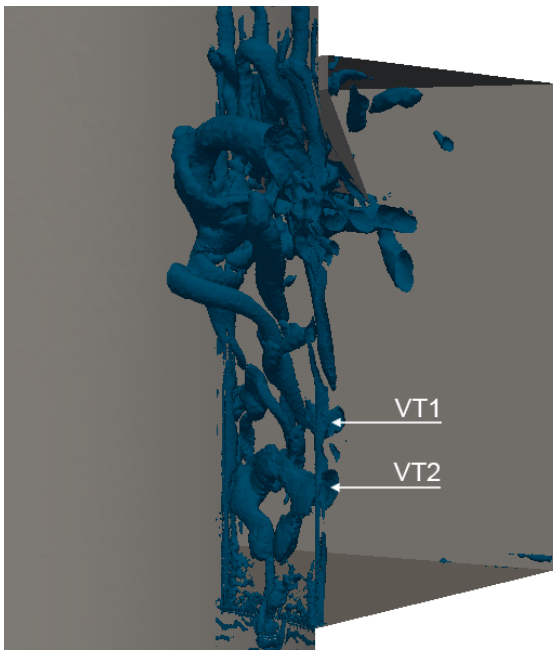
(c) T3
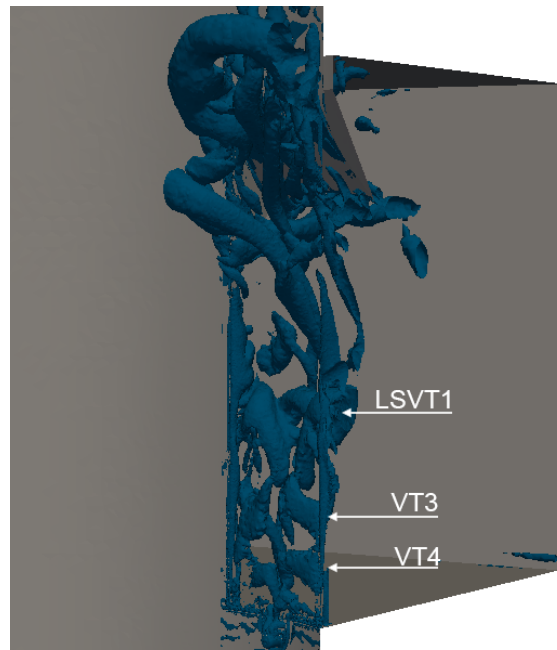
(d) T4
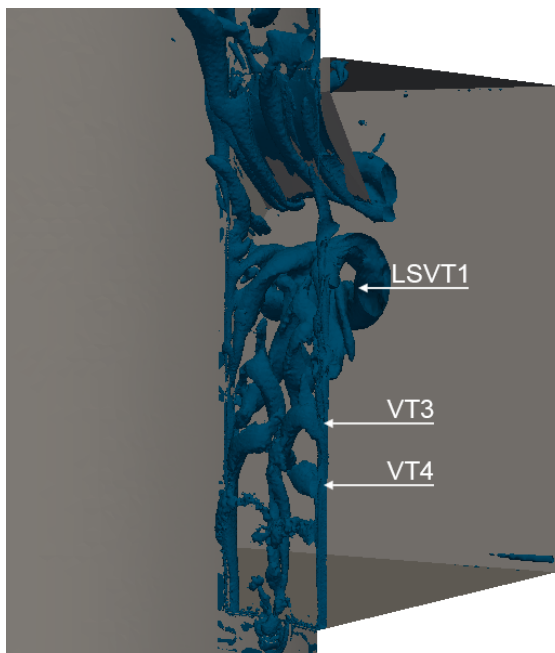
(e) T5

(f) T6

(g) T7

(h) T8

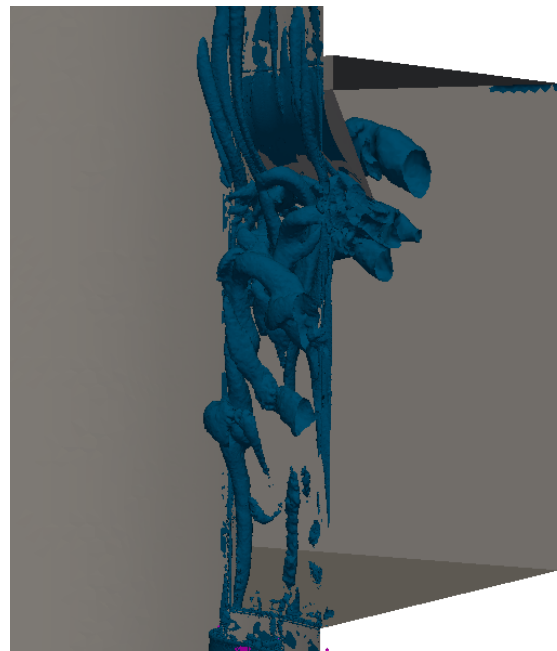**Figure E.1:** Iso-surfaces λ_2-criterion 10000

Wing

The wing slightly reduced the oscillation strength. The associated vortex visualisation has been presented in Figure E.2

Due to the support in the middle of the wing, some length-wise scales are introduced over the cavity opening.
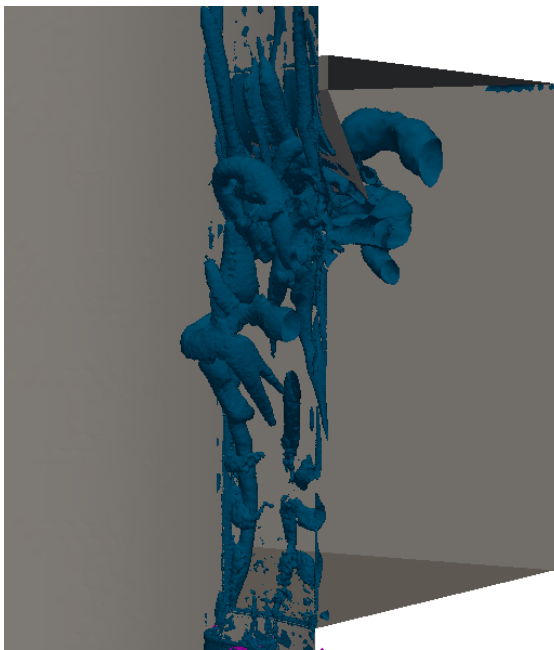
Furthermore, the differences with the current situation are small, which is consistent with the relative small reduction of the oscillation strength.
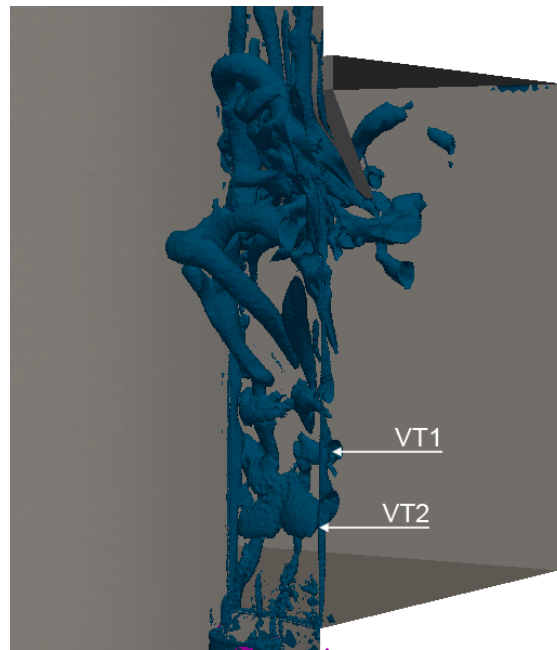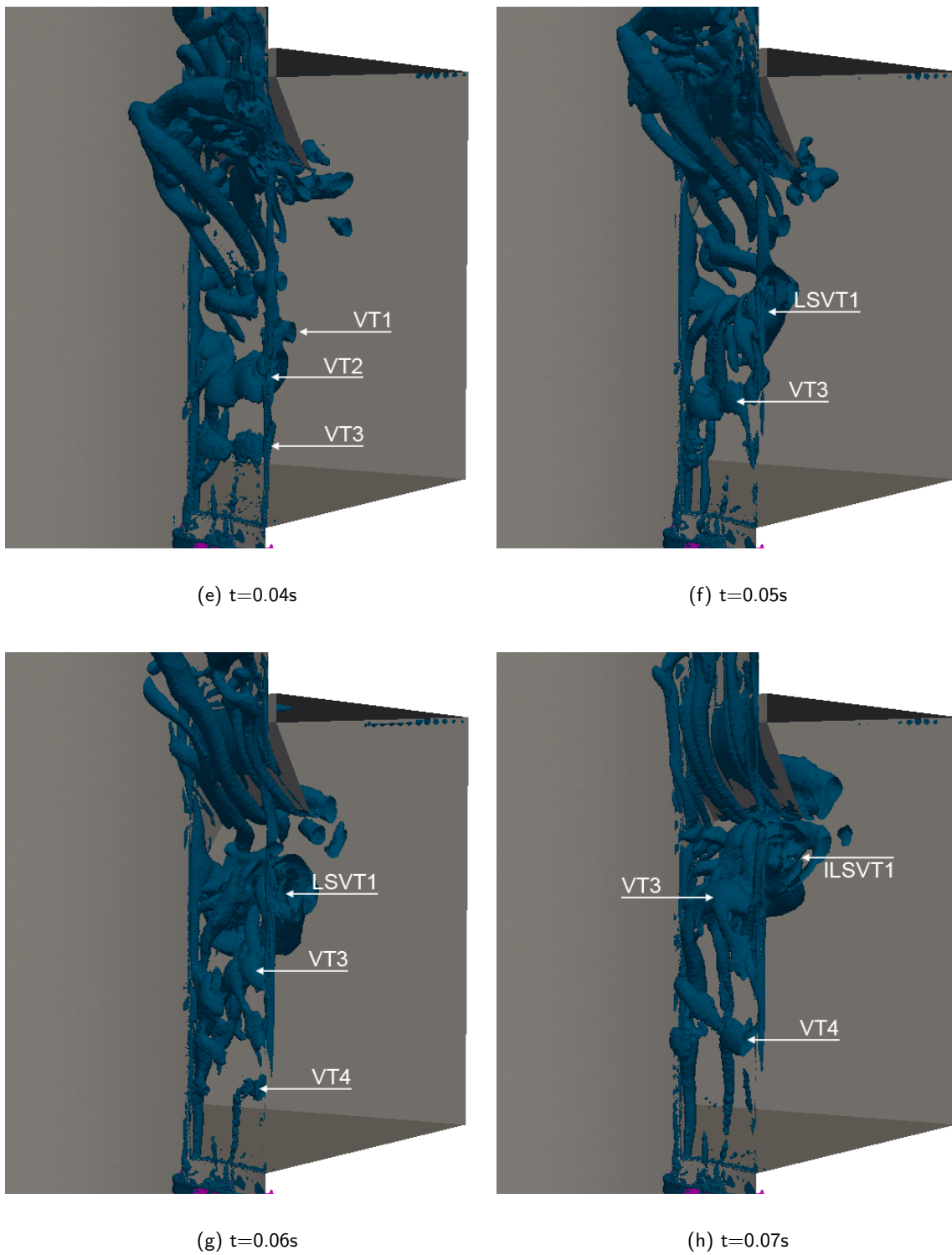
(a) t=0.00s

(b) t=0.01s

(c) t=0.02s

(d) t=0.03s

(e) t=0.04s

(f) t=0.05s

(g) t=0.06s

(h) t=0.07s

Figure E.2: Iso-surfaces λ_2-criterion 10000